



**HAL**  
open science

# Effects of dynamics and optical feedback on hybrid III-V/Si semiconductor lasers

Sandra Cadavid Gomez

► **To cite this version:**

Sandra Cadavid Gomez. Effects of dynamics and optical feedback on hybrid III-V/Si semiconductor lasers. Optics / Photonic. Institut Polytechnique de Paris, 2020. English. NNT : 2020IPPAT008 . tel-03086448

**HAL Id: tel-03086448**

**<https://theses.hal.science/tel-03086448v1>**

Submitted on 22 Dec 2020

**HAL** is a multi-disciplinary open access archive for the deposit and dissemination of scientific research documents, whether they are published or not. The documents may come from teaching and research institutions in France or abroad, or from public or private research centers.

L'archive ouverte pluridisciplinaire **HAL**, est destinée au dépôt et à la diffusion de documents scientifiques de niveau recherche, publiés ou non, émanant des établissements d'enseignement et de recherche français ou étrangers, des laboratoires publics ou privés.

# Effects of Dynamics and Optical Feedback on Hybrid III-V/Silicon Semiconductor Lasers

Thèse de doctorat de l'Institut Polytechnique de Paris  
préparée à Télécom Paris

École doctorale n°626 Polytechnique de Paris (ED IP Paris)  
Spécialité de doctorat: Electronique et optoélectronique

Thèse présentée et soutenue à Palaiseau, 4 March 2020, par

**Sandra C. GOMEZ**

Composition du Jury :

M. Laurent VIVIEN Directeur de Recherches CNRS	Président
M. Vincent RONCIN Maître de Conférences HDR, Université Paris 13	Rapporteur
M. Ammar SHARAIHA Professor, Ecole Nationale d'Ingénieurs de Brest (School of Engineering)	Rapporteur
M. Laurent VIVIEN Directeur de Recherches CNRS	Examineur
M. George FISCHER Senior Scientist, Combat Development and Capability Command (U.S. Army Armaments Center)	Examineur
M. Venkataraman SWAMINATHAN Adjunct Professor, Penn State University (Department of Physics)	Examineur
M. Vassilios KOVANIS Professor & MEng Program Director, Virginia Tech (School of Electrical and Computer Engineering)	Examineur
M. Frederic GRILLOT Professor, Institut Polytechnique - Télécom Paris (School of Communications and Electronics)	Directeur de thèse

**Titre :** Effets de la dynamique et de la rétroaction optique sur les lasers à semi-conducteurs hybrides III-V/Si

**Mots clés :** Circuits intégrés photoniques, lasers à semi-conducteurs, rétroaction optique

**Résumé :** Les circuits intégrés photoniques (PIC) sont devenus des éléments clés pour effectuer des fonctions de transmission et de réception à large bande dans les réseaux de communication optique. Cette thèse fournit des informations sur les lasers à semi-conducteurs hybrides (SCL) constitués d'une couche active de matériaux III-V sur un substrat de silicium sur isolant (SOI) pour exploiter conjointement les propriétés d'émission des couches III-V et les nombreux avantages offerts par Si pour les applications sur chip. En raison des développements technologiques importants en électronique, cette approche hybride est bien positionnée pour répondre aux exigences de transmission et d'accès à courte distance à moindre coût. Cependant, plusieurs défis subsistent, comme le manque de sources lumineuses efficaces et de dispositifs sans isolateur.

Du point de vue de l'intégration monolithique d'une intégration hétérogène PIC, il est essentiel de s'assurer que les réflexions parasites qui peuvent provenir de plusieurs emplacements n'affectent pas la stabilité du laser. Plus précisément, les composants hybrides III-V sur Si semblent avoir de nombreuses sources potentielles de réflexions qui peuvent créer des centimètres de cavités externes en plus de celles naturellement produites à l'intérieur de la fibre de l'ordre de plusieurs mètres. Par conséquent, le travail présenté ici vise à comprendre le comportement des SCL III-V/Si lorsqu'ils sont soumis à une variation de réaction optique, explore les aspects fondamentaux de la dynamique chaotique et étudie les applications potentielles adaptées aux systèmes de télécommunications optiques dans une tentative de répondre aux exigences existantes en matière de haute vitesse.

**Title :** Effects of Dynamics and Optical Feedback on Hybrid III-V/Si Semiconductor Lasers

**Keywords :** Photonic integrated circuits, semiconductor lasers, optical feedback

**Abstract :** Photonic Integrated Circuits (PIC) have become key elements to perform broadband transmission and reception functions in optical communication networks. This thesis provides information on hybrid semiconductor lasers (SCL) consisting of an active layer of III-V materials on a silicon-on-insulator (SOI) substrate to jointly exploit the emitting properties of III-V layers and the numerous advantages offered by Si for on-chip applications. Due to the significant technological developments in electronics, this hybrid approach is well positioned to meet the high volume requirements for short distance transmission and access networks at a lower cost. However, several challenges still exist such as the lack of effective light sources and isolator-free devices.

From a monolithic perspective of a PIC heterogeneous integration, it is essential to ensure that the parasitic reflections that may stem from multiple locations do not affect the stability of the laser. Specifically, III-V hybrid components on Si appear to have many potential sources of reflections that can create centimeter external cavities in addition to those naturally produced inside the fiber in the order of several meters. Therefore, the work presented herein aims at understanding the behavior of III-V/Si SCLs when subjected to a variation of optical feedback, explores the basic aspects of chaotic dynamics, and investigates potential applications suitable for optical telecommunication systems in an attempt to meet the existing and emerging high speed requirements.

It always seems impossible until it's done!

*Nelson Mandela*

This work is dedicated to my parents, my family and friends ...  
Without whom this achievement would not have been possible.

## ACKNOWLEDGEMENTS

First and foremost, I would like to express my most sincere gratitude to my advisor Professor Frederic GRILLOT, who has been extremely supportive of my academic goals and who has actively encouraged me to pursue this significant endeavor. His continuous motivation, patience and scientific guidance cannot be underestimated and have enabled me to overcome the challenges encountered through the rough road of completing my thesis as a part time student despite my professional obligations.

I would also like to extend my deepest appreciation to my thesis committee for their valuable time, consideration, and feedback: Dr. Ammar SHARAIHA, Dr. Vincent RONCIN, Dr. George FISCHER, Dr. Venkataraman SWAMINATHAN, Dr. Vassilios KOVANIS and Dr. Laurent VIVIEN.

Special thanks to Professor Gerard MEMMI, Head of the Computer Science and Network Department for introducing me to Professor Bruno THEDREZ, Head of the Communications and Electronics (COMELEC) School, who gave me the opportunity to join the program at Telecom ParisTech. In addition, I would like to thank Dr. Eric CASSAN, Director of the Electrical, Optical and Bio Doctoral program for his administrative assistance and support throughout the process. I am extremely grateful to all who in one way or another contributed to the completion of this thesis. Particular helpful to me during this time were Dr. Heming HUANG and Dr. Kevin SCHIRES, who provided a great amount of assistance and invaluable contribution to my work. Thank you again for your insightful comments and motivation!

The experimental measurements collected during the course of my thesis were performed using devices fabricated by III-V lab; therefore, I would also like to knowledge their significant support. Thank you! Furthermore, I wish to extend my gratitude to the U.S Army Combat Capabilities Development Command for allowing me to continue my education while serving overseas and to the Office of the Project Manager for Combat Am-

munition Systems for providing me with the flexibility to complete the required work for the remaining part of the program.

Last but not least, I would like to thank my family and friends for their unwavering support throughout this rewarding journey and for believing in me. This work would have not been possible without them!

”We’ll always have Paris!”

## TABLE OF CONTENTS

<b>Acknowledgments</b> . . . . .	v
<b>List of Figures</b> . . . . .	xi
<b>Chapter 1: Introduction and Background</b> . . . . .	1
1.1 Silicon Photonics . . . . .	1
1.2 Applications and Challenges . . . . .	7
1.2.1 Optical Interconnects . . . . .	9
1.2.2 High Performance Computing . . . . .	13
1.3 Overview of III-V/Silicon Hybrid Technology . . . . .	15
1.3.1 Silicon Waveguides . . . . .	15
1.3.2 Hybrid III-V/Si Semiconductor Lasers . . . . .	16
1.4 Organization of the Thesis . . . . .	20
References . . . . .	28
<b>Chapter 2: Principles of Semiconductor Lasers</b> . . . . .	29
2.1 Basic Operation . . . . .	30
2.1.1 Electronic Transitions in Semiconductors . . . . .	30
2.1.2 The Rate Equations . . . . .	35
2.1.3 Optical Gain and Laser Cavity . . . . .	37

2.1.4	Light-Current Characteristic . . . . .	41
2.1.5	Stability Analysis, Relaxation Oscillations and Damping . . . . .	43
2.1.6	Linewidth Enhancement Factor . . . . .	46
2.1.7	Gain Compression . . . . .	48
2.2	Classification of Semiconductor Devices . . . . .	49
2.2.1	Fabry-Perot Lasers . . . . .	49
2.2.2	Distributed Bragg Reflector Lasers . . . . .	50
2.2.3	Distributed Feedback Lasers . . . . .	51
2.3	Semiconductors Under Study . . . . .	53
2.3.1	Tunable Lasers . . . . .	53
2.3.2	Hybrid III-V/Silicon DFB Lasers . . . . .	60
	References . . . . .	68
	<b>Chapter 3: Optical Feedback . . . . .</b>	<b>69</b>
3.1	Optical Feedback Effects on the Optical Spectrum of a Laser Diode . . . . .	71
3.2	Analytical Approach of Optical Feedback . . . . .	74
3.2.1	Rate Equations of a Laser Diode under Optical Feedback . . . . .	74
3.2.2	Feedback-induced Frequency Shift . . . . .	76
3.2.3	Threshold Reduction . . . . .	77
3.2.4	Linewidth Evolution . . . . .	78
3.3	Dynamical Properties of a Laser Diode under Optical Feedback . . . . .	81
3.3.1	Dimensionless Rate Equations with Optical Feedback . . . . .	81
3.3.2	Bifurcation Diagram Representing the Laser Dynamics . . . . .	82

3.3.3	Influence of the Bias Current, the External Cavity Length and the $\alpha_H$ factor on the Bifurcation Diagram . . . . .	84
3.3.4	Phase Diagrams . . . . .	86
3.3.5	Coherence Collapse and Chaos . . . . .	87
	References . . . . .	95
<b>Chapter 4: Hybrid III-V/Si Semiconductor Lasers . . . . .</b>		<b>96</b>
4.1	Devices under Study and Experimental Set-up . . . . .	98
4.1.1	FP Laser . . . . .	103
4.1.2	Tunable Laser . . . . .	108
4.1.3	Hybrid III-V/Si DFB Laser . . . . .	111
4.2	Direct Modulation . . . . .	127
4.2.1	Static Characterization . . . . .	127
4.2.2	High-speed Test Bed Experimental Set-up . . . . .	128
4.2.3	Eye Diagram and Bit Error Rate . . . . .	133
4.3	Conclusions . . . . .	135
	References . . . . .	140
<b>Chapter 5: Hybrid III-V/Si Distributed Feedback Laser with High Quality Factor</b>		<b>141</b>
5.1	Device Under Study . . . . .	143
5.2	Optical Feedback Set-up . . . . .	146
5.3	Results and discussion . . . . .	147
5.4	Physical interpretation . . . . .	150
5.5	Conclusions . . . . .	153

References . . . . . 156

**Chapter 6: Summary and Future Directions . . . . . 157**

    References . . . . . 165

**Vita . . . . . 166**

**List of Acronyms . . . . . 169**

## LIST OF FIGURES

1.1	Cisco’s visual networking index internet protocol traffic forecasts [12]. . . .	2
1.2	Progress in hybrid-silicon photonic integrated circuit technology - Development of chip complexity measured as the number of components per chip [23, 24]. . . . .	4
1.3	Silicon photonics market annual growth [49]. . . . .	8
1.4	Penetration of optical links into communications. Historical roadmap for introduction of optical interconnections into digital systems showing link distance versus link bandwidth, approximate cost per unit gigabit per second of the link and approximate date of commercial introduction [60]. . . .	10
1.5	Connected devices and their impact on cloud and data center traffic [11]. . .	12
1.6	Silicon waveguides developed by III-V lab-Leti technology [74]. . . . .	16
1.7	III-V on silicon epitaxy and bonding [74]. . . . .	17
1.8	III-V/Si heterogeneous integration approaches: (a) UCSB/Intel with low bonding thickness and non-encapsulated Si waveguides [81] (b) IMEC platform uses BCB bonding [80]. . . . .	18
1.9	III-V/SOI laser process [75]. . . . .	19
1.10	(a) Cross section of the III-V/SOI and (b) Scanned electron image of the structure [74]. . . . .	19
2.1	Schematic energy-level diagram: stimulated absorption, spontaneous emission, stimulated emission) [15]. . . . .	31

2.2	Electron energy vs $k$ vector: Band structure of a direct band-gap III-V semiconductor showing valence heavy-hole (hh) band, conduction band $e$ , minimum conduction band energy $\mathbf{CB}_{\min}$ , and band-gap energy $E_g$ . The semiconductor is doped p-type, and at low temperature the Fermi energy is $E_F$ and the Fermi wave vector is $k_{F_{hh}}$ . Electrons in the conduction band can make a transition from a state characterized by wave vector $\mathbf{k}$ and energy $E_k$ in the conduction band to wave vector state $\mathbf{k}$ energy $E_K - \hbar\omega$ in the valence band by emitting a photon of energy $\hbar\omega$ [15]. . . . .	33
2.3	Schematic illustration of the gain curve and longitudinal modes of a semiconductor laser: cavity modes are given by $m\frac{\lambda}{2} = nL$ , where $m$ is an integer and $n$ the effective refractive index [22]. . . . .	40
2.4	Output power versus current characteristics of a laser and its corresponding optical spectrum: below the threshold only spontaneous emission is important; above the threshold, the stimulation emission power increases while the spontaneous emission is clamped at its threshold level [23, 16]. . . . .	42
2.5	Fabry-Perot: Device schematic and laser spectrum [39]. . . . .	49
2.6	(a) DFB structure laser structure; (b) Lasing emission output; (c) Optical spectrum [13]. . . . .	51
2.7	First fabricated DFB structure [41, 42]. . . . .	51
2.8	Tunable single laser and gain profile [53]. . . . .	54
2.9	Tunable laser based on mirrors with periodic spectra: (a) Schematic of a SG-DBR displaying the four sections used to select the power and desired channel; (b) Vernier effect, two reflection combs from mirror 1 and mirror 2 [53]. . . . .	55
2.10	Reflectivity spectrum of the sample grating mirrors showing the multiple mirror peaks to cover the tuning range [51]. . . . .	56
2.11	(a) Schematic of the hybrid III-V/Si tunable laser and (b) Stack structure of the device [57]. . . . .	57
2.12	Schematic of a double RR laser design [57]. . . . .	58
2.13	(a) Operation principle of a double RR filter, (b) Response of the device after tuning the ring with the smaller FSR, thus having a new coincidence with a longer wavelength [59]. . . . .	59

2.14	Hybrid silicon structures where the gain material is bonded to the silicon waveguide. The laser cavity can be implemented either in the III-V material or in the SOI material [60]. . . . .	60
2.15	3D view of a III-V on Si waveguide. The width $W_{Si}$ of the Si waveguide controls the confinement in the III-V region. [59]. . . . .	61
2.16	Scanning electron microscope image of (a) a Bragg grating and (b) a focusing grating coupler [57]. . . . .	62
2.17	III-V on silicon DFB structure. (a) Longitudinal cross section. Grating is made on top of the silicon waveguide. (b) Transverse cross section. DFB parameters depends on the rib width $W_{Si}$ . (c) Top view featuring the slab (light blue), the waveguide (blue) and the etched region (yellow). A $\lambda/4$ phase shift is inserted in the centre of the cavity [57]. . . . .	62
3.1	Semiconductor laser subject to optical feedback [4]. . . . .	69
3.2	Cartography of optical feedback regimes in a DFB laser as a function of the external cavity length and the feedback strength [14]. The optical spectra on both sides illustrate the laser dynamics under optical feedback [15]. . . .	72
3.3	Threshold reduction with optical feedback, experimentally and theoretically. The transmittance in $x$ -axis is proportional to the feedback strength [26]. . . . .	77
3.4	Evolution of the laser linewidth as a function of the feedback strength, for several initial phase conditions [32]. The roman numerals I-IV corresponds to the regimes given in fig 3.2. . . . .	80
3.5	Ellipse of the feedback modes and anti-modes. In blue circles, stable external cavity modes, and in red circles, unstable anti-modes [33]. . . . .	81
3.6	a) Numerical bifurcation diagram for $T = 1700$ , $P = 0.5$ , $\theta = 500$ ( $L_{ext} \approx 30$ cm) and $\alpha_H = 3$ . b) Corresponding time trace for $\eta = 0.001$ . c) Time trace for $\eta = 0.0027$ . d) Time trace for $\eta = 0.0042$ [33]. . . . .	83
3.7	Evolution of the bifurcation diagram, calculated by increasing the feedback strength for $T = 1700$ , as a function of the main parameters. First row: evolution with the pump current, for $\alpha_H = 3$ and $\theta = 500$ . a) $P = 0.02$ . b) $P = 0.5$ . c) $P = 1$ . Second row: evolution with the external cavity length, for $\alpha_H = 3$ and $P = 0.5$ . d) $\theta = 50$ ( $L_{ext} \approx 3$ cm). e) $\theta = 500$ ( $L_{ext} \approx 30$ cm). f) $\theta = 1000$ ( $L_{ext} \approx 60$ cm). Third row: evolution with the $\alpha_H$ -factor, for $P = 0.5$ and $\theta = 500$ . g) $\alpha_H = 1$ . h) $\alpha_H = 3$ . i) $\alpha_H = 5$ [33]. . . . .	85

3.8	Numerical time traces and associated phase diagrams [47]. . . . .	87
3.9	Experimental phase diagrams showing the route to chaos [41]. . . . .	87
3.10	Optical and electrical spectra of a DFB quantum well laser under optical feedback, presenting the progressive appearance of coherence collapse [33].	88
3.11	Mapping of the appearance of LFF as a function of the feedback strength and the bias. The LFF regime is depicted in light gray. The dark-gray region embedded in the LFF regime corresponds to the region of coexistence of the stable emission state and the LFF state. The unshaded region encompassed by the dashed line corresponds to the continuous transition between the LFF regime and the fully developed coherence collapse regime. current [57].	90
4.1	Schematic view of the FP (top) and TUL (bottom) under study, with the Si waveguides shown in grey. The lettered sections correspond to (a) and (e) vertical couplers, (b) high-reflectivity DBR, (c) III-V gain section, (d) low-reflectivity DBR, and (f) Si rings. The dotted red line on the TUL design shows where the samples used in this study were cleaved. . . . .	99
4.2	(a) Schematic and (b) structure of the device studied, showing the Si waveguide (yellow) and the III-V material (green). The vertical couplers are represented in (a) at both extremities of the Si waveguide. . . . .	100
4.3	Experimental set-up. The blue and red arrows show the short and long external cavities, respectively. The analysis block consist of a combination of a power-meter as well as an optical and an electrical spectrum analyzer. .	101
4.4	Evolution of the coupled light against the voltage applied to the piezoelectric actuator for different fiber displacements along the vertical axis. . .	103
4.5	Top, optical spectrum evolution of the FP laser for two randomly selected positions of the cleaved fiber. Bottom, excerpts from (a) showing spectra at (c) 40 and (d) 80 mA. . . . .	104
4.6	Coupled light evolution for both the voltage applied to the piezoelectric actuator (controlling the short cavity-feedback) and the long-feedback strength. The same 3D plot is shown from two angles: one revealing the periodicity of the short-feedback for a long-feedback strength of 0% (blue curve), the other for a long-feedback strength of 7.6% (red curve). . . . .	106
4.7	Evolution of the voltage applied to the piezoelectric actuator for (a) the coupled power, and the optical spectrum with a long-feedback strength of (b) 0% and (c) 7.6%. . . . .	107

4.8	Evolution of the electrical spectra for the following piezo-micropositioner voltages: (a) 0.03 V, (b) 0.1 V, (c) 0.14 V. The different long feedback strengths corresponds to 0% (black curves), 4% (blue curves) and 7.6% (red curves). . . . .	108
4.9	Mapping of the (a) optical and (b) electrical spectrum of the free-running TUL as a function of the bias current. . . . .	109
4.10	Mapping of the electrical spectrum of the TUL with bias current (a) in free-running operation and (b) under long-cavity feedback with a 7.5% strength. The two vertical red lines are measurement artifacts stemming from the RF spectra processing. . . . .	110
4.11	Experimental set-up; PM: power-meter, OSA: optical spectrum analyzer, ESA: electrical spectrum analyzer. . . . .	112
4.12	(a) Applied current against the output light intensity - Evolution of the power couple using an AR-coated lensed fiber against the bias current applied to the free-running device. (b) Optical spectrum of the laser for $I = 140$ mA. . . . .	113
4.13	Evolution of the ROF with the square root of the current overdrive above threshold. . . . .	114
4.14	Solitary Characteristics of a hybrid III-V/Si DBF Laser at room temperature for different bias currents (a) RF Spectrum and (b) Evolution of the ROF. . .	115
4.15	Evolution of the (a) Optical and (b) RF spectra following the route to chaos under long feedback using an AR-coated lensed fiber. . . . .	116
4.16	Evolution of the optical spectra of (a) a conventional III-V laser and (b) hybrid III-V/Si DFB laser under long optical feedback strength using an AR-coated lensed fiber. . . . .	117
4.17	Variation of the power coupled with the cleaved fiber as a function of the voltage applied to the piezoelectric actuator. Two measurements for different fiber positions are presented in black and grey. . . . .	118
4.18	(a) Variation of the power coupled with the cleaved fiber within one period when the fiber is moved away (black) and towards (red) the laser. The gray dashed line represents the power coupled when using the AR-coated lensed fiber. (b) Evolution of the optical spectrum when using the AR-coated lensed fiber. (c), (d) Evolution of the optical spectrum when moving the fiber away or towards the laser, respectively. . . . .	119

4.19	Evolution of the (a) optical and (b) RF spectra within one period. The green dashed line shows the evolution of the ROF. . . . .	121
4.20	Bifurcation diagrams as a function of the short feedback phase under (a) minimum and (b) maximum long feedback strength. . . . .	122
4.21	Evolution of optical (left) and RF (right) spectra with the position of the cleaved fiber for long feedback strengths of (a), (b) -79 dB, (c), (d) -42 dB, (e), (f) -36 dB and (g), (h) -26 dB. In (h) the black line shows the chaos bandwidth under long feedback only, and the green dashed line shows the evolution of chaos bandwidth with the phase of the short feedback. . . . .	123
4.22	Evolution of the optical (left) and RF (right) spectra with the long feedback strength for three positions of the cleaved fiber. a) and b) correspond to a feedback phase of $1.9\pi$ (minimum ROF, stable). c) and d) correspond to a feedback phase of $0.3\pi$ (maximum ROF, stable). e) and f) correspond to a feedback phase of $0.25\pi$ (strongest oscillations). . . . .	125
4.23	Optical (left) and RF (right) spectra under maximum long feedback and their bandwidth, the dashed lines showing the free-running spectra as reference. The black curve corresponds to maximum long feedback alone. The blue (resp. red) curve corresponds to both feedbacks with minimum (maximum) ROF. The green curve corresponds to both feedbacks with strongest periodic oscillations. . . . .	126
4.24	Solitary Characteristics of a hybrid III-V/Si DBF Laser at $I = 141$ mA for $T = 20^\circ\text{C}$ and $35^\circ\text{C}$ (a) L-I curve and (b) Optical Spectrum . . . . .	128
4.25	Experimental set-up used for optical feedback investigation. . . . .	129
4.26	Optical Spectra of the hybrid III-V/Si DFB device at $20^\circ\text{C}$ and $35^\circ\text{C}$ under different feedback strengths: (a). Full spectrum, at $T = 20^\circ\text{C}$ ; (b) Zoomed-in spectrum at $T = 20^\circ\text{C}$ ; (c) Full shifted spectrum, at $T = 35^\circ\text{C}$ and; (d) Zoomed-in shifted spectrum at $T = 35^\circ\text{C}$ . . . . .	130
4.27	Critical feedback at $20^\circ\text{C}$ : (a) Feedback sensitivity in the optical domain; (b) Optical Spectrum; (c) Feedback sensitivity in the frequency domain and; (d) RF spectrum. The green dotted line at about -16 dB equivalent to about 2.5% of the injected optical feedback indicates the static critical feedback level, $r_{crit}$ at which the laser begins to destabilize. . . . .	131

4.28	Critical Feedback at 35°C: (a) Feedback sensitivity in the optical domain; (b) Optical Spectrum; (c) Feedback sensitivity in the frequency domain and; (d) RF spectrum. The green dotted line is equivalent to about 2.2% of the injected optical feedback indicates the static critical feedback level, $r_{crit}$ at which the laser begins to destabilize. . . . .	132
4.29	Eye diagrams in (a) back-to-back (solitary) for T = 20°C, (b) after 10 km transmission (solitary) T = 20°C, (c) back-to-back (solitary) for T = 35°C, (d) after 10 km transmission (solitary) T = 35°C . . . . .	134
4.30	Bit Error Rate plots after 10-km transmission distance at different optical feedback strenghts for (a) T = 20°C, (b) T = 35°C. . . . .	135
5.1	Relative intensity noise measurements at bias current of 120 mA with similar threshold values for: (a) A standard $\lambda/4$ phase shifted hybrid DFB laser design (top) and a high- $Q$ hybrid laser (bottom) [11]. . . . .	142
5.2	(a) Schematic of the high- $Q$ DFB laser cross-section; (b) III-V total overlap versus Si waveguide width . . . . .	144
5.3	Top view of of the high- $Q$ . The 300 nm slab is in light blue, the 500 nm waveguide in darker blue and the 30 nm tooth etched regions in yellow. The grating has two regions: a parabolic tapered grating in the centre and a uniform grating at each side . . . . .	144
5.4	(a) Optical spectrum of the high- $Q$ DFB laser and L-I curve (inset) at $3 \times I_{th}$ ; (b) The calculated $Q$ factor and threshold current as a function of the total cavity length. . . . .	145
5.5	High- $Q$ DFB laser at T = 20°C, 25°C, 30°C, and 35°C: (a) L-I curve; (b) Optical spectrum . . . . .	145
5.6	Experimental set-up used for optical feedback investigation. . . . .	147
5.7	(a) Optical and (b) electrical spectral map of the high- $Q$ DFB laser with respect to the optical feedback strength. . . . .	148
5.8	(a) Optical and (b) RF spectral map of a conventional QW DFB laser; eye diagrams at (c) level (I) and (d) level (II) marked in the map. . . . .	148
5.9	(a) BER characteristics of the high- $Q$ laser with (blue and cyan triangles) and without (red and magenta squares) feedback; eye diagrams (b) in B2B without feedback and (c) with maximal feedback after transmission. . . . .	150

## Foreword

Photonic Integrated Circuits (PIC) have become key elements to perform broadband transmission and reception functions in optical communication networks. There are currently two parallel approaches developed to manufacture PICs: monolithic integration on Indium Phosphide (InP) [1] and integration on Silicon (Si) [2]. The first approach has reached a certain level of maturity for metropolitan networks transmission and long distance applications. However, the second approach is actively in a phase of rapid development and continues to receive a great level of attention from different communities for its vast potential to reach high volume production at low cost. Due to the significant technological developments in electronics, the second approach is well positioned to meet the high volume requirements for short distance transmission and access networks. However, major difficulties in the development of Si on PICs include the lack of effective light sources and isolator-free devices. The most promising solution is the incorporation of an active layer of III-V semiconductor on a silicon-on-insulator (SOI) substrate to jointly exploit the emitting properties of III-V heterogeneous materials and the numerous advantages offered by Si [3]. From a monolithic integration perspective of all these photonic components, it is essential to ensure that the parasitic reflections that may stem from multiple internal and external locations do not affect the stability of the laser. Specifically, III-V hybrid components on Si appear to have many potential sources of reflections that can create centimeter external cavities in addition to those naturally produced inside the fiber in the order of several meters. Therefore, the work presented herein aims at understanding the behavior of III-V/Si semiconductor lasers (SCL) when subjected to a variation of optical feedback, explores the basics aspects of chaotic dynamics, and investigates potential applications suitable for optical telecommunication systems.

## REFERENCES

- [1] K. Schires, N. Girard, G. Baili, G.-H. Duan, S. Gomez, and F. Grillot, “Dynamics of hybrid III-V silicon semiconductor lasers for integrated photonics,” *IEEE Journal of Selected Topics in Quantum Electronics*, vol. 22, no. 6, pp. 43–49, 2016.
- [2] K. Schires, G. Baili, N. Girard, G.-H. Duan, S. Gomez, and F. Grillot, “Nonlinear dynamics of hybrid III-V/silicon laser poster,” 2016.
- [3] S. Gomez, K. Schires, A. Gallet, G. Baili, G.-H. Duan, and F. Grillot, “Wideband chaos in hybrid III-V/silicon distributed feedback semiconductor lasers under optical feedback,” in *Physics and Simulation of Optoelectronic Devices XXV*, B. Witzigmann, M. Osiński, and Y. Arakawa, Eds., SPIE, 2017.

# CHAPTER 1

## INTRODUCTION AND BACKGROUND

### 1.1 Silicon Photonics

The allure of silicon photonics (SiPh) lies in the potential for production of low-cost and compact circuits that integrate photonics and microelectronics on a single PIC [1, 2] to enable faster data transfer over longer distances at higher speed rates. Historically, the main use of Si-based photonics has been primarily for optical communications and optical interconnects in microelectronic circuits [3], where optical transceivers are the fundamental building blocks of the data center interconnects (DCIs). However, PICs are increasingly becoming more appealing to other markets due to the promising benefits these devices can offer to a wide range of applications [4] to include high performance computing (HPC) and optical signal processing technologies [5, 6]. Additional emerging applications for PICs also reside in the area of healthcare, sensing, spectroscopy and measurement instrumentation among others for both the military and the private sector domain [7, 8, 9].

From the telecommunication industry point of view, the ability to handle the unprecedented increase in volume and complexity of data traffic as more devices and users become connected is a continuous challenge faced by data providers [10]. It is no surprise that as new digital services and high power consumption applications are released such as video and gaming, the amount of bandwidth growth becomes more critical in order to handle a higher rate of users and data traffic. For instance, the average smartphone user in 2015 consumed more data in less than a minute than a mobile user did in an entire month in 2000 [11]. Cisco's visual networking index (VNI) forecast projects global internet protocol (IP) traffic to nearly triple from 2017 to 2022. As shown in fig. 1.1, the overall IP traffic is expected to grow to 396 exabytes (EB) per month by 2022, up from 122 EB per

month in 2017, a compound annual growth rate (CAGR) of 26% [12] reaching the so called "Zettabyte Era". Therefore, existing and future data centers (DCs) must adapt to the fast growing bandwidth demand to enable large amounts of data to be transferred reliably at higher speed rates in order to satisfy the hyper-connectivity levels required by networked end-user devices and the internet of everything (IoE) [13]. Consequently, the use of PICs in the telecommunications domain continues to increase due the enormous data capacity this technology can provide.

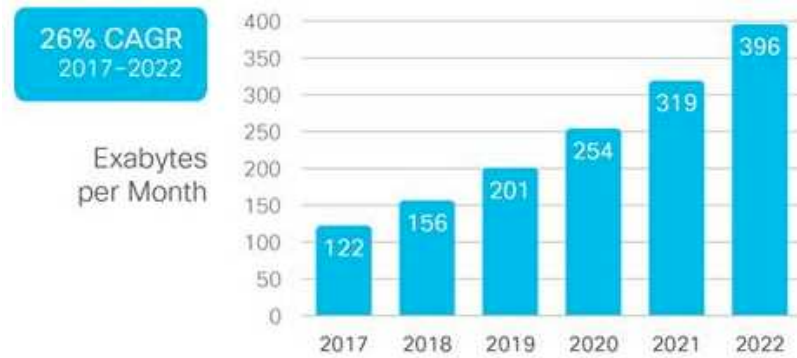


Figure 1.1: Cisco's visual networking index internet protocol traffic forecasts [12].

In an attempt to meet new optical network requirements and fundamentally improve the way data is moved using smaller form factor and low power devices with maximum functionality; various alternatives such as SiPh are currently being investigated as part of the proposed solution combined with coherent communication techniques to achieve higher functionality and overcome limitations of legacy systems. Several research efforts have already revealed promising results to meet the aforementioned needs and associated challenges hence, SiPh is now seen as a rapidly evolving candidate solution of choice for the next generation of high frequency circuits. This technology provides numerous advantages over traditional optics and communication networks by delivering enhanced bandwidth and significant size reduction through the well-established wafer scale manufacturing process, which in turns leads to remarkable cost savings while reducing networking bottlenecks and enhancing compute capacity. In addition, the integration of optical functions on a micro-electronic chip brings many innovative perspectives, along with the possibility to improve

the performance of converged photonic and electronic circuits [14] altogether such as the ability to perform signal processing closer to the receiver and the emitter. This novel approach uses Si as the medium for optical signals, allowing much faster digital signaling than is currently possible with traditional electron-based semiconductor devices. The high refractive index contrast of Si allows for a dense integration of optical building blocks, ideal for accommodating thousands of photonic components on a single chip [15]. PICs should then lead to a drastic reduction of the circuit size and allow novel ways of handling and transmitting data, resulting in significant performance improvements overall [6, 16]. As a result, SiPh is considered a disruptive technology meant to achieve a new breed of monolithic opto-electronic devices for a potentially low cost Si process with the ultimate goal of delivering connectivity everywhere, from the network to the chip-to-chip level for increased capacity and improved functionality [17].

This ongoing digital transformation of data analytics and the IoE will drastically force mobile providers to move faster than ever towards the next generation of mobile communications to meet the forecasted bandwidth demand. Therefore, improvements in the existing network infrastructure to include scalability of advanced DCs must be edge-centric, cloud-enabled and data-driven [18]. Thus, building on the already established complementary metal-oxide-semiconductor (CMOS) large-scale fabrication methods, techniques and commercially proven processes developed for the microelectronics industry is critical for creating PICs with a high density of optical components in a timely and cost effective manner to address existing capability gaps [19]. Since the first demonstration of the heterogeneous device platform in 2005 [20], the success of the hybrid-silicon technology has been inevitable. Hybrid III-V SCLs have played a key role in the functionality of DCIs and have without a doubt achieved substantial performance characteristics over the last decade. In this thesis several hybrid SCLs configurations are fully exploited to assess their potential to serve as light sources in PICs and optical isolator-free applications. Published results have revealed that by varying the conditions of the design and fabrication process such as

geometry, cavity length and so on, one can impact and optimize the response of a SCL as reported in [21] to maximize performance based on the identified application.

Significant advancements in SiPh have already been proven and different approaches to develop materials platforms for photonic integration that can conceivably deliver enhanced performance with a monolithically integrated solution have successfully demonstrated high reliability [22]. These approaches include: 1) pure III-V semiconductor material (e.g., InP); 2) SOI; 3) heterogeneous integration of III-V on SOI and 4) direct epitaxial growth of III-V on Si [23]. The level of integration and PIC complexity as a function of time for the first three approaches is illustrated in fig. 1.2 to show both the progress of InP-based and hybrid III-V/Si PICs. It is clear that InP-based monolithic integration has increased over the last two decades. However, hybrid III-V/Si PICs are catching up exponentially [24].

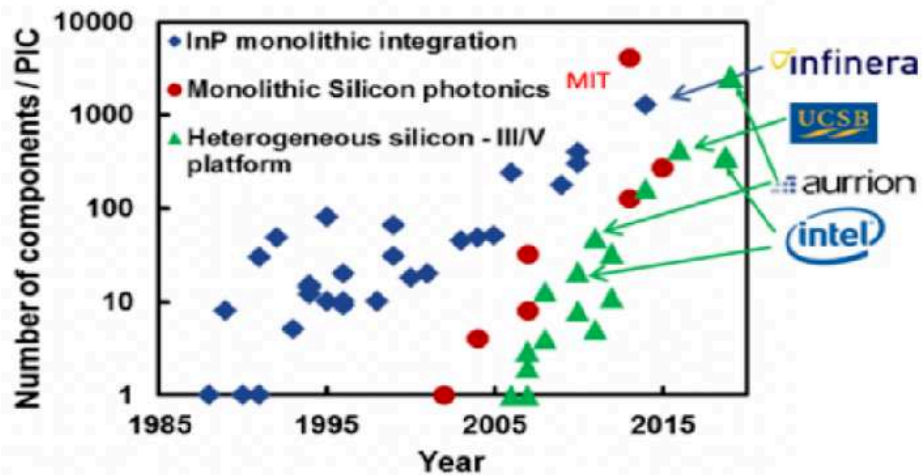


Figure 1.2: Progress in hybrid-silicon photonic integrated circuit technology - Development of chip complexity measured as the number of components per chip [23, 24].

The last approach, direct epitaxial growth of III-V layers on Si remains a challenge. Although recent efforts have reported substantial breakthroughs on this approach [25, 26, 27], several technology constraints still exist due to the restrictions posed by the indirect gap of Si that can result in a much smaller absorption coefficient [28]. Therefore, current research is also strongly focused on heterogeneous integration of III-V semiconductors on Si through wafer bonding techniques [29, 30, 31]. The main difficulty lies in material

property mismatches among different elements, such as the introduction of threading dislocations (TD) in the III-V material due to the large lattice-constant mismatch between Si and the III-V region in addition to thermal expansion, which lead to a high-density of defects, cracking, and delamination [32].

Practical monolithic or hybrid integrated light sources and on-chip optical isolators with low risk of short-cavity reflections and the desired performance are still missing, thus, current light sources on Si have to be either bonded or coupled off chip. Electronically pumped Si based light sources with enough light generating efficiency heterogeneously integrated with III-V materials on-chip are actively being investigated [33] in order to achieve the full potential of PICs. The future of PICs currently relies on complex designs where light is coupled between III-V and Si waveguides. Light sources within a PIC are destined to be monolithically integrated close to other optical components, all sources of optical reflections. Such complex devices thus require careful study of their dynamical properties, in particular when a laser may be subject to any external light fed back into the cavity [20] as discussed in Chapter 4. Therefore, the lack of on-chip source limits the potential applications of PICs, which pushes users such as Cisco, Luxtera, Acacia and Petra among many others to heavily rely on external III-V lasers as the light source for monolithic Si photonic approaches [23, 34, 35].

In addition, no on-chip optical isolators with low risk of short-cavity reflections, sufficient isolation ratio, low loss and the sought performance have yet been reported at the required operating wavelength, however, significant progress has already been demonstrated. Optical isolators are extremely important devices because of their unique functionality to shield the SCL from backward propagating light. These components are necessary to protect SCLs from unwanted optical feedback [28] that can potentially destabilize their performance and in order to maintain the desired lasing frequency steady [36]. Therefore, investigating the impact these parasitic reflections have on the performance characteristics of SCLs due to the tight heterogeneous integration of passive and optical functionalities

remains of first importance for PIC integration in the telecommunications industry.

Progress in III-V foundry processes has already made possible monolithic integration of both passive (isolators, circulators, couplers, etc.) and active components (active isolators, lasers, modulators, amplifiers and photo-detectors) with very high densities enabling the development of complex circuits with a steadily increasing number of components [37, 38, 39, 40, 41, 42] for PICs development. Novel semiconductor optical amplifiers (SOA) are also very attractive devices for optical communications and will also play a key role in optical fiber transmission and data processing due to their capability to operate as multi-functional devices [43]. SOAs can enable increased output power and signal pre-amplification. Their ability to control the output power levels from individual transmitters by altering them external to the cavity in addition to their high gain and low power consumption makes SOAs indispensable amplifier blocks in complex PICs [44]. These devices can be employed as stand alone devices or monolithically integrated with a LD for high power, long haul applications, or an electro-absorption modulator (EAM) for metro-core applications. Published literature have demonstrated the multi-functional capability of SOAs by combining optical amplification with either photodetection, modulation, wavelength conversion among many others. Different applications for SOAs have been identified for data optimization such as the one reported in [45, 46] where a multi-section SOA is used as an in-line photodetector in the presence of bi-directional transmission for signal detection in order to minimize crosstalk.

Multiple efforts have emerged from both industry and academia addressing the associated challenges with SiPh. For instance, the University California Santa Barbara (UCSB) has demonstrated promising results with their unique approach of utilizing a Si waveguide mode evanescently coupled to III-V semiconductor multiple quantum wells (QWs), thus combining the advantages of high-gain III-V materials and the integration capability of Si to develop light sources. In this case, the difficulty of coupling to Si-based passive optical devices was overcome by confining most of the optical mode into the Si. The approach

taken restricts the laser operation to the region defined by the Si waveguide, relaxing the requirement for high precision pick and placing of the III-V device on the Si substrate. Thus, concerns over process compatibility of disparate components were minimized because the bonding procedure used to attach the III-V device and the Si is positioned at the back end of the process flow [22].

The growing need of novel devices required to address these major technology gaps as well as the reliable and functional integration of embedded systems remains of paramount importance and extremely necessary to achieve the craved power and efficiency [17]. The need to learn not only about the advantages offered by hybrid III-V on Si light sources but also about their strengths and limitations is in fact the motivation of the work herein.

## **1.2 Applications and Challenges**

Telecommunications network systems are now facing an explosive traffic increase with a growth rate of more than 30 % per year [47]. The main industrial drive in the SiPh domain is in optical interconnects [48] with the intent to replace existing electrical links unable to provide the required network scalability for the increased data traffic to support the next generation of DCs. Therefore, this arena is a rapidly growing field of opportunity for optics and photonics technology. Fig. 1.3 illustrates the forecasted SiPh market size in millions from 2017 - 2026 at a CAGR of 20.4 % based on trends and information collected from the key players in this market globally [49].

Much of the traffic on the DC interconnection is extensively associated with machine learning and dominated by video services [14, 50]. As server output data rate extends beyond 10 Gbps, novel solutions will be needed to increase the speed of short-reach optical interconnects at least 4 fold to 40 Gbps, 120 Gbps and 480 Gbps, while keeping the same power-and-space profiles of existing modules [51]. In order to progressively achieve the higher bandwidth demand and increased data rates for capacity-building infrastructure; each discrete component used in electro-optical devices has been redesigned for integration

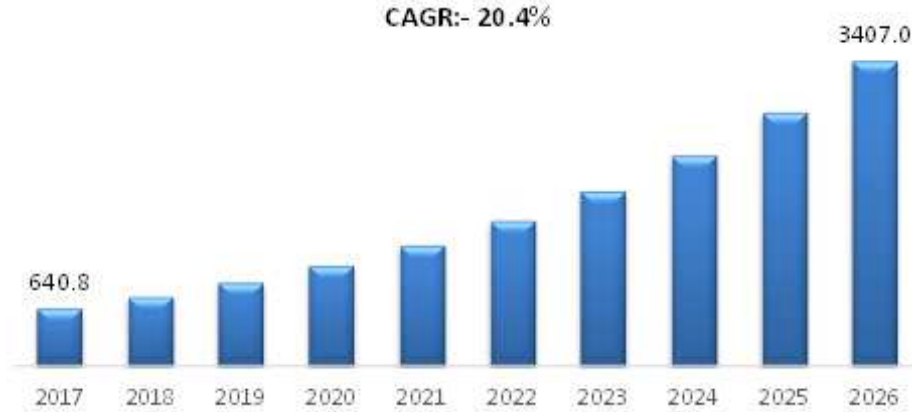


Figure 1.3: Silicon photonics market annual growth [49].

on Si with the intention of taking advantage of the high-density PIC approach to incrementally transform the network ecosystem. The number of efforts conducted by both academic and industry have led to the development of innovated technical solutions for a variety of domains as described in [5, 6]. These efforts include the realization of novel integrated modulators, photodetectors, isolators, polarization controllers, amplifiers, as well as novel laser sources [52].

While the performance specifications for long-haul telecom backbones cannot yet be met with PICs, shorter-range communication (metropolitan networks, fiber-to-the-home) and DCIs (rack-to-rack, board-to-board) consider SiPh a very attractive technology to address existing network challenges [53]. Recent advances in DCs and informatics [14, 50] reveal how photonic integration will become increasingly used for data transmission, either inside a chip or for short-access and eventually for long-haul telecommunications networks to meet the growing high bandwidth requirements [16, 54]. The use of SiPh in the long-haul network, based on coherent optical communications will set the path for the next industrialization of high performance opto-electronics transceivers at a lower cost with the sought functionality [55]. In order to provide speedy and unfailingly connectivity, DCs need to talk to each other reliably to successfully share data and connect. Current standards are based on 100 Gbps, however, growing bandwidth demands resulting from cloud based applications and multi-media demand will required new standards based on 200-400 Gbps [55].

Since the most effective transport for optical interconnects is high-speed packet-optical connectivity such as coherent optics [56]; SCLs are primarily used as light sources in the optical links.

In this section, I will expand on how SiPh is being employed for various applications with emphasis on DCIs. These devices play a critical role in long-haul, metropolitan and access networks as they efficiently connect regional and access networks DCs from multiple locations enabling the transmission of critical assets over various distances. Short-reach intra-data center interconnects with photonic integration are also critical for building scalable datacenter clusters [51]. This high pace development of state-of-the-art devices and specifically DCIs is driven by emerging services and large data sets derived from machine learning applications to improve the user's experience. The increased bandwidth requirement is indisputably paving the way for new endeavors to achieve enhanced performance, lower cost and higher integration.

### 1.2.1 Optical Interconnects

Modern DCs heavily rely on interconnects for delivering critical communications connectivity among numerous servers, memory, and computation resources [50]. In fact, we can say that the existing data server infrastructure is almost completely based on optical interconnects [57]. The rapid evolution of the IoE along with the immediate need to remain widely connected is pushing for the development of higher speed interconnects to provide the distributed processing, computational power and memory required by the next-generation of DCs. Among the various technologies for dealing with this unavoidable bandwidth demand, SiPh holds the most potential for providing high density photonics integration with ultra-small footprint, low power consumption and affordable devices to deliver the scalability [58] and increased functionality necessary to address existing bottlenecks in PICs [59]. Therefore, it is important to examine the history of optical data links penetration into communications to clearly visualize their continuous evolution over the

past 30 years. Fig. 1.4 shows a general perspective of the rate of penetration of optics versus the link distance and the bandwidth. The vertical axis represents the minimum range of the link, and the upper horizontal axis represents the bandwidth per fiber connector.

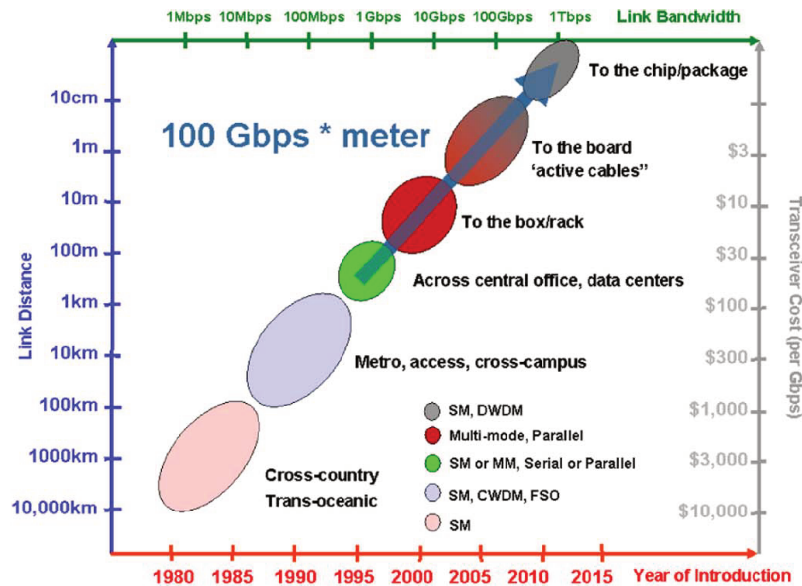


Figure 1.4: Penetration of optical links into communications. Historical roadmap for introduction of optical interconnections into digital systems showing link distance versus link bandwidth, approximate cost per unit gigabit per second of the link and approximate date of commercial introduction [60].

The approximate trend, across five orders of magnitude of bit rates and distance in fig. 1.4, suggest that over the past several decades, optical links have achieved bandwidth-reach product performance exceeding  $10^6$  Gbps-m with single-mode solutions and  $10^3$  Gbps-m with multimode fiber solutions, a successive penetration into the interconnection hierarchy every five years [19, 60, 61].

On the electrical side, copper-link solutions, including digital subscriber line (DSL), asymmetric DSL, and other twisted pair solutions, have generally followed the 10 Mbps-m performance trend [60]. Continuing this trend suggests that in the years to come, optical links can be expected to reach right to the chip-scale package on a printed circuit board, representing link distances below 1 m to deliver higher bandwidths. Although many may see this prediction as a radical departure from current design norms, recent efforts indicate

that the required technologies are well under development. Central to this case are optical links that demonstrate higher data capacity in addition to a power dissipation benefit over electrical solutions as reported in [62] when comparing an electrical copper-based backplane and a full-optical fiber-based backplane using a vertical cavity surface emitting laser (VCSEL). In this study, the electrical solution with equalization at a bit rate around 20-22 Gbps showed a power consumption per Gbps higher than 0.8 mW. However, using the same power budget, the optical backplane was able to reach 25 Gbps with a power consumption per Gbps lower than 0.2 mW. This is more than 4 times less than the electrical solution. For many years, electrical interconnects have dominated ultra-short reach links, however, existing electrical interconnects cannot handle the data capacity expected in the years to come because of the required level of integration density. Electrical solutions are close to reach their limit; therefore, different alternatives must continue to be explored such as optical technologies. Optical solutions have already demonstrated the ability to provide higher capacity over longer distances than electrical transmission systems in addition to reduced losses, coupling efficiency and lower costs among many other benefits.

Fig. 1.5 displays the estimated annual growth rates and the impact connected devices and additional data services will have on the cloud and DC traffic. Undoubtedly, the network transformation to support such demand is imminent. Therefore, optical interconnects with integrated optics on a single chip continue to be vigorously investigated as a viable solution because of their promising capability to replace bulky components as well as extremely energy and cost prohibited copper interconnects used for electronic data transmission. In addition, optical interconnects have negligible frequency dependent loss, low cross talk and high bandwidth [63]. Recent efforts on optical links based on PICs for short distance applications have previously been proposed and have demonstrated significant energy efficiency improvements. This includes higher bandwidth due to the reduced coupling loss since optics can transport more data at a significantly lower power compared to electronic transmission [11], which makes this disruptive technology very appealing to data providers.

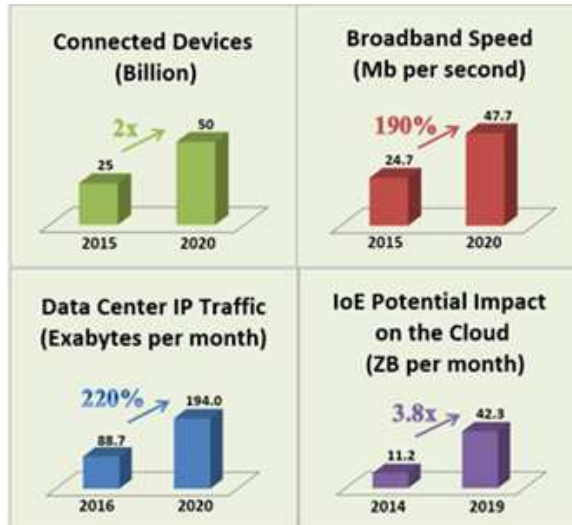


Figure 1.5: Connected devices and their impact on cloud and data center traffic [11].

To achieve future network scalability, which must be able to handle ultra-large data flows and bandwidth-intensive requests, existing DCs architecture must undergo a fundamental shift to progressively introduce optical technologies at different system levels to enable a variety of transparent network or all-optical networking schemes [64]. Additional needs exist in determining suitable network topologies to optimally support high transmission capacity for powerful DCs, handle the increased computational capability of large data sets and run multiple requests in parallel as described in [65, 66] by both Facebook and Google, respectively. The selected network architecture must be flexible, scalable and modular to accommodate new service requirements with zero or minimum downtime. Optical interconnects at various scales can make use of different networks topologies since system parameters, design goals and requirements can differ significantly among providers. Furthermore, several digital signal processing techniques have been established and continue to be developed to alleviate impairments in coherent optical communications such as clock recovery (CR) for enhanced floor-free transmission at higher bit rates as well as different modulation schemes. Different efforts have been carried out to demonstrate the robustness of CR devices with high spectral purity against detrimental degradation encountered in optical transmission to include excess optical noise of optical amplifiers and residual

chromatic dispersion in optical fibers as reported in [67]. Innovative approaches leading to a major technology shift will also come from new developments in the field of advanced packaging. Tighter opto-electrical integration along with packaging will play a significant role in the overall performance of these devices and will likely change the landscape of SiPh as it can help solve some of the challenges associated with heterogeneous integration [11]. New packaging techniques can potentially alleviate the risk of short cavity reflections that can be detrimental to the laser's performance and limit floor-free transmissions at the desired level as demonstrated in Chapter IV and V of this manuscript.

Although hybrid SiPh integration and its use for optical links has already been proven as described in [33]; the implementation of next generation optical interconnects poses specific technological constraints, especially in relation to power dissipation, optimal reach and maximum channel data rate. The development of light sources on-chip using a wafer scale approach remains a critical challenge. The main difficulty still resides in designing the appropriate chip-level interconnects that satisfy the high requirements on bandwidth capacity, latency and energy efficiency in order to optimize the internal network architecture to support the new generation of DCs [68]. Therefore, different efforts continue to be carried out to further investigate the properties of III-V materials and Si combined for the development of feedback insensitive light sources on-chip for high-speed optical interconnects to achieve a cost effective solution compatible with legacy data center standards.

### 1.2.2 High Performance Computing

Another important application of SiPh is in the high performance computing (HPC) domain. This technology goes hand in hand with the existing and projected digital appetite. It is evident that computing performance must continue to improve in order to meet the growing proliferation of computing processing and communications capability required by DCs (massive parallel supercomputers infrastructure) to support increased capacity and distance as digital trends continue to evolve [61]. In an effort to forecast the rapid growth of

cloud-based IP and the degree of virtualization, Cisco reported in [69] that hyperscale DCs (large-scale public cloud DCs) will grow from 338 in number at the end of 2016 to 628 at the end of 2021. Hyperscale DCs are expected to quadruple and estimated to represent 53% of the installed data serves by 2020. The annual global cloud IP traffic is also expected to reach 19.5 Zettabytes (1.6 ZB per month) by the end of 2021, up from 6.0 ZB per year (499 EB per month) in 2016. That means that the global cloud IP traffic will more than triple over the next 5 years and expected to account for 95% of total DC traffic by 2021. In addition, DCs virtualization and cloud computing is also expected to increase exponentially. By 2021, 94% of workloads and compute instances will be processed by multi-cloud DCs; 6% will be processed by traditional DCs, therefore, a robust underlined compute capability and reliable infrastructure to ensure prompt response time is imperative. Furthermore, DC workloads and compute instances will more than double from 2016 to 2021; however, for cloud those will nearly triple over the same period [69]. A compute instance is defined as a virtual or physical set of computer resources, including storage, that are assigned to run a specific application or provide computing services for one to many users. Therefore, it is crucial for data providers to prepare for this pivotal and unavoidable fast-coming growth of intensive workloads requirements. Compute capacity must continue to scale at the component and at the system level in order to meet the high pace bandwidth growth in support of the essential network's infrastructure transformation while maintaining high level performance [61].

For computation hardware, the past three decades saw central processing units (CPUs) performance gains governed by Moore's Law and driven by reduction in semiconductor feature size and the use of multi-core architectures. However, the semiconductor form factor is at the edge of practical lithography capability and will be limited by physical principles. While multi-core architectures performance hinges on having high-bandwidth chip-scale communication networks. Bandwidth to access off-chip memory is also crucial to scalable high-performance architectures [70]. The need for bandwidth is driven

by the server and storage consolidation and inter-processor communication, as well as the increased bandwidth demands of multi-core and multi-threaded CPUs. Therefore, future supercomputers are expected to have tens of thousands of transceivers, each providing aggregate point-to-point interconnect bandwidths of greater than 100-Gbps [71]. State-of-the-art network typologies will then require sophisticated architectures for optimizing an increased number of processor-memory units, lower latency signaling between chips, and larger system bisection bandwidths for communication. Currently, the top HPC systems have bisection bandwidths between 1 to 10 Tbps and next generation systems are looking for 10-100x improvements in bandwidth [61]. This means that enhanced compute capacity is of paramount importance to accommodate the cloud estimated workloads and traffic demand to perform tens of trillions of computations per second [72] as we continue to scale and improve efficiency at the system level.

### **1.3 Overview of III-V/Silicon Hybrid Technology**

#### 1.3.1 Silicon Waveguides

Si waveguides form the basic building blocks of all SiPh circuits. Their fabrication starts with a SOI wafer, which is considered the most suitable platform for SiPh devices. The characterization results presented throughout the course of this thesis were obtained using devices provided by III-V lab. In this section, the process used to fabricate the devices under investigation is generally described.

Fig. 1.6 displays the Si waveguide: the Si is 500 nm thick and the SOI buried oxide (BOX) is approximately 2  $\mu\text{m}$  thick. The SOI is constructed by patterning three types of Si waveguides: 1) the laser rib, 2) the strip and 3) the passive rib waveguide. The rib width  $W_{Si}$  fabrication is conducted using a 193 nm deep-UV (DUV) high resolution lithography to precisely control its size. The slab width  $W_{slab}$  is usually larger compared to the mode size. Its value has very little impact on the mode properties; therefore, it is fabricated with a less precise 248 nm DUV lithography equipment. In order to achieve Si dry etching, a 180

nm hydrogen bromide (HBr) process is used [73]. After the patterning is completed, the waveguides are encapsulated in silicon dioxide ( $\text{SiO}_2$ ) then chemical-mechanical polishing (CMP) is performed to planarize the wafer surface and reduce the  $\text{SiO}_2$  thickness to 80 nm. The variation in refractive index between Si and  $\text{SiO}_2$  is important because it provides strong vertical confinement of light traveling in the Si overlay of the SOI [22].

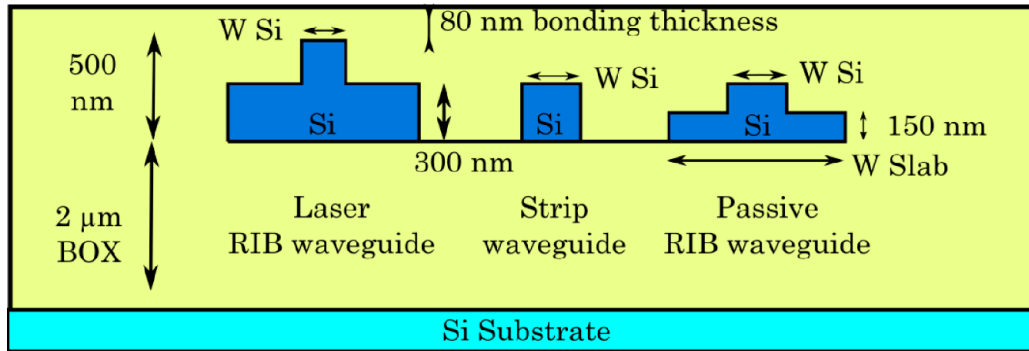


Figure 1.6: Silicon waveguides developed by III-V lab-Leti technology [74].

As described in [75], the waveguide single mode operation depends on the rib width  $W_{Si}$ . If  $W_{Si}$  is larger than a cut-off value  $W_{Si_c}$ , both transverse electric (TE) modes: the fundamental mode,  $\text{TE}^0$  and the first-order mode  $\text{TE}^1$  are guided in the structure. Fortunately, due to the accuracy of DUV lithography and the well-established Si etching processes, it is possible to fabricate Si based-waveguides with  $W_{Si} < W_{Si_c}$  to keep only one TE mode (i.e.,  $\text{TE}^0$ ). As referenced in [75] the rib and strip waveguides have losses around 1.5 dB/cm and 4 dB/cm, respectively. Losses are influenced by the sidewall roughness and mode leakage in the substrate as indicated in [76]. The following section describes the fabrication process of III-V materials on Si lasers devices by bonding a III-V wafer on top of a processed Si wafer.

### 1.3.2 Hybrid III-V/Si Semiconductor Lasers

III-V compounds have emerged as the materials of choice for lasers that emit in the 0.7-1.6  $\mu\text{m}$  wavelength range because heterogeneously integrated III-V materials have demonstrated

significant improvements in the development of electrically-pumped laser sources on Si [77]. This integration is achieved by means of die to wafer  $\text{SiO}_2/\text{SiO}_2$  direct bonding as described in [74]. The gain region is a forward bias  $pn$  junction. The devices studied herein use an active region with height AlInGaAs QWs that are 8 nm thick. They are sandwiched between two separate confinement heterostructures as well as an  $n$  and  $p$ -doped InP. Normally, III-V lasers are grown from an  $n$ -type substrate to a  $p$ -doped contact. Since the III-V wafer substrate needs to be removed, an inverse structure is then grown, that is, the  $p$  doped InP first followed by active region and then the  $n$ -doped Indium Phosphide (InP) as shown in fig. 1.7. The  $n$  side is then bonded to the SOI wafer and the substrate is removed as described in detail in [78].

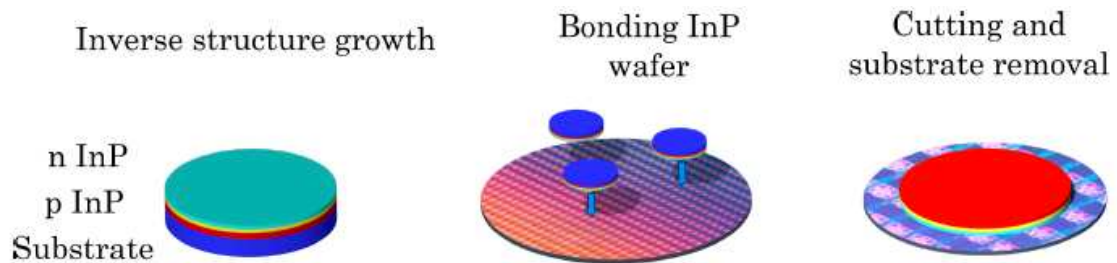


Figure 1.7: III-V on silicon epitaxy and bonding [74].

Different approaches for wafer fabrication and bonding techniques has been proposed. For instance, UCSB and Intel Lab first developed a III-V/SOI laser [79]. In their platform the Si and III-V wafers are oxidized before bonding. This technique results in a very thin spacer of 5 nm between III-V and Si. As illustrated in fig 1.8(a), the Si waveguide is not encapsulated: there are air trenches in each of its sides. Their III-V mesa is wide ( $\omega > 7 \mu\text{m}$ ). Proton implantation limits the current injection on a small surface to efficiently inject carriers into the gain region and prevents the coupling to III-V higher order mode (gain guided structure). The mode is also index-guided by the Si waveguide. Another innovative approach has been developed by Ghent University and IMEC as demonstrated in fig. 1.8(b). In this case, the Si waveguides are encapsulated in  $\text{SiO}_2$  and CMP is then

performed to reduce SiO<sub>2</sub> thickness down to 5 to 60 nm. Then, benzocyclobutene (DVS-BCB) is deposited by spin coating, which results in a spacer thickness lower than 110 nm. The III-V wafer is bonded by DVS-BCB as it sticks to both wafers. This bonding technique is more tolerant to III-V wafers defects as compared to the molecular bonding approach used on the devices investigated in throughout this thesis [80].

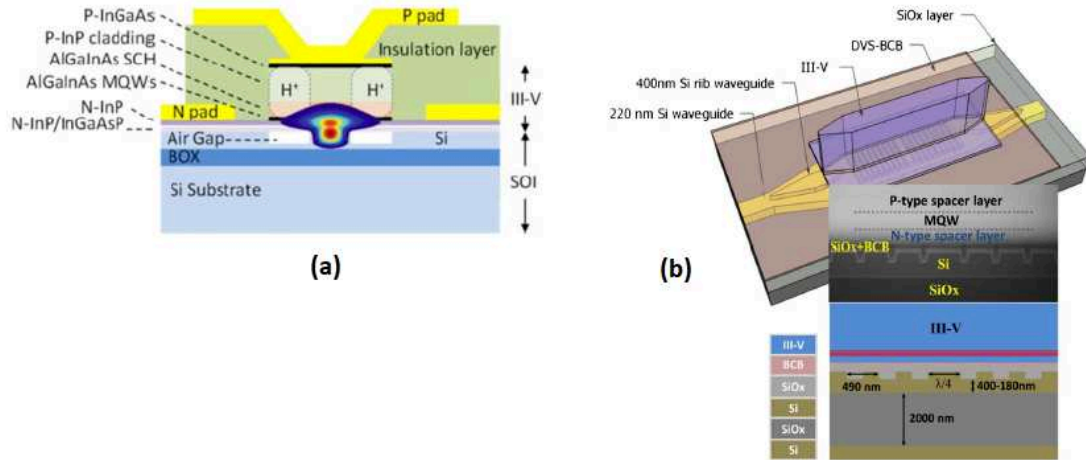


Figure 1.8: III-V/Si heterogeneous integration approaches: (a) UCSB/Intel with low bonding thickness and non-encapsulated Si waveguides [81] (b) IMEC platform uses BCB bonding [80].

The hybrid SiPh integration approach exploits the highly efficient light emission properties of some direct gap III-V semiconductor materials that can offer unique advantages as well as some shortcomings. The proposed novel designs have demonstrated that making use of existing microelectronics techniques for integration density while tailoring the selected approach based on the desired functionality can be extremely beneficial.

For instance the III-V process carried out by III-V Lab is performed on a 2, 3 or 4 inch wafer bonded on Si as depicted in fig. 1.9. First, contact lithography is conducted to define the different III-V active regions. In this step, both dry and humid etching processes are used. Secondly, the NiCr heaters are plated on top of an alumina layer to protect the optical mode from the highly absorbing metal. Thirdly, modulator electrodes as well as the heater and the laser buried contacts are made. In addition, the component is then encapsulated in

BCB. Last but not least, vias are made in BCB and a second metallization takes place.

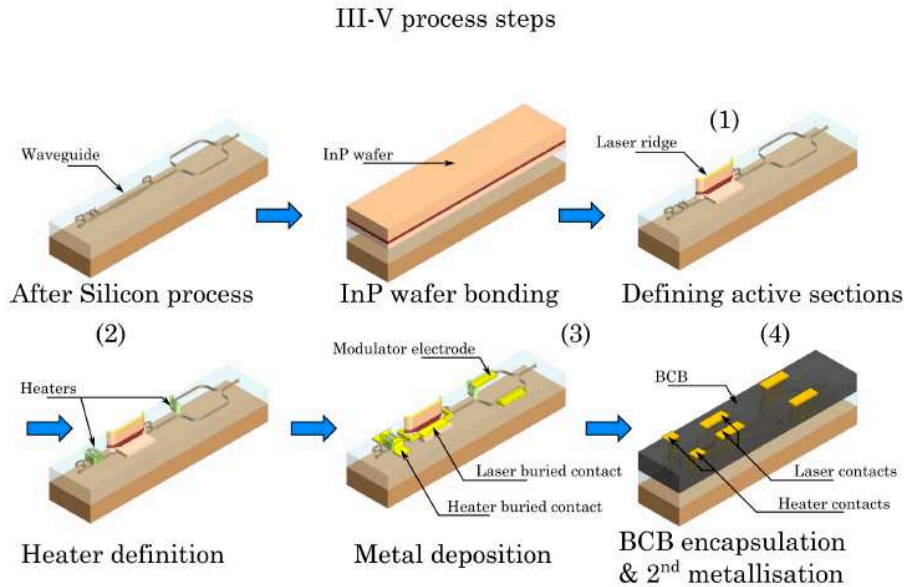


Figure 1.9: III-V/SOI laser process [75].

The main difficulty of III-V on Si processing is that initial etching methods were originally developed for III-V wafers with  $n$  doped substrates. As a consequence, those recipes have been tailored to accommodate the isolating substrate on SOI wafers. The cross section schematics and the scanned electron image (SEM) of such device is displayed in fig. 1.10(a) and fig. 1.10(b), respectively.

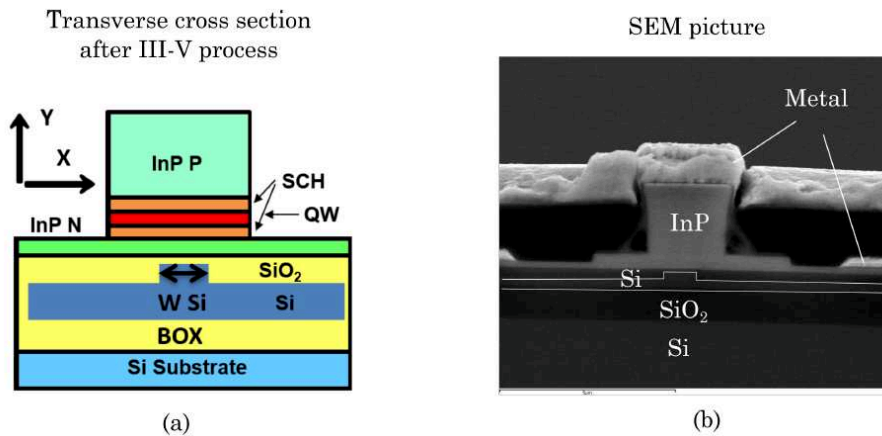


Figure 1.10: (a) Cross section of the III-V/SOI and (b) Scanned electron image of the structure [74].

## 1.4 Organization of the Thesis

The work presented in this manuscript aims at further investigating some of the strengths as well as the imposed restrictions and limitations of SiPh as it pertains to the light source for PIC applications, specifically novel hybrid III-V/Si SCLs. The structure of the thesis is as follows. First, in this chapter, an overview of SiPh is provided where technology applications and associated challenges are identified. In addition, the III-V/Si hybrid technology is generally introduced. Next, Chapter II summarizes the principles of SCLs to include basic operation parameters such as optical gain, radiative transition and linewidth enhancement factor among others. A description of several SCL structural variations available for potential on-chip integration is also provided. Chapter III dives into the definition of optical feedback and provides substantiating information on the potential effects parasitic reflections originating from multiple sources could have on the spectral characteristics of SCLs and overall performance. An analytical approach of non-linear dynamics is also discussed. The static and dynamic characteristics of different hybrid III-V/Si devices to include Fabry-Perot (FP) and tunable lasers (TUL) as well as the impact of optical feedback on their operation properties are experimentally demonstrated and highlighted in Chapter IV by comparing results obtained using different experimental set-ups configurations to understand the modal and temporal dynamics caused by optical feedback. In this section, we draw attention to the sensitivity of the output intensity to both amplitude and phase variations when these devices are subject to a combination of short and long cavity feedback conditions by discussing the findings from various characterization scenarios. Furthermore, Chapter IV examines the coherence collapse (CC) and the transition to chaotic state due to the non-linear dynamics effects. Performance results of a hybrid III-V/Si distributed feedback (DFB) SCL directly modulated at 10-Gbps is also demonstrated. Chapter V extends the modulation efforts to examine the dynamic properties of a hybrid III-V/Si DFB with a high quality factor externally modulated and explores its thermal sensitivity. The perfor-

mance results unveil its ability to successfully achieve a 10-Gbps floor-free transmission. The impact of optical feedback and thermal influence on the bit error rate (BER) and power penalty degradation is also shown. Finally, a general summary of the work is furnished in Chapter VI along with an outlook of this technology for future achievements.

## REFERENCES

- [1] D. Thomson, A. Zilkie, J. E. Bowers, T. Komljenovic, G. T. Reed, L. Vivien, D. Marris-Morini, E. Cassan, L. Viro, J.-M. Fédéli, J.-M. Hartmann, J. H. Schmid, D.-X. Xu, F. Boeuf, P. O'Brien, G. Z. Mashanovich, and M Nedeljkovic, "Roadmap on silicon photonics," *Journal of Optics*, vol. 18, no. 7, p. 073 003, 2016.
- [2] G.-H. Duan, C. Jany, A. L. Liepvre, A. Accard, M. Lamponi, D. Make, P. Kaspar, G. Levaufre, N. Girard, F. Lelarge, J.-M. Fedeli, A. Descos, B. B. Bakir, S. Messaoudene, D. Bordel, S. Menezo, G. de Valicourt, S. Keyvaninia, G. Roelkens, D. V. Thourhout, D. J. Thomson, F. Y. Gardes, and G. T. Reed, "Hybrid III–V on silicon lasers for photonic integrated circuits on silicon," *IEEE Journal of Selected Topics in Quantum Electronics*, vol. 20, no. 4, pp. 158–170, 2014.
- [3] L. Vivien, D. Marris-Morini, L. Viro, D. Perez-Galacho, G. Rasigade, J.-M. Hartmann, E. Cassan, P. Crozat, S. Olivier, C. Baudot, F. Boeuf, and J.-M. Fedeli, "High speed silicon-based optoelectronic devices on 300mm platform," in *2014 16th International Conference on Transparent Optical Networks (ICTON)*, IEEE, 2014.
- [4] *Handbook of silicon photonics (series in optics and optoelectronics)*. CRC Press, 2013, ISBN: 9781439836101.
- [5] G. Roelkens, U. Dave, A. Gassenq, N. Hattasan, C. Hu, B. Kuyken, F. Leo, A. Malik, M. Muneeb, E. Ryckeboer, S. Uvin, Z. Hens, R. Baets, Y. Shimura, F. Gencarelli, B. Vincent, R. Loo, J. V. Campenhout, L. Cerutti, J.-B. Rodriguez, E. Tournié, X. Chen, M. Nedeljkovic, G. Mashanovich, L. Shen, N. Healy, A. C. Peacock, X. Liu, R. Osgood, and W. Green, "Silicon-based heterogeneous photonic integrated circuits for the mid-infrared," *Optical Materials Express*, vol. 3, no. 9, p. 1523, 2013.
- [6] A. Rickman, "The commercialization of silicon photonics," *Nature Photonics*, vol. 8, no. 8, pp. 579–582, 2014.
- [7] P. Chaisakul, D. Marris-Morini, J. Frigerio, D. Chrastina, M.-S. Rouified, S. Cecchi, P. Crozat, G. Isella, and L. Vivien, "Integrated germanium optical interconnects on silicon substrates," *Nature Photonics*, vol. 8, no. 6, pp. 482–488, 2014.
- [8] P. Dong, Y.-K. Chen, G.-H. Duan, and D. T. Neilson, "Silicon photonic devices and integrated circuits," *Nanophotonics*, vol. 3, no. 4-5, 2014.
- [9] P. Burke, C. Du, D. Herr, J. Jensen, P. Lugli, D. Radack, M. Stroschio, V. Swaminathan, E. Towe, and D. Woodlard, "Device concepts, architectural strategies, and in-

terfacing methodologies for nanoscale sensor systems,” *IEEE Transactions on Nanotechnology*, vol. 9, no. 5, pp. 523–526, 2010.

- [10] A. Björilin, *Silicon photonics: High speed optical connectivity for 5G*, Sep. 2018.
- [11] I. D. Sousa, L.-M. Achard, and D. Patterson, *The future of packaging with silicon photonics*, Chip Scale Review, Jan. 2017.
- [12] Cisco, “Cisco visual networking index: Forecast and trends, 2017–2022,” Feb. 2019.
- [13] D. Newman, *Top 10 trends for digital transformation in 2018*, Sep. 2017.
- [14] C. Sun, M. T. Wade, Y. Lee, J. S. Orcutt, L. Alloatti, M. S. Georgas, A. S. Waterman, J. M. Shainline, R. R. Avizienis, S. Lin, B. R. Moss, R. Kumar, F. Pavanello, A. H. Atabaki, H. M. Cook, A. J. Ou, J. C. Leu, Y.-H. Chen, K. Asanović, R. J. Ram, M. A. Popović, and V. M. Stojanović, “Single-chip microprocessor that communicates directly using light,” *Nature*, vol. 528, no. 7583, pp. 534–538, 2015.
- [15] W. Bogaerts, M. Fiers, and P. Dumon, “Design challenges in silicon photonics,” *IEEE Journal of Selected Topics in Quantum Electronics*, vol. 20, no. 4, pp. 1–8, 2014.
- [16] M. Asghari and A. V. Krishnamoorthy, “Energy-efficient communication,” *Nature Photonics*, vol. 5, no. 5, pp. 268–270, 2011.
- [17] E. Mounier and T. Buisson, *Data center O/Is could pave the way for the photonic-in-package era*, Chip Scale Review, Jan. 2017.
- [18] A. Neri, *The edge-centric, cloud-enabled, data-driven enterprise of the future*, Hewlett Packard, Nov. 2018.
- [19] A. T. Friberg and R. Dändliker, Eds., *Advances in information optics and photonics*. SPIE, 2008.
- [20] H. Park, A. W. Fang, S. Kodama, and J. E. Bowers, “Hybrid silicon evanescent laser fabricated with a silicon waveguide and III-v offset quantum wells,” *Optics Express*, vol. 13, no. 23, p. 9460, 2005.
- [21] S. Serna, X. L. Roux, W. Zhang, C. Alonso-Ramos, D. Marris-Morini, L. Vivien, and E. Cassan, “Extrinsic losses in silicon slot photonic crystal waveguides: Influence of the fabrication process,” in *Asia Communications and Photonics Conference*, OSA, 2017.

- [22] A. Knights and J. Doylend, “Silicon photonics—recent advances in device development,” in *Advances in Information Optics and Photonics*, SPIE, 2008, pp. 633–656.
- [23] J. E. Bowers, “Evolution of photonic integrated circuits,” in *2017 75th Annual Device Research Conference (DRC)*, IEEE, 2017.
- [24] M. J. R. Heck, M. L. Davenport, and J. E. Bowers, “Progress in hybrid-silicon photonic integrated circuit technology,” *SPIE Newsroom*, 2013.
- [25] R. E. Camacho-Aguilera, Y. Cai, N. Patel, J. T. Bessette, M. Romagnoli, L. C. Kimerling, and J. Michel, “An electrically pumped germanium laser,” *Optics Express*, vol. 20, no. 10, p. 11 316, 2012.
- [26] A. Lee, Q. Jiang, M. Tang, A. Seeds, and H. Liu, “Continuous-wave InAs/GaAs quantum-dot laser diodes monolithically grown on si substrate with low threshold current densities,” *Optics Express*, vol. 20, no. 20, p. 22 181, 2012.
- [27] A. Y. Liu, C. Zhang, J. Norman, A. Snyder, D. Lubyshev, J. M. Fastenau, A. W. K. Liu, A. C. Gossard, and J. E. Bowers, “High performance continuous wave 1.3  $\mu\text{m}$  InAs quantum dot lasers on silicon,” *Applied Physics Letters*, vol. 104, no. 4, p. 041 104, 2014.
- [28] H. Shimizu, “Semiconductor optical isolators for integrated optics,” in *Spintronics VI*, H.-J. Drouhin, J.-E. Wegrowe, and M. Razeghi, Eds., SPIE, 2013.
- [29] G. Roelkens, J. V. Campenhout, J. Brouckaert, D. V. Thourhout, R. Baets, P. R. Romeo, P. Regreny, A. Kazmierczak, C. Seassal, X. Letartre, G. Hollinger, J. Fedeli, L. D. Cioccio, and C. Lagahe-Blanchard, “III-V/si photonics by die-to-wafer bonding,” *Materials Today*, vol. 10, no. 7-8, pp. 36–43, 2007.
- [30] H. Park, M. N. Sysak, H.-W. Chen, A. W. Fang, D. Liang, L. Liao, B. R. Koch, J. Bovington, Y. Tang, K. Wong, M. Jacob-Mitos, R. Jones, and J. E. Bowers, “Device and integration technology for silicon photonic transmitters,” *IEEE Journal of Selected Topics in Quantum Electronics*, vol. 17, no. 3, pp. 671–688, 2011.
- [31] J. C. Hulme, J. K. Doylend, and J. E. Bowers, “Widely tunable vernier ring laser on hybrid silicon,” *Optics Express*, vol. 21, no. 17, p. 19 718, 2013.
- [32] L. Chrostowski and M. Hochberg, *Silicon photonics design*. Cambridge University Press, 2015.
- [33] M. J. R. Heck, H.-W. Chen, A. W. Fang, B. R. Koch, D. Liang, H. Park, M. N. Sysak, and J. E. Bowers, “Hybrid silicon photonics for optical interconnects,” *IEEE Journal of Selected Topics in Quantum Electronics*, vol. 17, no. 2, pp. 333–346, 2011.

- [34] J. E. Bowers and A. Y. Liu, “A comparison of four approaches to photonic integration,” in *Optical Fiber Communication Conference*, OSA, 2017.
- [35] Y. Wan, Q. Li, A. Y. Liu, Y. Geng, J. Norman, W. W. Chow, A. C. Gossard, J. E. Bowers, E. L. Hu, and K. M. Lau, “Quantum dot lasers grown on (001) si substrate for integration with amorphous si waveguides,” in *Optical Fiber Communication Conference*, OSA, 2017.
- [36] M. Harfouche, “The coherence collapse regime of high-coherence Si/III-V lasers and the use of swept frequency semiconductor lasers for full field 3d imaging,” PhD thesis, 2018.
- [37] L. Viroth, P. Crozat, J.-M. Fédéli, J.-M. Hartmann, D. Marris-Morini, E. Cassan, F. Boeuf, and L. Vivien, “Germanium avalanche receiver for low power interconnects,” *Nature Communications*, vol. 5, no. 1, 2014.
- [38] G. T. Reed, G. Mashanovich, F. Y. Gardes, and D. J. Thomson, “Silicon optical modulators,” *Nature Photonics*, vol. 4, no. 8, pp. 518–526, 2010.
- [39] D. Liang and J. E. Bowers, “Recent progress in lasers on silicon,” *Nature Photonics*, vol. 4, no. 8, pp. 511–517, 2010.
- [40] C. Wang, X.-L. Zhong, and Z.-Y. Li, “Linear and passive silicon optical isolator,” *Scientific Reports*, vol. 2, no. 1, 2012.
- [41] W. V. Parys, M. Vanwolleghem, D. V. Thourhout, R. Baets, F. Lelarge, B. Thedrez, and L. Lagae, “Study of a magneto-optic contact for an amplifying waveguide optical isolator,” *IEEE Photonics Technology Letters*, vol. 19, no. 9, pp. 659–661, 2007.
- [42] Y. Cai, A. Pilipetskii, and M. Nissov, “On optimal decision thresholds for soft-decision error correction decoding in fiberoptic communication systems,” in *Optical Fiber Communication Conference*, Optical Society of America, 2004, WM3.
- [43] M. OMahony, “Semiconductor laser optical amplifiers for use in future fiber systems,” *Journal of Lightwave Technology*, vol. 6, no. 4, pp. 531–544, 1988.
- [44] L. A. Coldren, S. W. Corzine, and M. L. Mašanović, *Diode lasers and photonic integrated circuits*. John Wiley & Sons, Inc., 2012.
- [45] A. Sharaiha, “Simultaneous in-line photodetection using semiconductor optical amplifier in presence of bi-directional transmission,” in *Conference Proceedings. LEOS98. 11th Annual Meeting. IEEE Lasers and Electro-Optics Society 1998 Annual Meeting (Cat. No.98CH36243)*, IEEE.

- [46] A. Sharaiha and M. Guegan, “Equivalent circuit model for multi-electrode semiconductor optical amplifiers and analysis of inline photodetection in bidirectional transmissions,” *Journal of Lightwave Technology*, vol. 18, no. 5, pp. 700–707, 2000.
- [47] K. Yamada, T. Tsuchizawa, H. Nishi, R. Kou, T. Hiraki, K. Takeda, H. Fukuda, Y. Ishikawa, K. Wada, and T. Yamamoto, “High-performance silicon photonics technology for telecommunications applications,” *Science and Technology of Advanced Materials*, vol. 15, no. 2, p. 024 603, 2014.
- [48] D. Miller, “Device requirements for optical interconnects to CMOS silicon chips,” in *Integrated Photonics Research, Silicon and Nanophotonics and Photonics in Switching*, OSA, 2010.
- [49] M. M. Research, *Global silicon photonics market – global industry analysis and forecast (2017-2026) by product (switch, transceiver, and others), component (modulator, laser, photodetector), application, and geography*.
- [50] Q. Cheng, M. Bahadori, M. Glick, S. Rumley, and K. Bergman, “Recent advances in optical technologies for data centers: A review,” *Optica*, vol. 5, no. 11, p. 1354, 2018.
- [51] C. Lam, “Google optical network,” in *National Fiber Optic Engineers Conference*, OSA, 2010.
- [52] M. J. R. Heck, “Grating coupler enabled optical isolators and circulators for photonic integrated circuits,” *IEEE Journal of Selected Topics in Quantum Electronics*, vol. 21, no. 4, pp. 361–369, 2015.
- [53] M. Asghari, “Silicon photonics: A low cost integration platform for datacom and telecom applications,” in *Optical Fiber Communication Conference/National Fiber Optic Engineers Conference*, Optical Society of America, 2008.
- [54] Y. Vlasov, “Silicon CMOS-integrated nano-photonics for computer and data communications beyond 100g,” *IEEE Communications Magazine*, vol. 50, no. 2, s67–s72, 2012.
- [55] D. Perez-Galacho, L. Bramerie, C. Baudot, M. Chaibi, S. Messaoudene, N. Vulliet, L. Vivien, F. Boeuf, C. Peucheret, and D. Marris-Morini, “Silicon modulators for the generation of advanced modulation formats,” in *2018 20th International Conference on Transparent Optical Networks (ICTON)*, IEEE, 2018.
- [56] Ciena, *What is dci?* <https://www.ciena.com/insights/what-is/What-is-DCI.html>.
- [57] *Optical interconnects for data centers*. Elsevier, 2017.

- [58] P. Absil, “Silicon photonics integration,” *SPIE Professional*, 2014.
- [59] R. F. Aguinaldo, “Silicon photonics with applications to data center networks,” PhD thesis, University of California San Diego, 2014.
- [60] A. V. Krishnamoorthy, K. W. Goossen, W. Jan, X. Zheng, R. Ho, G. Li, R. Rozier, F. Liu, D. Patil, J. Lexau, H. Schwetman, D. Feng, M. Asghari, T. Pinguet, and J. E. Cunningham, “Progress in low-power switched optical interconnects,” *IEEE Journal of Selected Topics in Quantum Electronics*, vol. 17, no. 2, pp. 357–376, 2011.
- [61] A. Krishnamoorthy, “The intimate integration of photonics and electronics,” in *Advances in Information Optics and Photonics*, SPIE, pp. 581–598.
- [62] A. Boletti, D. Giacomuzzi, G. Parladori, P. Boffi, M. Ferrario, and M. Martinelli, “Performance comparison between electrical copper-based and optical fiber-based backplanes,” *Optics Express*, vol. 21, no. 16, p. 19 202, 2013.
- [63] S. Mishra, N. Chaudhary, and K. Singh, “Overview of optical interconnect technology,” *International Journal of Scientific and Engineering Research*, vol. Volume 3, Apr. 2012.
- [64] W. S. Ring, *Silicon photonics: Challenges and future*, Optoelectronics Industry Development Association Forum Report, 2007.
- [65] N. Farrington and A. Andreyev, “Facebooks data center network architecture,” in *2013 Optical Interconnects Conference*, IEEE, 2013.
- [66] X. Z. X. Zhou, H. L. H. Liu, R. Urata, and R. Urata, “Datacenter optics: Requirements, technologies, and trends (invited paper),” *Chinese Optics Letters*, vol. 15, no. 5, pp. 120 008–120 011, 2017.
- [67] V. Roncin, S. Lobo, L. Bramerie, P. Rochard, A. Shen, F. V. Dijk, G.-H. Duan, and J.-C. Simon, “Demonstration of chromatic dispersion and optical noise insensitivity of a quantum-dash based fabry-perot laser in all-optical clock recovery at 40 gbit/s,” in *33rd European Conference and Exhibition on Optical Communication - ECOC 2007*, IEE, 2007.
- [68] S. Aleksic, “The future of optical interconnects for data centers: A review of technology trends,” in *2017 14th International Conference on Telecommunications (ConTEL)*, IEEE, 2017.
- [69] Cisco, *Cisco global cloud index: Forecast and methodology, 2016 –2021*, Nov. 2018.
- [70] X. L. Zhu, “Systems engineering for silicon photonic devices,” PhD thesis, Columbia University, 2016.

- [71] P. Pepeljugoski, F. Doany, D. Kuchta, L. Schares, C. Schow, M. Ritter, and J. Kash, "Data center and high performance computing interconnects for 100 gb/s and beyond," in *OFC/NFOEC 2007 - 2007 Conference on Optical Fiber Communication and the National Fiber Optic Engineers Conference*, IEEE, 2007.
- [72] A. Sabban, *Novel wearable antennas for communication and medical systems*. CRC Press, 2017, ISBN: 978-1-138-04790-7.
- [73] M. Lamponi, "Hybrid III-V on silicon lasers for telecommunication applications," PhD thesis, Université Paris Sud - Paris XI, Mar. 2012.
- [74] A. Gallet, "Hybrid III-V/Si lasers for optical communications," PhD thesis, Université Paris-Saclay, 2018.
- [75] X. Pommarede, "Hybrid III-V/Si photonic integrated circuits for optical communication applications," PhD thesis, Université Paris-Saclay, May 2017.
- [76] F. Grillot, L. Vivien, S. Laval, and E. Cassan, "Propagation loss in single-mode ultrasmall square silicon-on-insulator optical waveguides," *J. Lightwave Technol.*, vol. 24, no. 2, p. 891, 2006.
- [77] L. Grenouillet, T. Dupont, P. Philippe, J. Harduin, N. Olivier, D. Bordel, E. Augendre, K. Gilbert, P. Grosse, A. Chelnokov, and J. M. Fedeli, "Hybrid integration for silicon photonics applications," *Optical and Quantum Electronics*, vol. 44, no. 12-13, pp. 527–534, 2012.
- [78] D. Bordel, M. Argoud, E. Augendre, J. Harduin, P. Philippe, N. Olivier, S. Mes-saoude, K. Gilbert, P. Grosse, B. B. Bakir, and J.-M. Fedeli, "Direct and polymer bonding of III-V to processed silicon-on-insulator for hybrid silicon evanescent lasers fabrication," ECS, 2010.
- [79] A. W. Fang, H. Park, O. Cohen, R. Jones, M. J. Paniccia, and J. E. Bowers, "Electrically pumped hybrid AlGaInAs-silicon evanescent laser," *Optics Express*, vol. 14, no. 20, p. 9203, 2006.
- [80] S. Keyvaninia, S. Verstuyft, L. V. Landschoot, F. Lelarge, G.-H. Duan, S. Mes-saoudene, J. M. Fedeli, T. D. Vries, B. Smalbrugge, E. J. Geluk, J. Bolk, M. Smit, G. Morthier, D. V. Thourhout, and G. Roelkens, "Heterogeneously integrated III-v/silicon distributed feedback lasers," *Optics Letters*, vol. 38, no. 24, p. 5434, 2013.
- [81] M. J. R. Heck, J. F. Bauters, M. L. Davenport, J. K. Doylend, S. Jain, G. Kurczveil, S. Srinivasan, Y. Tang, and J. E. Bowers, "Hybrid silicon photonic integrated circuit technology," *IEEE Journal of Selected Topics in Quantum Electronics*, vol. 19, no. 4, pp. 6 100 117–6 100 117, 2013.

## CHAPTER 2

### PRINCIPLES OF SEMICONDUCTOR LASERS

Semiconductor devices are key elements for optical communication systems and are quickly penetrating other markets due to their enhanced coherence and potential to meet the required size, weight and power vital for modern data centers. In addition, SCLs have successfully demonstrated a suitable wavelength range and high reliability necessary to support increased bandwidth requirements and efficiently move large sets of data at higher speed rates. SCLs have also found use in many other potential applications to include long distance transmission, high-speed optical recording, single and multi-mode database transmission, free-space communications and high-speed printing among others [1].

The first laser, based on the ruby rod and emitting at  $\lambda = 694 \text{ nm}$ , was demonstrated by Maiman in 1960 at Hughes Research laboratories in California [2]. The burgeon of optoelectronics started in 1962 when gallium arsenide (GaAs) and gallium arsenide phosphide (GaAsP) SCLs were demonstrated by Hall, Nathan, Rediker, and Holonyak [3, 4, 5, 6].

The development of SCLs slowly transitioned from a pulse-operated simple *pn* homojunction to a continuously operated (300K) double heterostructure (DH) in 1970 [7, 8], which led to the development of light sources in fiber optics communications. Rapid improvements and enhanced reliability in SCLs, together with the introduction of low-loss optical fibers, have undoubtedly opened up the door for optical communications [9] as anticipated in 1966 by Kao and Hockham [10], indicating that optical fibers can be made pure enough to carry signals for very long distances. Semiconductor heterostructures have played a significant role in the progress made in several electronic, photonic and opto-electronic devices over the last couple of decades due to their abrupt change in the energy band structure at the heterointerface. This may lead to discontinuities in the conduction and valence band edges that can be used to control the flow and distribution of electrons and holes in device

structures while significantly altering the performance of the device [11].

In this chapter, the most related fundamentals principles of SCLs are outlined, followed by a short description of different laser configurations to include FP cavities, variations of tunable lasers (TULs) and hybrid III-V/Si technologies. In addition, the rate equations of LDs are reviewed to better understand the static and dynamic characteristics of the devices under investigation. Last but not least, the optical properties of SCLs and significant aspects of different structural designs are also discussed.

## 2.1 Basic Operation

### 2.1.1 Electronic Transitions in Semiconductors

The principle of SCLs lies in the interaction between light and semiconductor materials. The quantum electronic concept common to all lasers can be found in the  $pn$  junction of a semiconductor device, which is fabricated into an optical waveguide geometry that provides lateral opto-electronic confinement with certain mechanisms providing optical feedback for the generated optical wave such as front-end facets or grating [12]. The operation of a SCL relies on the interband recombination of carriers and the subsequent release of photons. By applying a forward bias into the center of the  $pn$  junction using an external voltage, a diffusion and drift of electrons and holes across the junction takes place, which pumps the carriers promoting population in the conduction band [13].

In a narrow depletion region, electron-hole pairs (EHP) can recombine both radiatively or non-radiatively. Electrons and holes can also absorb the radiation. When the current through the junction exceeds the critical value, population inversion is then achieved due to the rate of photon emission caused by the electron-hole recombination exceeding the rate of absorption associated with the electron-hole generation. The electronic radiative transitions that take place between the conduction and valence bands in a SCL play a key role similar to the one between the pairs of states in a simple two-level laser system following convention [14]. Fig. 2.1 provides a schematic energy-level diagram for two states  $|1\rangle$

and  $|2\rangle$  illustrating the three types of electronic recombination/generation (photon emission/absorption). In this figure,  $P(E)$  is the spectral density of electromagnetic modes measured in units of number of photons per unit volume per unit energy interval and  $f_1(f_2)$  is the ensemble average Fermi–Dirac occupation factor for particles in state  $|1\rangle$  ( $|2\rangle$ ). It is assumed that the system is maintained at absolute temperature  $T$  [15].

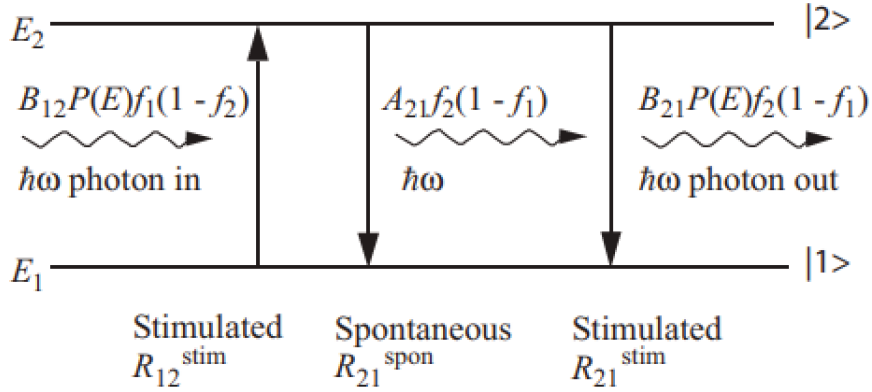


Figure 2.1: Schematic energy-level diagram: stimulated absorption, spontaneous emission, stimulated emission) [15].

Fig. 2.1(left) represents the energy of the photon transferred to an electron, while elevating it from some state 1 in the valence band to some state 2 in the conduction band. This process of stimulated absorption generates new carriers and is also responsible for the disappearance of photons (photon absorption). Fig. 2.1(middle) represents the case of an electron in the conduction band recombining spontaneously with a hole in the valence band to generate a photon. This process demonstrates that the field that stimulates the electron to emit a photon is not a real field, but a vacuum-field, which results in relatively incoherent emission because the emission time and direction is random and the photons will not contribute to a coherent radiation field (photon emission). In fig. 2.1(right), the incoming photon stimulates the electron to liberate energy in the form of a new photon, lowering it from state 2 in the conduction band to state 1 in the valence band, thus contributing to the coherent radiation field (coherent photon emission). Stimulated emission provides a recombination path for carriers and more importantly the source of new photons.

In this case, both the frequency and the phase of the emitted photon are identical to those of the incoming photon. Photons generated by stimulated emission then results in a narrow spectral linewidth. In addition, non-radiative recombination can also take place where a conduction band electron can recombine with a valence band hole without generating any useful photons [16]. Non-radiative mechanisms include [17, 16]: Recombination at defective surfaces and interfaces in the active region of the device and Auger recombination in which the electron-hole recombination energy is given to another electron or hole in the form of kinetic energy. In such processes, a conduction band electron recombines with a valence band hole while generating no useful photons, but phonons or lattice vibration. In the context of the SCL, crystal imperfections in the final wafer are inevitable but should be minimized because they represent the loss of electrons which do not contribute to the gain and significantly influence the efficiency of the carrier recombination. For instance, it is known that the direct growth of III-V on Si introduces a high-density of TDs [18] that lead to non-radiative recombination and reduced carrier density due to lattice, polarity, and incompatible thermal expansion coefficient mismatch between Si and the III-V, which can limit device performance and reliability [19].

However, there are several distinct features in a SCL active medium. For instance, the optical transitions in SCL for Si take place between a continuous band of states within the valence and conduction bands. The interaction between the different excited states in the band of a SCL is considerably greater than the interaction between the excited states of the different atoms in the two-level system. Therefore, the collision process in the electron and hole subsystems occurs much faster and the intraband relaxation time can be much shorter compared to that of the radiation (interband) process. The intraband process then plays a crucial role in the line broadening of a SCL. In addition, the higher the concentration of electronic states in the bands, the higher the potential for an enhanced optical gain. Finally, in a SCL, the EHPs can be transported through the material by conduction or diffusion leading to a spatial variation of the optical mode through the stimulated emission.

The band structure diagram of a typical III-V (i.e., GaAs, InP, and InGaAs) semiconductor (known as the  $E - k$  plot) is illustrated in fig. 2.2. The simplest model of a direct band-gap semiconductor typically includes a heavy-hole (HH) valence band with effective hole mass and conduction band  $e$  with effective electron mass. Fig 2.2 depicts schematically the spontaneous emission of a photon of energy  $\hbar\omega$  accompanied by an electronic transition of a state characterized by wave vector  $\mathbf{k}$  and energy  $E_K$  in the conduction band to wave vector state  $\mathbf{k}$  energy  $E_k - \hbar\omega$  in the valence band by emitting a photon energy  $\hbar\omega$ . Because the initial and final electronic states have the same value of  $\mathbf{k}$ , it is assumed that negligible momentum is carried off by the photon.

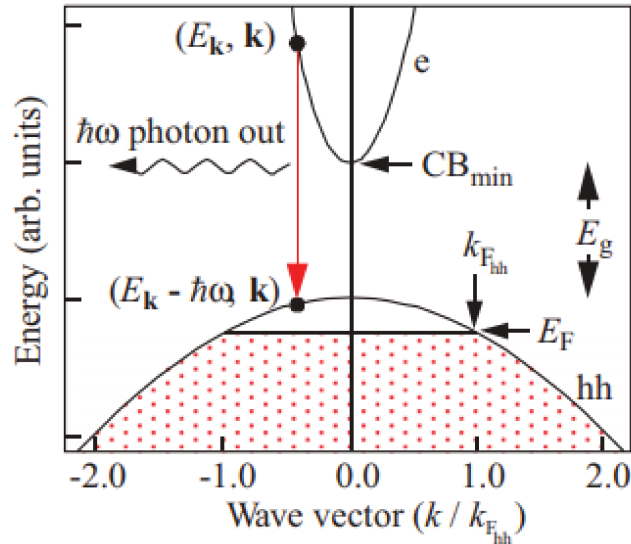


Figure 2.2: Electron energy vs  $k$  vector: Band structure of a direct band-gap III-V semiconductor showing valence heavy-hole (hh) band, conduction band  $e$ , minimum conduction band energy  $\mathbf{CB}_{\min}$ , and band-gap energy  $E_g$ . The semiconductor is doped p-type, and at low temperature the Fermi energy is  $E_F$  and the Fermi wave vector is  $k_{F_{hh}}$ . Electrons in the conduction band can make a transition from a state characterized by wave vector  $\mathbf{k}$  and energy  $E_k$  in the conduction band to wave vector state  $\mathbf{k}$  energy  $E_K - \hbar\omega$  in the valence band by emitting a photon of energy  $\hbar\omega$  [15].

In such a semiconductor the energy minimum of the conduction band lines up vertically in the wave vector ( $k$ -space) axis with the maximum energy of the valence band [15]; that is, they share the same crystal momentum. However, an indirect bandgap material is not naturally capable of accomplishing efficient radiative recombination.

For LDs, the transition from the conduction to the valence band should be radiative and must yield a photon energy:

$$\hbar\omega = E_c - E_v = E_g \quad (2.1)$$

where  $\hbar$  is the Planck's constant and  $\omega$  the angular frequency defined as  $2\pi\nu$ , where  $\nu = c/\lambda$  ( $c$  = speed of light and  $\lambda$  = wavelength of light).  $E_v$  and  $E_c$  are the electron energy in the valence and conduction bands respectively. As stated by the rules of quantum mechanics, it can be shown that each process must conserve both the energy and the wavevector  $k$ . The  $k$ -conservation rule immediately implies a requirement for direct band-gap semiconductors for the radiative recombination to be significant. The condition for lasing in a SCL is given by

$$E_g < \hbar\omega < F_c - F_v \quad (2.2)$$

where  $F_c$  and  $F_v$  represent the separation of the quasi-Fermi levels for electrons and holes respectively. Condition (2.2) is necessary, but not enough for lasing to occur in a SCL. Therefore, in order to achieve lasing, all conditions must be met for the stimulated emission rate to be sufficiently large to compensate the loss mechanisms. The optical gain is directly related to the rate of stimulated emission. The process of stimulated emission provides optical gain to an incident wave by generating a coherent wave (i.e., same direction and phase). Thus, the optical radiation propagating through the medium will be amplified as long as the stimulated emission process overwhelms the absorption in the cavity which requires a high density of electrons in the conduction band resulting in coherent light emission. However, under thermal equilibrium, more electrons naturally exist in the valence band resulting in the absorption process surpassing the stimulated emission. In this case, the gain is insufficient to compensate the cavity losses. Consequently, the material has to be driven into a higher non-equilibrium state to invert the carrier population by energy

injection so that incident radiation can be amplified rather than absorbed. For SCLs, population inversion is achieved by injecting current into a *pn* junction-based structure [12]. The main factors influencing the gain spectrum are the density of state functions as well as the transition and occupation probabilities.

### 2.1.2 The Rate Equations

The rate equations are of paramount importance to investigate the static and dynamic characteristics of SCLs as they model the electrical and optical performance of these devices. The differential equations relate to the density of photons and charge carriers in the device to the injection current as well as to the device and material parameters to include optical gain, photon lifetime and carrier lifetime. There is strong evidence substantiated by numerous publications that the rate equations can also capture the essential physics of SCLs subject to external optical feedback [20]. Therefore, these equations are necessary to properly understand the feedback parameters that will be discussed throughout the course of this thesis. The rate equations that follow are expressed in terms of carrier and photon generation.

#### *Carrier Generation*

The rate equation for the carrier density  $N$  can be defined as

$$\frac{dN}{dt} = G_{gen} - R_{rec} \quad (2.3)$$

where  $G_{gen}$  is the rate of injected carriers and  $R_{rec}$  is the rate of recombining carriers per unit volume in the active regions. Because there are  $\eta_i I/q$  electrons per second being injected into the active region then,

$$G_{gen} = \frac{\eta_i I}{qV} \quad (2.4)$$

where  $I$  is the bias current,  $q$  the electron charge,  $V$  the volume of the active region and  $\eta_i$  is the injection efficiency representing the fraction of terminal current that generates carriers in the active region. The rate of recombining carriers can be expressed as

$$R_{rec} = \frac{N}{\tau_c} + R_{st} \quad (2.5)$$

where  $\tau_c$  is the carrier lifetime and  $R_{st}$  is the net stimulated recombination defined by Equation (2.8), which is directly proportional to the optical gain  $G(N)$  defined by Equation (2.12). Thus, the carrier rate Equation (2.3) may also be expressed in terms of gain such as

$$\frac{dN}{dt} = \frac{\eta_i I}{qV} - \frac{N}{\tau_c} - G(N)S \quad (2.6)$$

The last two terms of this equation correspond to the carrier decay and photon generation, respectively. In the absence of a large photon density, such as in the laser well below threshold,  $R_{st}$  can be neglected.

### *Photon Generation*

The rate equation for the photon density  $S$ , which includes the photon generation and loss terms can be defined as

$$\frac{dS}{dt} = \Gamma R_{st} + \Gamma \beta_{sp} R_{sp} - \frac{S}{\tau_p} \quad (2.7)$$

where  $\Gamma$  is the confinement factor,  $\beta_{sp}$  is the spontaneous emission factor, defined as the percentage of the total spontaneous emission coupled into the lasing mode and  $\tau_p$  is the photon lifetime.  $R_{st}$  represents the photon-stimulated net electron-hole recombination that generates more photons. Thus, photon generation term above threshold  $R_{st}$  can then be defined as:

$$R_{st} = \nu_g G(N)S \quad (2.8)$$

where  $\nu_g$  is the group velocity. In this context,  $\nu_g G(N)$  is the normalized differential gain (i.e., the differential gain normalized to the group velocity). From this point on, we will call  $G_N$  the differential gain. Thus, in terms of gain, Equation (2.7) can be re-written as

$$\frac{dS}{dt} = \Gamma G(N)S + \Gamma \beta_{sp} R_{sp} - \frac{S}{\tau_p} \quad (2.9)$$

Therefore, the carrier and photon density rate equations can be rewritten as

$$\frac{dN}{dt} = \frac{\eta_i I}{qV} - \frac{N}{\tau_c} - G_N(N - N_{tr})S \quad (2.10)$$

$$\frac{dS}{dt} = \Gamma G_N(N - N_{tr})S + \Gamma \beta_{sp} R_{sp} - \frac{S}{\tau_p} \quad (2.11)$$

where  $N_{tr}$  is the carrier density at transparency where the gain compensates totally the absorption. Equations (2.10) and (2.11) are valid for both above and below threshold.

### 2.1.3 Optical Gain and Laser Cavity

Optical gain is the fractional increase in light per unit length, which is proportional to the photon density and can only be accomplished through the process of stimulated carrier recombination. A simple formula for the optical gain  $G(N)$  is obtained by assuming a linear dependence on the carrier density  $N$  in the active region such as:

$$G(N) = G_N(N - N_{tr}) \quad (2.12)$$

where  $G_N$  is the differential gain coefficient  $\nu_g \partial g / \partial N$  (i.e. dynamic gain) and  $N$  is the carrier density injected into the laser. Optical gain alone is not enough to operate a laser, optical feedback is also necessary to establish amplified radiation and ensure laser oscillation as well as to sustain pumping levels above threshold. Optical feedback can be generated in many different ways but the simplest way to create it is by forming a laser cavity with

front–end cleaved facets, also known as partially reflecting mirrors. The laser cavity provides a direction selectivity for the process of stimulated emission because only photons traveling along its axis are reflected back and forth to experience maximum gain.

Although spontaneous and stimulated emission can also take place while current is applied to the junction, the laser does not generate the required coherence emission until the current exceeds the critical value, which is referred to as the threshold current,  $I_{th}$ . In other words, if the resulting gain is sufficient to overcome the losses of a resonant optical mode of the cavity, this mode is said to have reached threshold. For  $I_{th}$  to occur, it is required that the optical field in the cavity of the device is reproduced after each round trip. Therefore; the  $I_{th}$  conditions for self-sustaining oscillation of a FP laser can be expressed as:

$$\Gamma g_{th} = \alpha_i + \frac{1}{2L} \ln\left(\frac{1}{R_1 R_2}\right) \quad (2.13)$$

where  $\Gamma$  is the optical confinement factor,  $g_{th}$  the threshold gain,  $\alpha_i$  the internal loss in the active layer due to free-carrier absorption and scattering and  $L$  the cavity length bounded by the facets with power reflectivities,  $R_1$  and  $R_2$ . This equation indicates that at laser threshold, the gain balances exactly the losses.

The modal condition of the wavelength is given by

$$\beta L = m\pi \quad (2.14)$$

where  $\beta$  is the propagation constant,  $m$  the longitudinal mode integer. The optical confinement factor  $\Gamma$  in Equation (2.13) represents the fraction of the mode energy contained in the active layer. This factor is also known as the electron-photon overlap,  $V/V_p$ , where  $V$  is the volume of the active region occupied by electrons and  $V_p$  is the cavity volume occupied by photons. Thus,  $\Gamma$  accounts for the reduction in gain due to the spreading of the optical mode to the cladding/passive layers surrounding the active layer. The term  $\alpha_i$  takes

into account the internal losses of the cavity. Since the mirror loss term  $\alpha_m$  is defined as  $(1/2L)(\ln[1/R_1R_2])$ . Therefore, Equation (2.13) can be re-written as

$$\Gamma g_{th} = \alpha_i + \alpha_m \quad (2.15)$$

$\Gamma g_{th}$  is also referred to as the threshold modal gain because it represents the net gain required for the mode as a whole, and it is the mode as a whole that experiences the cavity loss [16]. Because photon losses occur within the cavity due to optical absorption and scattering out of the mode and the output coupling mirror where a portion of the resonant cavity mode is usefully coupled to some output medium [16]; the net loss by a photon lifetime can be characterized as  $\tau_p$  as previously discussed. Therefore, noting that the photon decay rate,  $1/\tau_p = \nu_g(\alpha_i + \alpha_m)$ ; Equation (2.13) can also be expressed as

$$\Gamma g_{th} = \alpha_i + \alpha_m = \frac{1}{\nu_g \tau_p} \quad (2.16)$$

Equation (2.14) is related to the phase and yields a condition on the modal  $\lambda = 2nL/m$ . It can be used to extract the lasing frequency  $\omega = \beta c$ , therefore:

$$\omega = \frac{m\pi c}{n_g} L \quad (2.17)$$

known as the cavity resonance frequency, which leads to  $m\frac{\lambda}{2} = nL$ . In this resonance condition,  $n$  is the refractive index of the active layer and  $c$  the speed of light in vacuum.

Equation (2.17) means that the laser tends to oscillate at a frequency that is a longitudinal mode supported by FP cavity. Interestingly, reaching the lasing threshold for one or more longitudinal modes depends on the characteristics of gain curve including the gain width and the gain broadening mechanism (whether homogeneous or inhomogeneous) [21]. In the case of homogeneous broadening, only one longitudinal mode, whose frequency coincides with the gain-peak frequency, reaches threshold and the laser remains in the single mode operation regime as shown in fig. 2.3.

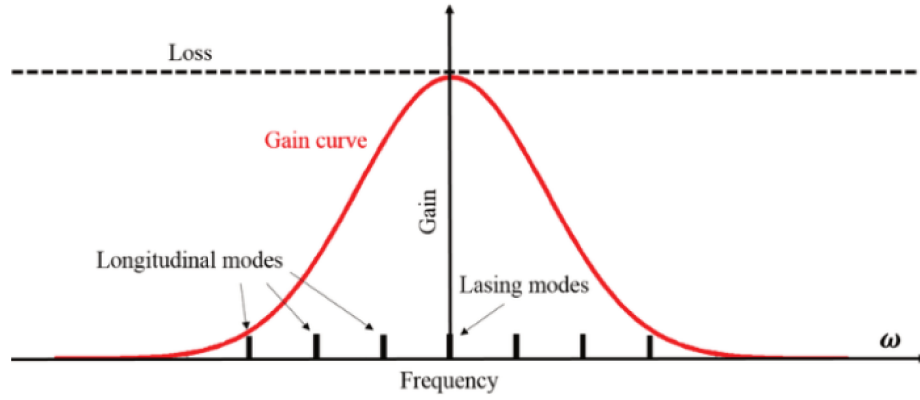


Figure 2.3: Schematic illustration of the gain curve and longitudinal modes of a semiconductor laser: cavity modes are given by  $m\frac{\lambda}{2} = nL$ , where  $m$  is an integer and  $n$  the effective refractive index [22].

In a SCL, the refractive index  $n$  (phase optical index) varies with  $\omega$  (material dispersion) and strictly speaking the intermode spacing  $\delta\omega$  is as follows:

$$\delta\omega = \frac{\pi c}{n_g} L \quad (2.18)$$

The optical group index  $n_g$ , which is dependent on frequency can be expressed as,

$$n_g = n + \omega \frac{\partial n}{\partial \omega} \quad (2.19)$$

$n_g$  in semiconductors is usually 20-30% larger than the index of refraction. This is a unique feature of this type of laser that the longitudinal frequencies and their separation vary with the external pumping, because of the refractive index modulation [22].

The round trip  $\delta\tau$  of the laser is related to the intermode spacing  $\delta\omega$  and is the inverse of the mode spacing

$$\delta\tau = \frac{2\pi}{\delta\omega} = \frac{2n_g L}{c} \quad (2.20)$$

The gain bandwidth of a SCL is very broad as compared to  $\delta\omega$ , the longitudinal modes spacing and in practice this generally results in multi-longitudinal mode operation. Nor-

mally, there are several modes that meet the phase condition described by Equation (2.14) and exhibit gains that are only slightly smaller ( $\approx 10^{-3} - 10^{-4}$ ) than the threshold gain (2.13). Single-mode operation can be achieved if the threshold gain for the oscillating mode is significantly smaller than that for the other modes.

#### 2.1.4 Light-Current Characteristic

The light-current (L-I) curve characterizes the emission properties of a SCL. It indicates the current that needs to be applied for a desired amount of power. The inter-band radiative recombination can lead to either spontaneous or stimulated emission. The steady-state gain in the laser operation above  $I_{th}$  must also equal its threshold value as given by Equation (2.13). That is, in a laser cavity,

$$G(N)(I > I_{th}) = g_{th}. \quad (2.21)$$

Furthermore, because the gain is monotonically related to the carrier density, this implies that the carrier density must clamp at its threshold value. That is,

$$N(I > I_{th}) = N_{th} \quad (2.22)$$

The stimulated recombination term  $R_{st}$  also increases, reducing the carrier density and gain until a new steady-state dynamic balance is struck where Equations. (2.21) and (2.22) are again satisfied [16]. Assuming a linear dependence of the optical gain on the carrier concentration, the ideal light-current characteristics (LCC) above the laser threshold can be obtained using the following relationship:

$$P(I) = \eta_i \left( \frac{\alpha_m}{\alpha_m + \alpha_i} \right) \frac{\hbar\omega}{2q} (I - I_{th}) \quad (2.23)$$

where  $\eta_i$  is the fraction of the terminal current that contributes to the generation of carriers in the active region and  $q$  is the electric charge. Equation (2.23) represents a linear LCC

as the one shown in fig. 2.4, where significant optical power can be achieved above the threshold current  $I_{th}$  and the round trip gain equals unity. This equation, takes into account the total power out of both mirrors.  $I_{th}$  can be defined as the output light power *vs* the pump, characterized by a sharp knee as illustrated below.

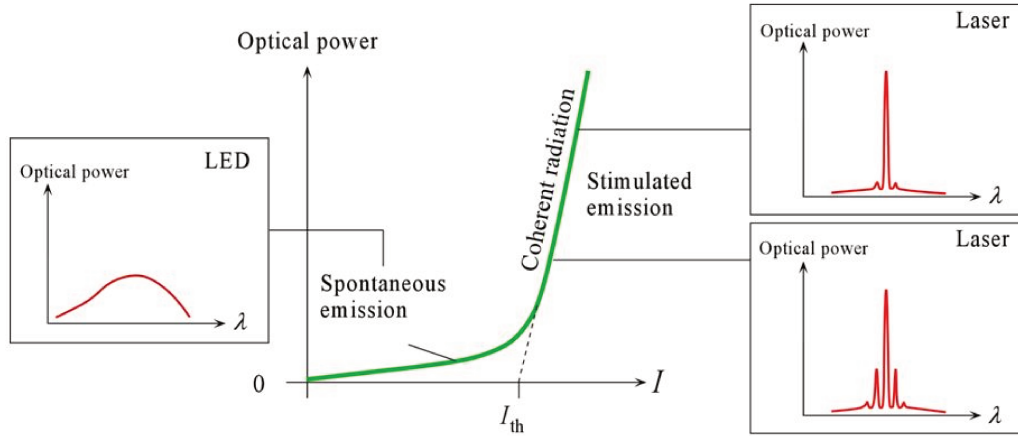


Figure 2.4: Output power versus current characteristics of a laser and its corresponding optical spectrum: below the threshold only spontaneous emission is important; above the threshold, the stimulation emission power increases while the spontaneous emission is clamped at its threshold level [23, 16].

Below this current, the power mainly consists of amplified spontaneous emission. Above  $I_{th}$ , the carrier density is fixed and the slope increases linearly with the injected current. The power of the curve is predominately constant until the power saturation mechanisms settle in. The saturation of the power is connected to the thermal heating of the device because the recombination coefficients and the bandgap depends on the temperature. Generally, additional current is required for both  $I_{th}$  and the increment above  $I_{th}$  as the temperature is increased. Therefore, the  $I_{th}$  dependence on the temperature  $T$  and its behavior can be empirically described as:

$$I_{th} \propto e^{\frac{T}{T_0}} \quad (2.24)$$

Where  $T_0$  represents the overall temperature characteristic; typical values of  $T_0$  are in the

range of 150-200K for GaAlAs lasers and between 40-70K for InGaAsP lasers.

Note that the small values of  $T_0$  indicate a larger dependence on temperature. Both the gain and internal loss variation result in an exponential temperature dependence of the threshold current.

### 2.1.5 Stability Analysis, Relaxation Oscillations and Damping

SCLs are class B lasers, meaning that  $\tau_c \geq \tau_p$ . Relaxation oscillations are inherent to this type of lasers [24]. In a SCL, the lasing field  $E$  can be described as [25]

$$\frac{dE}{dt} = \left\{ \frac{1 + i\alpha_H}{2} \left[ \Gamma G_N (N - N_{tr}) - \frac{1}{\tau_p} \right] + i\omega \right\} E \quad (2.25)$$

where  $\alpha_H$  is the linewidth enhancement factor defined by Equation (2.44) and  $\omega$  is the lasing angular frequency. By writing  $S = |A|^2$  and assuming the lasing field is in the form  $E = Ae^{i\omega t + i\phi}$ , thus by separating the real and the imaginary part of Equation (2.25), we obtain the photon density and the phase of the electric field rate equations

$$\frac{dA}{dt} = \frac{1}{2} \left[ \Gamma G_N (N - N_{tr}) - \frac{1}{\tau_p} \right] A \quad (2.26)$$

$$\frac{d\phi}{dt} = \frac{\alpha_H}{2} \left[ \Gamma G_N (N - N_{tr}) \right] - \frac{1}{\tau_p} \quad (2.27)$$

As opposed to Equation (2.11), the spontaneous emission term is neglected in Equation (2.26). Equation (2.10) can be rewritten in terms of the amplitude coefficient as

$$\frac{dN}{dt} = \frac{\eta_i I}{qV} - \frac{N}{\tau_c} - G_N (N - N_{tr}) |A|^2 \quad (2.28)$$

Therefore, the steady-state solutions  $A_s$ ,  $\phi_s$ , and  $N_s$  of equations (2.26)-(2.28) are given by

$$A_s^2 = \frac{\eta_i I / qV - N_s / \tau_c}{G_N (N_s - N_{th})} \quad (2.29)$$

$$\phi_s = 0 \quad (2.30)$$

$$N_s = N_{tr} + \frac{1}{\Gamma G_N \tau_p} = N_{th} \quad (2.31)$$

Note that for equation (2.30)  $\phi_s = 0$  when  $\omega_s = \omega$ . Since the laser is under steady-state ( $A_s \neq 0$ ), this leads to  $N_s = 0$  and  $A_s = P$ , where  $P = \tau_p G_N N_{th} / 2 = I / I_{th} - 1$ .

Assuming the presence of small perturbations around the steady-state can be expressed as

$$A = A_s + \delta A \quad (2.32)$$

$$\phi = (\omega_s - \omega_0)t + \delta \phi \quad (2.33)$$

$$N = N_s + \delta N \quad (2.34)$$

By injecting Equations (2.29)-(2.34), we get

$$\frac{\delta A}{dt} = \frac{1}{2} \Gamma G_N A_s \delta N \quad (2.35)$$

$$\frac{\delta \phi}{dt} = \frac{\alpha_H}{2} \Gamma G_N \delta N \quad (2.36)$$

$$\frac{\delta N}{dt} = -\frac{2A_s}{\Gamma \tau_p} \delta A - \frac{1}{\tau_c} \delta N - G_N A_s^2 \delta N \quad (2.37)$$

Rearranging Equations (2.35)-(2.37) yields the Jacobian Matrix  $M_j$  below:

$$\begin{bmatrix} \frac{\delta A}{dt} \\ \frac{\delta \phi}{dt} \\ \frac{\delta N}{dt} \end{bmatrix} = \begin{bmatrix} 0 & 0 & \frac{1}{2}\Gamma G_N A_s \\ 0 & 0 & \frac{\alpha_H}{2}\Gamma G_N \\ -\frac{2A_s}{\Gamma\tau_p} & 0 & -\frac{1}{\tau_c} - G_N A_s^2 \end{bmatrix} \times \begin{bmatrix} \delta A \\ \delta \phi \\ \delta N \end{bmatrix} = M_j \begin{bmatrix} \delta A \\ \delta \phi \\ \delta N \end{bmatrix} \quad (2.38)$$

Thus the solutions to Equations (2.35)-(2.37) can be extracted from the eigenvalues of the Jacobian Matrix. The characteristic equation solving the eigenvalue  $\xi$  is given by  $|M_j - \lambda I| = 0$

$$|M_j - \lambda I| = -\xi \left[ \xi^2 + \left( \frac{1}{\tau_c} + G_N A_s^2 \right) \xi + \frac{G_N A_s^2}{\tau_p} \right] = 0 \quad (2.39)$$

where the trivial solution  $\xi = 0$  and the two other solutions are given by

$$\xi = -\frac{1}{2} \left( \frac{1}{\tau_c} + G_N A_s^2 \right) \pm \sqrt{\frac{1}{4} \left( \frac{1}{\tau_c} + G_N A_s^2 \right)^2 - \frac{G_N A_s^2}{\tau_p}} \quad (2.40)$$

As previously discussed, in class B lasers,  $\tau_c \geq \tau_p$ , therefore, the term inside the square root is negative, thus the solution becomes complex with

$$\xi = -\frac{1}{2} \left( \frac{1}{\tau_c} + G_N A_s^2 \right) \pm i \sqrt{\frac{G_N A_s^2}{\tau_p} - \frac{1}{4} \left( \frac{1}{\tau_c} + G_N A_s^2 \right)^2} = \xi_{Re} + i \xi_{Im} \quad (2.41)$$

where the relaxation oscillation frequency (ROF)  $f_r$  and the damping factor  $\gamma$  are defined from the real part  $\xi_{Re}$  and the imaginary part  $\xi_{Im}$  such as [25]

$$f_r = \frac{1}{2\pi} \sqrt{\frac{G_N A_s^2}{\tau_p}} \quad (2.42)$$

$$\gamma = \frac{1}{2} \left( \frac{1}{\tau_p} + G_N A_s^2 \right) \quad (2.43)$$

In Equation (2.41), since  $\tau_c$ ,  $G_N$  and  $A_s$  are positive meaning that  $\xi_{Re} < 0$ , thus the steady-

state solutions are always stable. In Equation (2.42), the steady-state field amplitude  $A_s$  increases with the bias current, leading to the increase of the ROF as well as the damping. The ROF is also known as optical perturbations. These oscillations are usually damped and eventually lead back to the steady state of photons and carriers because any disturbances or perturbations decay with time. For operation just above the laser threshold, the relaxation oscillations are slow, and their damping time is about twice the upper-state lifetime of the gain medium [26]. For higher powers, the oscillations can be faster, and the damping time gets shorter. One can then say that the resonance is damped at low and high output powers. This happens because the imaginary damping term depends on  $\omega_r$  as defined by Equation (4.1) in the presence and absence of optical feedback [16].

The high-speed devices studied herein exhibit strongly damped relaxation oscillations with very high frequencies in the gigahertz region. This pronounced oscillatory behavior can be observed in the experimental results provided in Chapter IV [27]. It is important to note that  $f_r$ ,  $\gamma$  and the  $\alpha_H$  are key parameters in SCLs as they fundamentally drive the laser's dynamics discussed in Chapter III. Due to the inhomogeneous broadening and the high gain compression effects discussed in Section 2.1.7, the ROF is further reduced as well as the 3-dB modulation bandwidth [16].

#### 2.1.6 Linewidth Enhancement Factor

The linewidth enhancement factor (LEF), also known as the  $\alpha_H$  [28] factor or the linewidth broadening factor is of paramount importance for SCLs because it is one of the most distinctive features that differentiates the behavior of a SCLs with respect to other types of lasers. It quantifies the coupling between the real and imaginary parts of the material's nonlinear susceptibility, i.e. between the differential gain and the refractive index, or equivalently the coupling between the amplitude and the phase of the electric field in the laser cavity [29]. The linewidth is dependent on the reflectivity of the mirrors. Decreasing, the mirror reflectivity affects the mode structure; the higher the reflectivity of the mirrors, the

narrower the linewidth, which is an essential feature for coherent communication systems. The  $\alpha_H$  factor impacts several fundamental aspects of SCLs to include chirp under current modulation, linewidth (that is proportional to the factor  $(1 + \alpha_H^2)$ ), sensitivity to optical feedback, mode stability and the occurrence of filamentation in broad-area devices [30]. In other words, the LEF is a fundamental feature in SCLs and is responsible amongst other consequences for a large spectral linewidth broadening.

Historically the  $\alpha_H$  factor was first introduced simultaneously in 1967 by Lax [31] and Haug Haken [32]. Using either quantum calculations from the density matrix equations or a semi-classical theory, both have introduced a factor of  $(1 + \alpha_H^2)$  to describe the noise-induced phase fluctuations that also appear in the equation setting the spectral linewidth. However, the former did not further exploit the spectral linewidth equation, whereas the latter did not consider the  $\alpha_H$  factor since it was too small as compared to unity. In 1982, Henry [28] reintroduced the  $\alpha_H$  factor and fully theorized the spectral linewidth of semiconductor lasers. Typical values of the  $\alpha_H$  factor range between 2 to 5 for bulk and QW materials. The  $\alpha_H$  factor can be defined as [33]:

$$\alpha_H = -\frac{d[\Re\{\chi(n)\}]/dn}{d[\Im\{\chi(n)\}]/dn} = -\frac{4\pi}{\lambda G_N} \frac{dn}{dN} \quad (2.44)$$

where  $n$  is the electron concentration,  $\lambda$  the lasing wavelength,  $G_N$  is used to defined the differential gain, and  $\frac{dn}{dN}$  the differential index. In synthesis, the dynamics of SCLs are greatly influence by the  $\alpha_H$  when studying the effects of optical feedback. Furthermore, the LEF significantly influences the nonlinear dynamics of a SCL subject to optical injection or optical feedback, and nonlinear dynamics can only be observed in lasers for which  $\alpha_H > 0$  [33]. The birth of the  $\alpha_H$  traces back to the early 80s, when the first measurements revealed that the linewidth of a SCL was much broader than predicted by the Shawlow-Townes theorem [34]. A theoretical explanation soon came from Henry, who then developed a theory that ascribes the excess linewidth to the joint action of spontaneous emission events and population inversion (i.e., carrier) relaxation, through the mechanism of index-gain cou-

pling [28]. The latter represents the fact that in a semiconductor medium, both the optical gain and the refractive index depend on the actual carrier density. Since then, a number of theoretical and experimental efforts have been carried out in an attempt to calculate the dependence of the  $\alpha_H$  on the LD material parameters and to measure its value in practical parameters.

### 2.1.7 Gain Compression

It has been extensively demonstrated both theoretically and experimentally that above threshold some additional effects such as gain compression significantly impact the  $\alpha_H$  factor [35]. Gain compression in SCLs corresponds to the decrease of the gain coefficient with optical intensity. Several processes such spatial hole burning (SHB) and carrier heating (CH), contribute to the gain compression in these devices [36, 37].

The nonlinear  $g_{nl}$  is defined as

$$g_{nl} = \frac{g}{1 + \epsilon_p P} \quad (2.45)$$

Where  $g$  is the uncompressed material gain,  $P$  the output power, and  $\epsilon_p$  the gain compression coefficient related to the output power. The gain compression has a direct impact on the above-threshold  $\alpha_H$  factor. For instance, in QW lasers, which are made from a nearly homogeneously-broadened gain medium, the carrier density is clamped at threshold and the change in  $\alpha_H$  factor is due to the decrease of the differential gain from gain compression. As a result, the change of the  $\alpha_H$  factor that is mostly due to the gain compression can be expressed as follows:

$$\alpha_H(P) = \alpha_{H0}(1 + \epsilon_p P) \quad (2.46)$$

Where  $\alpha_{H0}$  is the  $\alpha_H$  factor at threshold. Since the carrier distribution is clamped,  $\alpha_{H0}$  itself does not change as the output power increases. There is still not “one systematic

approach fits all” laser structures. Therefore, different methods must be used accordingly to measure the  $\alpha_H$  factor since the above threshold could behave differently from laser to laser. In inhomogeneous gain broadening in gain media such in the case of quantum dot (QD) laser, the carrier density and distribution are not clamped as in QW devices. This phenomenon is substantiated by the fact that a QD can switch to excited-state lasing from ground-state lasing as the current injection increases, indicating a carrier accumulation in the excited states even though the ground state is lasing [35]. The filling of the excited states inevitably increases the  $\alpha_H$  factor of the ground-state [38], introducing additional dependence of the alpha parameter on the output power.

## 2.2 Classification of Semiconductor Devices

### 2.2.1 Fabry-Perot Lasers

FP cavities are the most common and simplest laser cavities consisting of two planar mirrors and an optical gain medium as illustrated in fig. 2.5 left. The cavity of this laser can be realized by cleaving the end facets along the proper crystal planes to allow free-space light propagation. Because of the high optical gain of a SCL, the optical feedback provided by the natural reflectivity from the cleaved facets is generally sufficient for laser oscillation. The manufacturing process of a FP laser, consist of a *pn* heterojunction grown epitaxially, and then cut in order to create bars approximately as long as the final cavity.

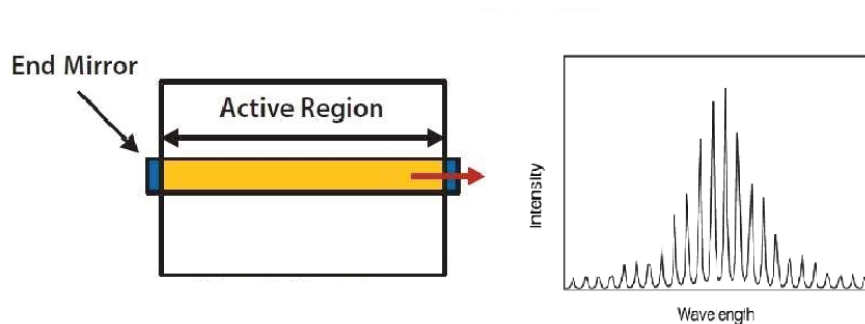


Figure 2.5: Fabry-Perot: Device schematic and laser spectrum [39].

### 2.2.2 Distributed Bragg Reflector Lasers

Distributed Bragg Reflector (DBR) used Bragg grating mirrors as the basis of operation. The mirrors consist of a series of relatively small impedance discontinuities (reflections) along the axial propagation direction ( $z$ -axis), phased so that the reflections add constructively at some (Bragg) frequency to a large net reflection [16]. DBRs are employed in-plane periodic structures to provide distributed selective feedback. The built-in grating leads to a periodic perturbation in the refractive index where feedback occurs by Bragg diffraction. The first order gratings are generally formed in the DBR regions with a coupling coefficient,  $\kappa$  of about  $100 \text{ cm}^{-1}$ . The longitudinal mode closest to the Bragg wavelength has the lowest threshold gain. The Bragg wavelength  $\lambda_B$  is related to the pitch of the grating  $\Lambda$ :

$$\Lambda = q \frac{\lambda_B}{2n} \quad (2.47)$$

where  $n$  is the mode effective refractive index and the integer  $q$  represents the order of the Bragg diffraction. For instance, a first order grating has a pitch of  $0.23 \mu\text{m}$  at a wavelength of  $1.5 \mu\text{m}$  and for a typical effective refractive index value of  $n_{eff} \approx 3.4$ . DBR lasers use gratings etched outside the active region. These unpumped corrugated regions act as frequency selective mirrors. Here optical gain and wavelength tuning are provided by the active region and the Bragg section, respectively. The passive phase-control section can be used to ensure single-mode operation. A DBR laser is usually designed such that the dominant mode has a threshold gain of about  $8\text{-}10 \text{ cm}^{-1}$  lower than the neighbor modes. These modes are typically suppressed by  $\approx 30 \text{ dB}$ . In contrast to FP lasers, the longitudinal modes of a DBR laser are not equi-spaced. Because of their spectral purity and practicality for wide wavelength tunability, DBR lasers have been successfully deployed in modern fiber optics networks and continue to be promising devices for applications in optical fiber communications schemes.

### 2.2.3 Distributed Feedback Lasers

Just as DBR lasers, distributed feedback (DFB) devices also use grating mirror but in this case gain is included in the grating, thus this configuration is simpler to fabricate because no active-passive transitions are necessary. A theoretical laser based on DFB was introduced by Bell Laboratories in 1972 [40]. A DFB device functions as a FP cavity, except that the fact a Bragg grating is integrated with the gain region as a DFB mechanism between two end mirrors as illustrated in fig. 2.6. The DFB grating is an index or gain periodic perturbation in an active waveguide that provides frequency-selective feedback. Therefore, a DFB laser without a structural phase shift in its grating has a high threshold and oscillates in two modes.

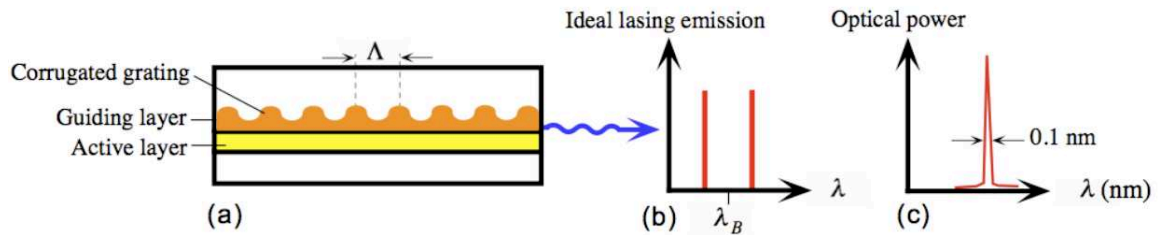


Figure 2.6: (a) DFB structure laser structure; (b) Lasing emission output; (c) Optical spectrum [13].

Nakamura *et al* [41] fabricated the first DFB structure in 1974, two years after the theoretical approach was formulated. The laser structure was developed using holographic lithography to define a grating in p-GaAs as presented in fig. 2.7.

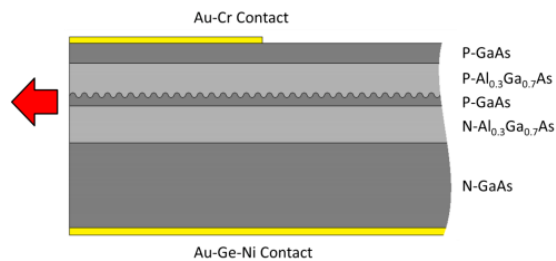


Figure 2.7: First fabricated DFB structure [41, 42].

The grating in a DFB cavity provides all of the optical feedback required for laser oscillation. The oscillation condition of a DFB laser can be found by considering the fact that when a laser mode is oscillating, there is a laser output without an optical input at that particular mode frequency. The end facets of a DFB laser are anti-reflection (AR) coated in order to eliminate any possible reflections from the facets. Generally, the transition between these two structures leads to an improvement of the temperature stability in the emitted wavelength. In a DFB device, an optical wave traveling in one direction is reflected by the grating into a wave traveling in the opposite direction and vice-versa [43]. Since it is not very practical to cleave and make coatings on integrated lasers, the simplest way to fabricate a single mode laser is to introduce a quarter-wave ( $\lambda/4$ ) phase shift in the middle of the DFB cavity [44] to ensure that there are not reflections in the chipset. A DFB laser with a proper structural phase shift has a lower threshold with only one oscillating mode. Because the grating in a DFB laser runs along the length of the active region where optical gain exists, the device then functions as a frequency-selective contra-directionally coupled amplifier for the intracavity laser field [45] because periodic perturbations in the refractive index along the laser cavity provide frequency-selective feedback. Its output power capability is also lower than the FP type with one selected wavelength, hence it provides a narrow spectral width of less than 0.1 nm.

The properties of a DFB laser depend on the grating strength  $k$ , also known as the grating coupling coefficient proportional to the index variation. Basically, this coefficient allows to estimate the strength of the interaction between the optical fields. This parameter is mostly linked to the grating profile, its position from the active region as well as the thickness and composition of the different layers of the waveguide. Also, it should be noted that the coupling coefficient has a strong impact on the laser's external optical feedback sensitivity.

Several approaches exist to develop DFB devices. However, the most known approach consists of a structure with an AR and a high reflection coating. AR coatings are assumed to avoid additional reflections. Therefore, this design leads to single mode operation of the de-

vice with strong side mode suppression ratio (SMSR) and large output power as described theoretically in [46]. Experiments conducted have demonstrated that a SMSR of at least 30 dB is necessary for single-frequency system applications [47]. The SMSR increases with the increasing threshold gain margin and the threshold gain margin depends on the cleavage position in the grating [48]. DFB devices still suffer from wavelength chirp during high-speed modulation and during ultra-short light pulse generation because the carrier-induced variation of the refractive index of the laser cavity causes the effective pitch of the grating to change. Additional information on DFB laser and a comprehensive description of the structure can also be found in [44]. A study on DFB devices and associated performance characterization results is provided in Chapter IV.

## **2.3 Semiconductors Under Study**

### 2.3.1 Tunable Lasers

A TUL is a device whose wavelength of operation can be adjusted in a controlled manner. When a laser is tuned, the device jumps from one wavelength to another corresponding to the resonance modes of the laser cavity [49]. Several key tunable designs have been proposed as presented in [50, 51] but the operation principle remains the same. The design is based on the DBR configuration [50] where a waveguide corrugation, which forms a grating, functions as a basic element of single mode selection and tunability [52]. In this case, the grating mirror has a narrow spectral reflectivity centered on the Bragg wavelength. There are three configurations to achieve a tunable laser, which are DBR diode laser with Bragg wavelength control, those with phase control and those with Bragg wavelength and phase control, the combination of control of Bragg wavelength and phase results in a widely tunable range [53]. In some instances a booster SOA placed after the laser can be used to manage losses and enhance the output power of the device.

Fig. 2.8 illustrates the schematic of a genetic tunable single-frequency laser; which consists of a front and a back mirror as well as an active and passive region in addition to the passive

grating. One section provides gain, one allows phase control and one can shift the mode-selective grating filter, respectively [47]. The mirrors are what gives the laser its name, “sample grating”. A conventional DBR mirror is formed by a continuous grating having a narrow reflectivity spectrum that is used to select the desired channel. The full range tuning of a SCL can be achieved with this configuration. A number of novel configurations have been proposed including structures that employ two different multi-element mirrors to create two reflection combs with the different wavelength spacings and a Vernier-effect tuning enhancement [54]. The widely tunable laser, which is based on two sampled gratings DBR (SG-DBR) in a Vernier configuration is designed to produce a periodic reflectivity spectrum as described in [55].

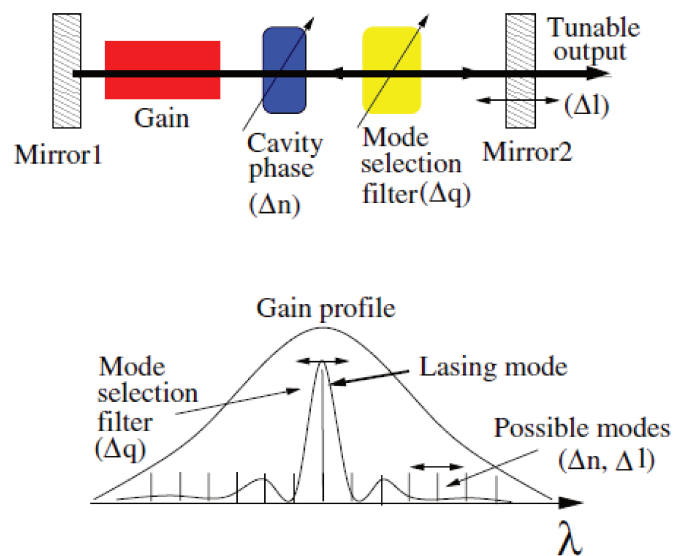


Figure 2.8: Tunable single laser and gain profile [53].

Jayaraman *et al.* [54] gave the first detailed description of widely tunable DBR lasers using sampled-grating theoretically and experimentally, achieving a tuning range of 57 nm limited by the beat period.

Fig. 2.9(a) depicts the first monolithic SG-DBR device to ever tune over a range of 30 nm [54]. The originally proposed four section design and Vernier mirror tuning concept,

along with the early discontinuous tuning concept that used only three-section are illustrated above. A sampled grating is a modification of the DBR continuous grating in which the grating teeth are periodically removed along the length of the grating as depicted in fig. 2.9(b).

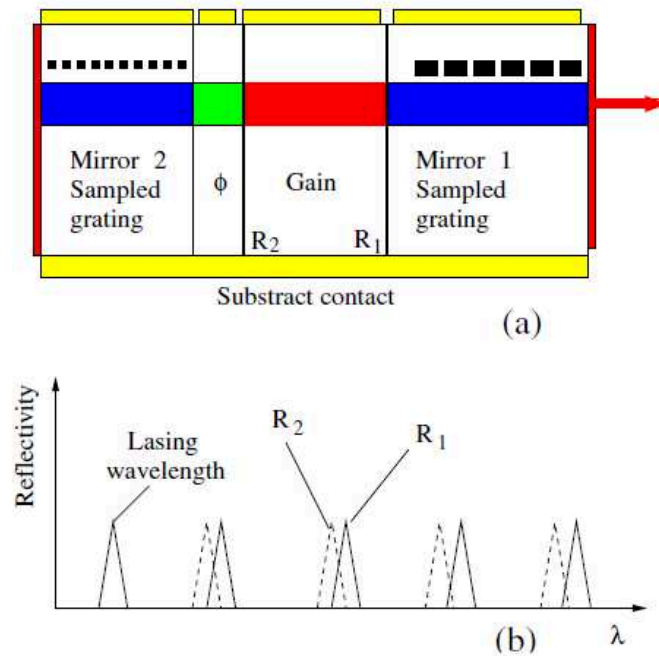


Figure 2.9: Tunable laser based on mirrors with periodic spectra: (a) Schematic of a SG-DBR displaying the four sections used to select the power and desired channel; (b) Vernier effect, two reflection combs from mirror 1 and mirror 2 [53].

By sampling the grating, multiple reflection peaks are then formed. These peaks are spaced apart in wavelength at a period inversely proportional to the period of the sampling. The front and back mirrors of the laser are sampled at different periods such that only one of their multiple reflection peaks can coincide at a time, as shown in fig. 2.10. This is known as the Vernier effect. In this way the desired channel can be selected by tuning the two mirrors such that the closest reflection peak of each mirror is aligned at the desired channel for lasing occurs [51].

When a DBR mirror section is tuned, two effects come into play, 1) the grating Bragg wavelength will vary due to the changed grating index; 2) the cavity mode position will

change also because the effective optical cavity length is now different. At the same time, the cavity modes will shift and subsequently, the new lasing mode will be the cavity mode that is the closest to the Bragg wavelength [16].

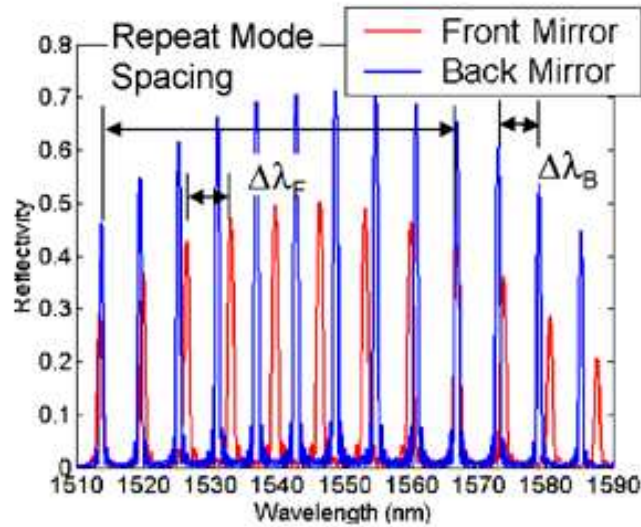


Figure 2.10: Reflectivity spectrum of the sample grating mirrors showing the multiple mirror peaks to cover the tuning range [51].

The SG-DBR structure is a very elegant solution that addresses the need for wide tuning range lasers. The SG-DBR laser is probably the most flexible and extendible tunable laser architecture available today. It is widely tunable and can also be monolithically integrated with an SOA for high power, long haul applications, or an electro-absorption modulator (EAM) for metro-core applications [51]. However, there are some challenges associated with the required sensitivity to cover a narrower tuning range in addition to the very precise wavelength selection and high stability. The SG-DBR overcomes this conflict by using a tuning mechanism with two degrees of freedom.

The bell shape of the SG-DBR reflectivity envelope is not very favorable for a wide tunability due to the Vernier side mode competition. In order to overcome this issue, a superstructure grating (SSG-DBR) concept has been proposed. This structure shares most of the features of the SG-DBR design but instead, the desired multi-peaked reflection spec-

trum of each mirror is created using a phase modulation of grating rather than an amplitude modulation function as in the SG-DBR [51]. In this complex approach, the grating is carefully designed with several phase shifts to obtain a square reflectivity envelope with a complex design. Periodic bursts of a grating with chirped period are typically used. This multi-element mirror structure requires a smaller grating depth and can provide an arbitrary mirror peak amplitude distribution if the grating chirping is properly controlled.

Furthermore, a ring resonator (RR) tunable laser design has also been introduced in [56] in an InP platform with low tuning power consumption with a limited 30 dB side mode suppression ratio and a 40 nm tuning range. This design provides a strong mode selection filtering. Only light at the resonance wavelength can be effectively coupled from the gain region to the front or back of the passive waveguide and reflected by one or both facets to the gain region via the ring resonator again. The schematic of a RR based laser and its stack structure is presented in fig. 2.11(a) and fig. 2.11(b) respectively.

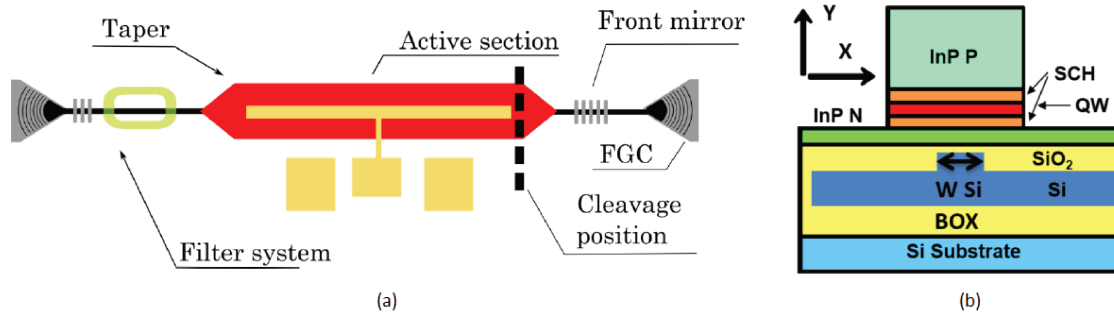


Figure 2.11: (a) Schematic of the hybrid III-V/Si tunable laser and (b) Stack structure of the device [57].

In this design, the laser cavity is shared between the III-V material and Si. The structure is composed of a back Bragg mirror, a filter system, a III-V transition, a gain section, another III-V transition and a front Bragg mirror. In this particular design adopted from III-V Lab, the confinement in the QWs is 10%. After the front mirror, light is out-coupled by a focusing grating coupler (FGC) at the vertical of the chip. The laser can also be cleaved in the III-V region to minimize the coupling losses. Light is then edge coupled with a lensed

fiber. To obtain a single mode laser with a RR filter system, there are two design rules:

- The filter selects a single FP mode. This means that the 3 dB bandwidth of the filter must be around the FP cavity spacing  $\Delta\lambda_{FP} = \lambda^2/2n_gL$  where  $L$  is the cavity length and  $n_g$  the group index
- The filter selects one FP mode on the 3 dB bandwidth of the gain medium ( $\approx 30$  nm), thus the filter free spectral range (FSR)<sub>F</sub> must be greater than this value.

There are two variations of RR, single and double. Using a single RR provides a simple tuning mechanism through the heater on top of the RR to tune the wavelength. A double ring configuration in a Vernier configuration was proposed in [58] by Lelievre *et al.* The schematic of double RR is displayed in fig. 2.12.

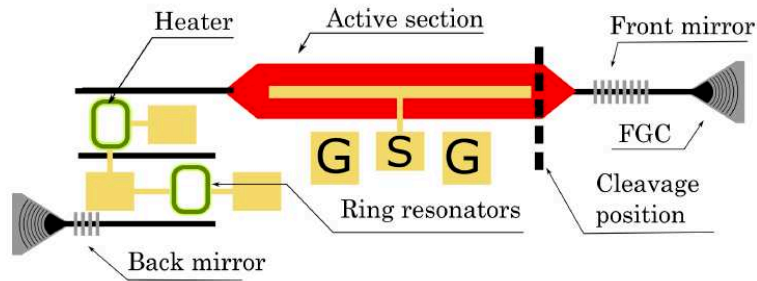


Figure 2.12: Schematic of a double RR laser design [57].

Since the two rings have slightly different radii; therefore, the FSR is also different such that the two ring combs have only one coincidence in the gain window [57].

Therefore, the two sets of transmission peak combs have small different peak spacing. The operation principle of this device is displayed in fig. 2.13. When current is applied to the resistor on top of the ring, the refractive index is changed by the thermo-optic effect and the comb is shifted in the longer wavelength. If the ring with small FSR is tuned, the coincidence wavelength is shifted in the longer wavelength as illustrated in 2.13(b). The opposite yields for the ring with the larger FSR. Additional information on double RR resonators under optical feedback is provided in Chapter IV.

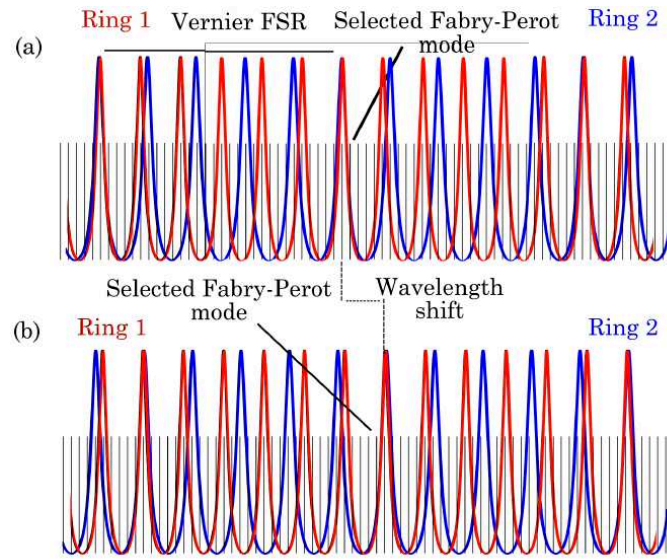


Figure 2.13: (a) Operation principle of a double RR filter, (b) Response of the device after tuning the ring with the smaller FSR, thus having a new coincidence with a longer wavelength [59].

These type of devices are more versatile and offer filtering properties since the FSR and bandwidth are easily controlled. Similar to SG and SSG-DBR lasers, wavelength tuning is achieved by aligning the peaks in the two sets of combs with adjustment of index in one or both ring resonators. Compared to SG and SSG-DBR lasers, double ring resonant coupled lasers could offer a much larger tuning enhancement because of uniform peak transmission and ultra-narrow bandwidth. Generally, tunable lasers has found multiple important applications in many fields. Many proposed wavelength division multiplexing (WDM) systems require the ability to switch between different wavelengths. In a WDM scheme, several wavelengths are modulated and multiplexed into one fiber. This approach is appropriate in a wide area telecommunication backbone network where tuning is used to configure and re-configure routes through the network [49].

Therefore, these devices are considered key optical components in optical communications systems because of their suitable wavelength range flexibility and adaptability in metropolitan and long distance networks.

### 2.3.2 Hybrid III-V/Silicon DFB Lasers

The hybrid laser consist of a heterogeneous integration approach of bonding III-V materials such as InP onto the Si waveguide as discussed in Chapter I. This is presently the most successful method for fabricating lasers integrated on Si. The use of these two materials combined brings great advantages to include the high optical gain offered by Si and the efficient light emission available in III-V materials. The hybrid III-V/Si structure consists of a III-V QW region bonded to a SOI wafer.

Various approaches can however, be taken when designing a hybrid waveguide to ensure coupling between the Si and the III-V material. In addition, the design of these devices can be manipulated in order to meet the desired performance characteristics. A proposed designed can be based on evanescent coupling, where most of the light is guided by the Si waveguide, and a small amount of light is evanescently coupled to the III-V material as illustrated in fig. 2.14(a). In this configuration, the optical cavity is defined in the Si using a variety of reflector structures such as Bragg gratings and RR as described in [60]. Another approach is to build the cavity in the III-V material and to evanescently couple the laser to the Si waveguides, as shown in fig. 2.14(b) to mainly confined the light in the III-V material.

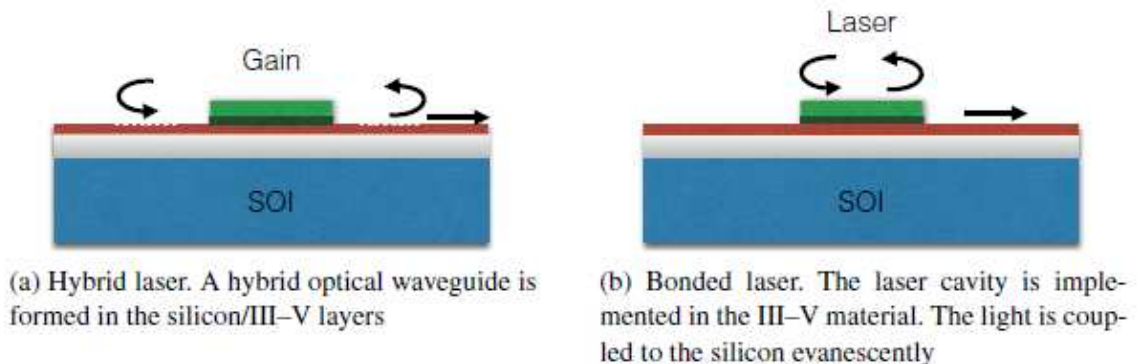


Figure 2.14: Hybrid silicon structures where the gain material is bonded to the silicon waveguide. The laser cavity can be implemented either in the III-V material or in the SOI material [60].

Coupling can then be performed using tapered waveguides to a cavity defined in Si [61]. Another method is to mainly confine the light in the III-V material, but evanescently couple to a Si Bragg grating waveguide thereby resulting in a distributed DFB laser [61]. To achieve a III-V on Si gain region, light is transferred from the Si to the III-V waveguide and vice versa. When the width of the Si waveguide  $W_{Si}$  is modified, the effective index of the Si waveguide varies concurrently. When the effective index is altered, the optical energy repartition between Si and III-V changes also.

The simulated field insensitive for three different Si rib widths is depicted in fig. 2.15 indicating that the mode distribution can be controlled. In this figure, the lateral  $x$  direction is in the plane of the substrate and vertical to the substrate is the transverse  $y$  direction. The  $z$ -axis is referred to as the optical propagating axis or the axial direction.

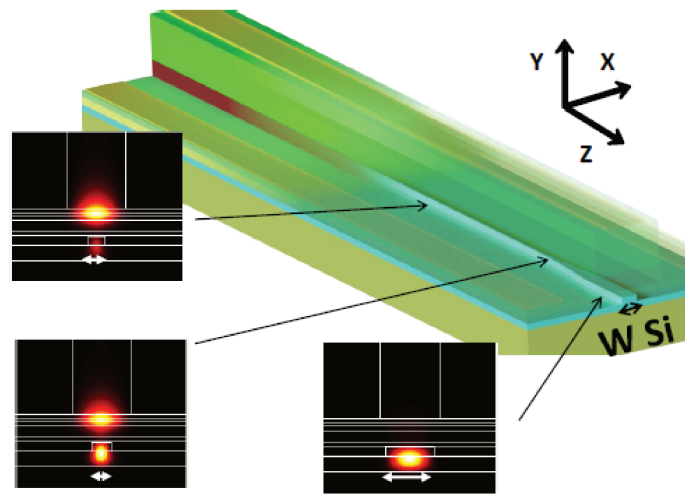


Figure 2.15: 3D view of a III-V on Si waveguide. The with  $W_{Si}$  of the Si waveguide controls the confinement in the III-V region. [59].

As shown, an adiabatic taper structure is designed to transfer the mode from Si to the III-V region. The gain region is then inserted inside a III-V on Si optical resonator to create the laser. After the mirror, the output power of the device is collected using Vertical Bragg Gratings (VBG) as revealed in fig. 2.16(b).

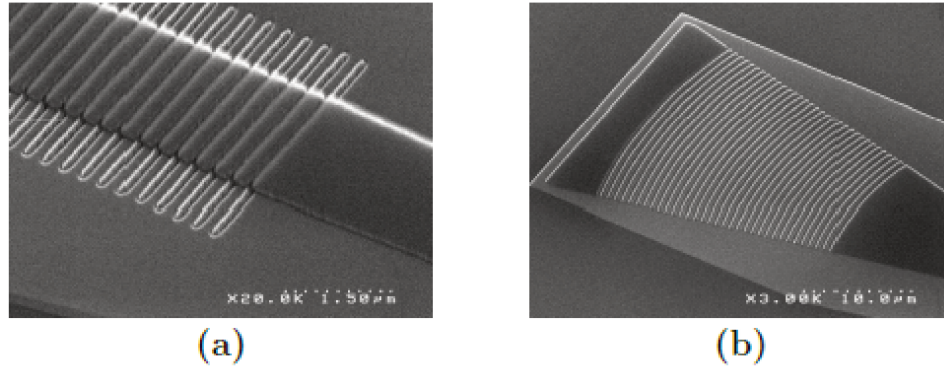


Figure 2.16: Scanning electron microscope image of (a) a Bragg grating and (b) a focusing grating coupler [57].

The grating of a III-V/Si device is made by etching teeth in the upper part of the laser waveguide as shown in fig. 2.17(a). The transverse cross section of this device is displayed in fig. 2.17(b), where the Si waveguide width  $W_{Si}$  controls the mode properties. As in a tunable laser, the cavity is shared between the III-V and Si material. The bonding oxide separates the two waveguides as discussed in [57]. The top view with the yellow etched region is illustrated in fig. 2.17(c).

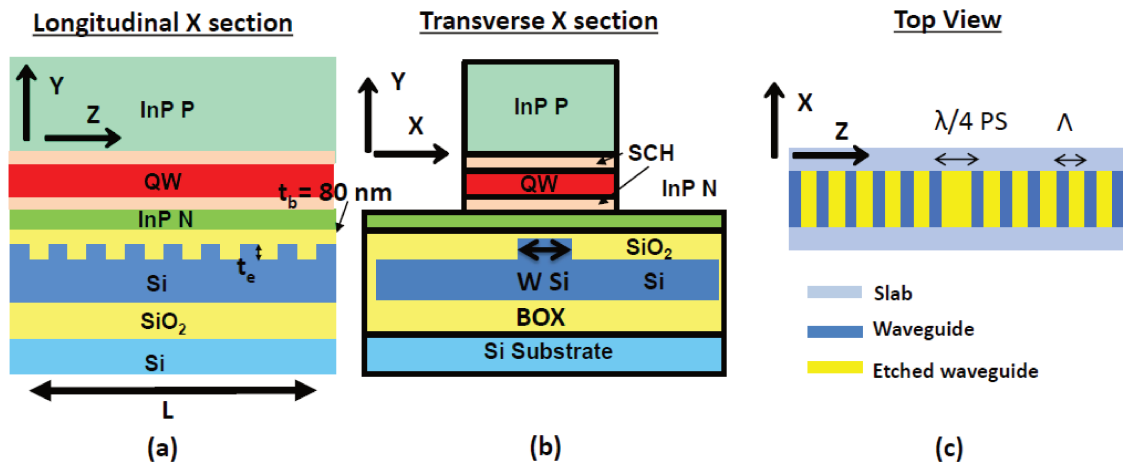


Figure 2.17: III-V on silicon DFB structure. (a) Longitudinal cross section. Grating is made on top of the silicon waveguide. (b) Transverse cross section. DFB parameters depends on the rib width  $W_{Si}$ . (c) Top view featuring the slab (light blue), the waveguide (blue) and the etched region (yellow). A  $\lambda/4$  phase shift is inserted in the centre of the cavity [57].

In the center of the cavity, two teeth are also etched to form the  $\lambda/4$  shift previously dis-

cussed. When  $W_{Si}$  is narrow, the mode is highly confined in the III-V material. Conversely, when the Si waveguide is thicker, the mode is confined in the Si waveguide instead. Some of the challenges associated with these type of devices lie in carefully designing the III-V region to define the tapers for the transition section between the hybrid and the Si waveguides to ensure low optical loss. This is because that part of the taper is built using III-V materials that may possibly have surface recombination which can also contribute to insertion losses between the III-V and Si regions.

A schematic of the device is provided in Chapter IV, fig. 4.10 along with detailed information on the structure's features. In addition, performance characteristics to include solitary measurements as well as maps of the optical and frequency spectra of the device when subject to optical feedback are provided.

## REFERENCES

- [1] P. L. D. et al., “Semiconductor lasers,” in *Handbook of Optics*, I. McGraw-Hill, Ed., Second Edition. 1995, vol. 1.
- [2] H. H. Telle and Á. G. Ureña, “Laser sources based on gaseous, liquid, or solid-state active media,” in *Laser Spectroscopy and Laser Imaging*, CRC Press, 2018, pp. 69–97.
- [3] R. N. Hall, G. E. Fenner, J. D. Kingsley, T. J. Soltys, and R. O. Carlson, “Coherent light emission from GaAs junctions,” *Physical Review Letters*, vol. 9, no. 9, pp. 366–368, 1962.
- [4] M. I. Nathan, W. P. Dumke, G. Burns, F. H. Dill, and G. Lasher, “Stimulated Emission of Radiation from GaAs p-n Junctions,” *Applied Physics Letters*, vol. 1, no. 3, pp. 62–64, 1962.
- [5] N. Holonyak and S. F. Bevacqua, “Coherent (Visible) Light Emission from Ga(As<sub>1-x</sub>P<sub>x</sub>) Junctions,” *Applied Physics Letters*, vol. 1, no. 4, pp. 82–83, 1962.
- [6] T. M. Quist, R. H. Rediker, R. J. Keyes, W. E. Krag, B. Lax, A. L. McWhorter, and H. J. Zeigler, “Semiconductor Maser of GaAs,” *Applied Physics Letters*, vol. 1, no. 4, pp. 91–92, 1962.
- [7] M. Panish, I. Hayashi, and F. Reinhart, “Properties of double heterostructure injection lasers: Continuous room-temperature operation,” in *1970 International Electron Devices Meeting*, IRE, 1970.
- [8] I. Hayashi, M. B. Panish, P. W. Foy, and S. Sumski, “Juntion lasers which operate continuously at room temperature,” *Applied Physics Letters*, vol. 17, no. 3, pp. 109–111, 1970.
- [9] H. Ghafouri-Shiraz, *Principles of semiconductor laser diodes and amplifiers: Analysis and transmission line laser modelling*. Imperial College Pr, 2003, ISBN: 1-86094-341-1.
- [10] K. Kao and G. Hockham, “Dielectric-fibre surface waveguides for optical frequencies,” *Proceedings of the Institution of Electrical Engineers*, vol. 113, no. 7, pp. 1151–1158, 1966.
- [11] V. Swaminathan, J. W. Little, and R. L. Tober, “Infrared detectors and lasers operating in the 3-12  $\mu\text{m}$  range using band-gap engineered structures with type II band-

- gap alignment,” in *Quantum Sensing and Nanophotonic Devices III*, M. Razeghi and G. J. Brown, Eds., SPIE, 2006.
- [12] H. Lei, “GaAs-based distributed feedback lasers based on GaAs-InGaP regrowth technology,” PhD thesis, University of Sheffield, 2017.
- [13] F. Grillot, *Advanced semiconductor lasers*, 2010.
- [14] *Heterostructure lasers*. Elsevier, 1978.
- [15] A. Levi, “Essential semiconductor laser device physics,” in. IOP Publishing, 2018.
- [16] L. A. Coldren, S. W. Corzine, and M. L. Mašanović, *Diode lasers and photonic integrated circuits*. John Wiley & Sons, Inc., 2012.
- [17] G. Agrawal, *Long-wavelength semiconductor lasers (van nostrand reinhold electrical/computer science and engineering series)*. Springer, 2012, ISBN: 9789401169967.
- [18] S. Chen, W. Li, J. Wu, Q. Jiang, M. Tang, S. Shutts, S. N. Elliott, A. Sobiesierski, A. J. Seeds, I. Ross, P. M. Smowton, and H. Liu, “Electrically pumped continuous-wave III–V quantum dot lasers on silicon,” *Nature Photonics*, vol. 10, no. 5, pp. 307–311, 2016.
- [19] J. Selvidge, J. Norman, M. E. Salmon, E. T. Hughes, J. E. Bowers, R. Herrick, and K. Mukherjee, “Non-radiative recombination at dislocations in InAs quantum dots grown on silicon,” *Applied Physics Letters*, vol. 115, no. 13, p. 131 102, 2019.
- [20] V. Kovanis, “Instabilities and chaos in semiconductor lasers with optical injection,” in *LEOS 95. IEEE Lasers and Electro-Optics Society 1995 Annual Meeting. 8th Annual Meeting. Conference Proceedings*, IEEE.
- [21] G. P. Agrawal and N. K. Dutta, *Semiconductor lasers*. Springer US, 1995.
- [22] M. Teimourpour, “Quantum inspired symmetries in laser engineering,” Master’s thesis, Jan. 2017.
- [23] S. O. Kasap, *Optoelectronics and photonics: Principles and practices*. Pearson, 2001, ISBN: 0201610876.
- [24] D. E. McCumber, “Intensity fluctuations in the output of cw laser oscillators. i,” *Physical Review*, vol. 141, no. 1, pp. 306–322, 1966.
- [25] A. Uchida, *Optical communication with chaotic lasers: Applications of nonlinear dynamics and synchronization*. Wiley-VCH, 2012, ISBN: 9783527408696.

- [26] F. Rana, *Semiconductor optoelectronics*, <https://courses.cit.cornell.edu/ece533/Lectures/handout11>.
- [27] R. Paschotta, *Relaxation oscillations*, Encyclopedia of Laser Physics and Technology, Oct. 2008.
- [28] C. Henry, “Theory of the linewidth of semiconductor lasers,” *IEEE Journal of Quantum Electronics*, vol. 18, no. 2, pp. 259–264, 1982.
- [29] G. Giuliani, “The linewidth enhancement factor of semiconductor lasers: Usefulness, limitations, and measurements,” in *2010 IEEE Photonic Society’s 23rd Annual Meeting*, IEEE, 2010.
- [30] J. Marcianti and G. Agrawal, “Nonlinear mechanisms of filamentation in broad-area semiconductor lasers,” *IEEE Journal of Quantum Electronics*, vol. 32, no. 4, pp. 590–596, 1996.
- [31] M. Lax, “Classical noise. v. noise in self-sustained oscillators,” *Physical Review*, vol. 160, no. 2, pp. 290–307, 1967.
- [32] H. Haug and H. Haken, “Theory of noise in semiconductor laser emission,” *Zeitschrift für Physik A Hadrons and nuclei*, vol. 204, no. 3, pp. 262–275, 1967.
- [33] M. Osinski and J. Buus, “Linewidth broadening factor in semiconductor lasers—an overview,” *IEEE Journal of Quantum Electronics*, vol. 23, no. 1, pp. 9–29, 1987.
- [34] A. L. Schawlow and C. H. Townes, “Infrared and optical masers,” *Physical Review*, vol. 112, no. 6, pp. 1940–1949, 1958.
- [35] H. Su, L. Zhang, A. L. Gray, R. Wang, P. M. Varangis, and L. F. Lester, “Gain compression coefficient and above-threshold linewidth enhancement factor in InAs/GaAs quantum DFB lasers,” in *Physics and Simulation of Optoelectronic Devices XIII*, M. Osinski, F. Henneberger, and H. Amano, Eds., SPIE, 2005.
- [36] M. Willatzen, A. Uskov, J. Mork, H. Olesen, B. Tromborg, and A.-P. Jauho, “Nonlinear gain suppression in semiconductor lasers due to carrier heating,” *IEEE Photonics Technology Letters*, vol. 3, no. 7, pp. 606–609, 1991.
- [37] J. Huang and L. W. Casperson, “Gain and saturation in semiconductor lasers,” *Optical and Quantum Electronics*, vol. 25, no. 6, pp. 369–390, 1993.
- [38] A. Markus, J. X. Chen, O. Gauthier-Lafaye, J. Provost, C. Paranthoen, and A. Fiore, “Impact of intraband relaxation on the performance of a quantum-dot laser,” *IEEE Journal of Selected Topics in Quantum Electronics*, vol. 9, no. 5, pp. 1308–1314, 2003.

- [39] *Fabry perot laser vs distributed feedback laser-difference between fabry perot laser and distributed feedback laser*, <https://www.rfwireless-world.com/Terminology/Fabry-Perot-Laser-vs-Distributed-Feedback-Laser.html>, 2012.
- [40] H. Kogelnik and C. V. Shank, "Coupled-wave theory of distributed feedback lasers," *Journal of Applied Physics*, vol. 43, no. 5, pp. 2327–2335, 1972.
- [41] M. Nakamura, K. Aiki, J. ichi Umeda, A. Yariv, H. W. Yen, and T. Morikawa, "GaAs-gal-xAlxAs double-heterostructure distributed-feedback diode lasers," *Applied Physics Letters*, vol. 25, no. 9, pp. 487–488, 1974.
- [42] K. Aiki, M. Nakamura, and J. Umeda, "A frequency-multiplexing light source with monolithically integrated distributed-feedback diode lasers," *IEEE Journal of Quantum Electronics*, vol. 13, no. 4, pp. 220–223, 1977.
- [43] D. Schuöcker, Ed., *Handbook of the eurolaser academy*. Springer US, 1998.
- [44] G. Morthier and P Vankwikelberge, "Handbook of distributed feedback laser diodes," in *Artech House 1997*, 1997, ISBN: 0-89006-607-8, MAY 1997, PP. 307 pages.
- [45] J.-M. Liu, "Semiconductor lasers and light-emitting diodes," in *Photonic Devices*, Cambridge University Press, pp. 816–925.
- [46] W. Streifer, R. Burnham, and D. Scifres, "Effect of external reflectors on longitudinal modes of distributed feedback lasers," *IEEE Journal of Quantum Electronics*, vol. 11, no. 4, pp. 154–161, 1975.
- [47] L. Coldren, G. Fish, Y. Akulova, J. Barton, L. Johansson, and C. Coldren, "Tunable semiconductor lasers: A tutorial," *Journal of Lightwave Technology*, vol. 22, no. 1, pp. 193–202, 2004.
- [48] J. Buus, M.-C. Amann, and D. J. Blumenthal, *Tunable laser diodes and related optical sources*. Wiley-IEEE Press, 2005, ISBN: 9780471208167.
- [49] H. J. R. Dutton, "Understanding optical communications," IBM, Tech. Rep., Sep. 1998.
- [50] H. Debrégeas, "Widely tunable laser diodes," in *Springer Series in Optical Sciences*, Springer International Publishing, 2017, pp. 209–248.
- [51] G. Fish and K. Affolter, "Optical communications: Tunable lasers and their impact on optical networks," Sep. 2001.
- [52] K. Kobayashi and I. Mito, "Single frequency and tunable laser diodes," *Journal of Lightwave Technology*, vol. 6, no. 11, pp. 1623–1633, 1988.

- [53] “Tunable monolithic semiconductor diode lasers,” in *Tunable External Cavity Diode Lasers*, WORLD SCIENTIFIC, 2004, pp. 29–61.
- [54] V. Jayaraman, A. Mathur, L. Coldren, and P. Dapkus, “Extended tuning range in sampled grating DBR lasers,” *IEEE Photonics Technology Letters*, vol. 5, no. 5, pp. 489–491, 1993.
- [55] M. C. Larson, “Narrow linewidth tunable dbr lasers,” *2016 International Semiconductor Laser Conference (ISLC)*, pp. 1–2, 2016.
- [56] S. Matsuo and T. Segawa, “Microring-resonator-based widely tunable lasers,” *IEEE Journal of Selected Topics in Quantum Electronics*, vol. 15, no. 3, pp. 545–554, 2009.
- [57] A. Gallet, “Hybrid III-V/Si lasers for optical communications,” PhD thesis, Université Paris-Saclay, 2018.
- [58] A. L. Liepvre, C. Jany, A. Accard, M. Lamponi, F. Poingt, D. Make, F. Lelarge, J.-M. Fedeli, S. Messaoudene, D. Bordel, and G.-H. Duan, “Widely wavelength tunable hybrid III–V/silicon laser with 45 nm tuning range fabricated using a wafer bonding technique,” in *The 9th International Conference on Group IV Photonics (GFP)*, IEEE, 2012.
- [59] X. Pommarede, “Hybrid III-V/Si photonic integrated circuits for optical communication applications,” PhD thesis, Université Paris-Saclay, May 2017.
- [60] L. Chrostowski and M. Hochberg, *Silicon photonics design*. Cambridge University Press, 2015.
- [61] S. Keyvaninia, G. Roelkens, D. V. Thourhout, C. Jany, M. Lamponi, A. L. Liepvre, F. Lelarge, D. Make, G.-H. Duan, D. Bordel, and J.-M. Fedeli, “Demonstration of a heterogeneously integrated III-V/SOI single wavelength tunable laser,” *Optics Express*, vol. 21, no. 3, p. 3784, 2013.

### CHAPTER 3

### OPTICAL FEEDBACK

Optical feedback is when portion of the optical output is back reflected into the gain medium as illustrated in fig. 3.1. This phenomenon can originate from a simple external connection and in the case of hybrid Si lasers from multiple sources such as active and passive transitions, regrowth interfaces and sometimes from process imperfections. Parasitic reflections can also emanate from other inhomogeneities in the system such as experimental set-up, fiber-coupled modules and radiation from other sources. The impact of optical feedback on SCLs has been intensively studied since the early 1970s [1, 2, 3] and continues to be an active field of research because of the significant consequences undesired short cavity reflections can cause on their performance and dynamic properties.

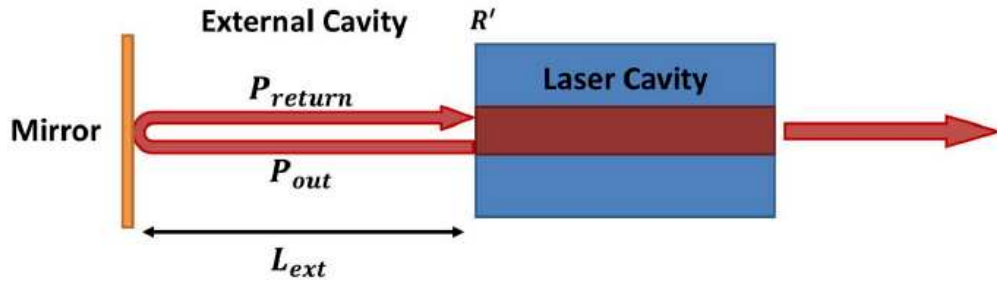


Figure 3.1: Semiconductor laser subject to optical feedback [4].

The distance of the laser to the mirror  $L_{ext}$  is related to the external round-trip time  $\tau_{ext}$  in external cavity that is defined as:

$$\tau_{ext} = \frac{2n_{ext}L_{ext}}{c} \quad (3.1)$$

where  $n_{ext}$  is the refractive index of the external cavity and  $c$  the speed of light in vacuum. In practice, the reflectivity of the re-injecting facet  $R'$  may not be zero, so that the returning

light can be bounced onto multiple round-trips within the external cavity. Such configuration can become a critical issue in the case of short external cavities, as the beam's path is equivalently multiplied. The feedback strength,  $r_{ext}$  represents the fraction of emitted power coupled back to the laser and is defined as the ratio between the output power,  $P_{out}$  from the laser facet subject to the optical feedback to the returned power  $P_{return}$  such as:

$$r_{ext} = \frac{P_{return}}{P_{out}} \quad (3.2)$$

There has been a considerable amount of interest in the spectral characteristics of the emission of a laser under external optical feedback, including the introduction of external cavity disperse elements [5]. Optical feedback can often be disadvantageous as it can cause consequential irregularities and unwanted instabilities in the laser output including deterministic chaos (i.e., coherence collapse) [6]. In fact, a great amount of time and effort is spent on investigating different alternatives to suppress or eliminate sources of optical feedback [7]. However, from the fundamental physics point of view, intentionally implemented feedback can also serve as an attribute to enhance several performance characteristics of the device to include increased output power, threshold reduction, decreased linewidth, and modulation bandwidth improvement. In addition, this deterministic chaos can also be used as a vehicle to perform random number generation and to carry out secure communications, which is in fact part of the motivation the work presented in this manuscript was conducted. Chapter IV provides additional information substantiated by experimental results demonstrating that a combination of optical feedback can be used for chaos bandwidth enhancements. This data helps us to better understand the perturbations generated by optical feedback on hybrid III-V on Si SCLs and determine how this phenomenon can be further investigated to augment existing applications and identify future uses such as the development of isolator-free integrated photonics.

Multiple experiments conducted throughout the years have demonstrated the impact returned light into the cavity of a laser has on its performance properties [8]. According

to the Poincaré-Bendison theorem, a dynamical system requires at least three degrees of freedom in order to become destabilized and exhibit deterministic chaos [9]. The three rate equations that govern the properties of a laser [10] are given by:

$$\frac{dN}{dt} = f(N, E, P) \quad (3.3)$$

$$\frac{dE}{dt} = g(N, E, P) \quad (3.4)$$

$$\frac{dP}{dt} = h(N, E, P) \quad (3.5)$$

where  $N$  is the carrier density,  $E$  the electric field and  $P$  the polarization. *Arecchi et al.* [11] proposed a laser classification based on the photon, carrier and polarization lifetimes,  $\tau_p$ ,  $\tau_c$  and  $\tau_{pol}$  respectively. The solutions to Equations (3.3) to (3.5) explain the variety of influences external feedback can exert on the laser characteristics. In SCLs, the polarization responds rapidly to the changes in the carrier density or electrical field; the third equation governing the polarization can be replaced by its steady-state solution. With only two degrees of freedom, the laser can not become unstable, therefore; an additional degree of freedom induced by an external mechanism such as optical injection or optical feedback is then required.

### 3.1 Optical Feedback Effects on the Optical Spectrum of a Laser Diode

The first observation of optical feedback impact on a LD was related to the feedback induced evolution of the optical spectrum. Depending on the feedback conditions (e.g., external cavity length, feedback strength), the spectrum can either become single-mode with a narrow linewidth as described in [12], (where the linewidth decreases from 6 MHz down to 30 kHz), or become strongly multimode [13]. In 1986, Tkach and Chraplyvy [14] carried-out a systematic experimental study that resulted in the cartography of a DFB QW laser

when subject to optical feedback as illustrated in fig. 3.2. This figure represents the spectral behavior of the laser as a function of two feedback parameters: the feedback strength and the external cavity length.

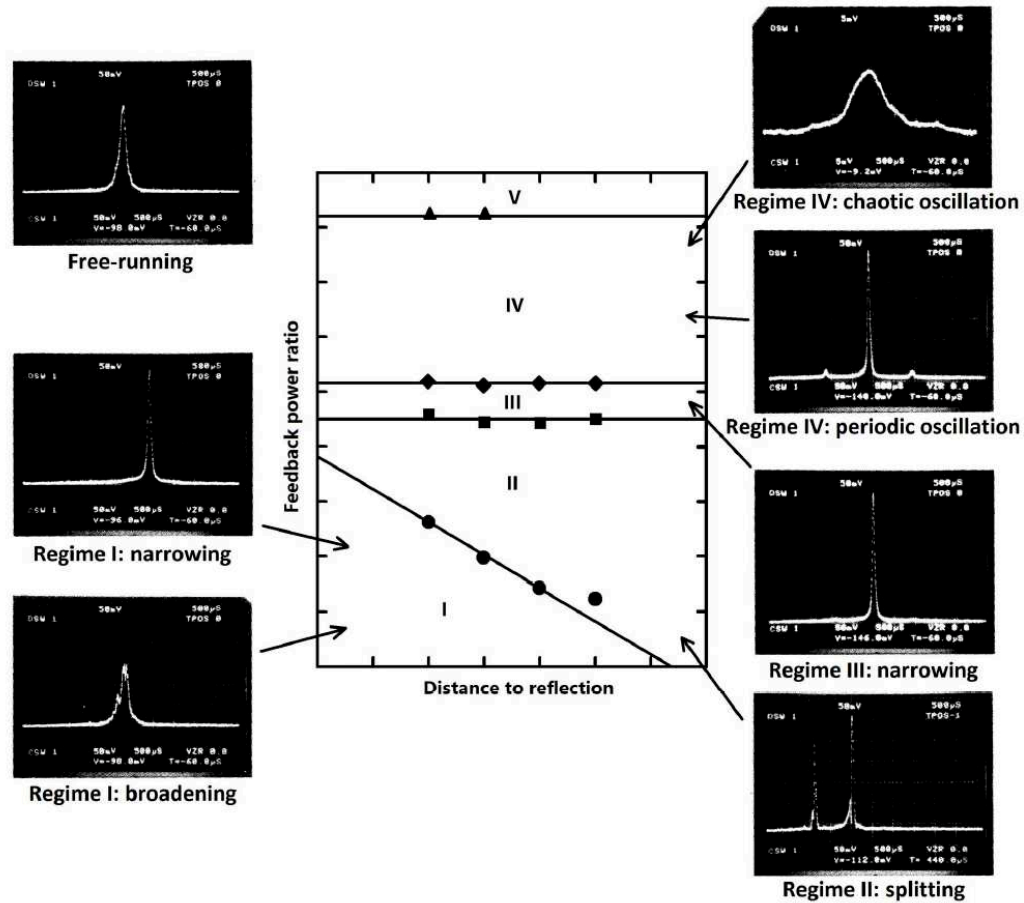


Figure 3.2: Cartography of optical feedback regimes in a DFB laser as a function of the external cavity length and the feedback strength [14]. The optical spectra on both sides illustrate the laser dynamics under optical feedback [15].

The dominant parameters driving the laser's dynamics under optical feedback are the external time delay  $\tau_{ext}$  and the feedback strength  $r_{ext}$ . Fig. 3.2 displays the five different feedback regimes of a SCL as a function of the external cavity length and the feedback strength when operating under external optical feedback. It also illustrates the evolution of the optical spectrum and the dynamics variation of the device. This cartography has served as a milestone reference for many scientists describing the effects of optical feedback in SCLs. The graph has been revisited numerous times [16] to extend the classification of

feedback to short and long external cavities when addressing sub-regimes of the CC [16] and incoherent interactions and it has also been complemented based on desired applications to address the small cavity regime [17], defined when  $r_{ext}\tau_{ext} < 1$ .

Regime I is a stable and single-mode regime where the laser linewidth and the output power depend on the feedback phase. Here, the laser spectrum demonstrates that the laser linewidth can be narrowed or broadened based on the distance to the reflector. Regime II is characterized by a bistability, the larger the distance to the feedback reflector, the more sensitive the laser is to the lower levels of feedback. In this regime, the laser remains single-mode but jumps around due to the changes associated with the phase of the laser spectrum that lead to mode hopping of the spectrum. In the optical spectra, two modes appear simultaneously, which corresponds to the external cavity modes (ECM) between the laser output facet and the feedback reflector with frequencies multiples of  $c/2n_{ext}L_{ext}$ . The amplitudes between the two peaks depend on the feedback phase. A further increase in the feedback strength leads the laser into the third regime, where the length of the reflector and the optical phase are inconsequential. Regime III provides stable and single mode operation with linewidth reduction. After this, the laser then enters Regime IV, where the device experiences unstable operation with CC causing a drastic decrease of the coherence length and a significant linewidth broadening to several tens of GHz with severe peaks. In this regime, the laser spectrum develops enhanced side modes separated by the main lasing mode due to the relaxation oscillation frequency (ROF) denoted by  $f_r$ . In this case, the laser is insensitive to changes in the feedback phase. This route to chaos is commonly observed in SCLs with optical feedback where two frequencies with incommensurable ratio namely the ROF and the external cavity frequencies interact with each other and result in the quasi-periodicity route to chaos as the feedback strength increases. The onset of this regime is also referred to as the critical level, denoted by  $r_{crit}$  and can be analytically estimated as [18]:

$$r_{crit} = \gamma^2 \frac{\tau_{int}^2}{16C_l^2} \frac{1 + \alpha_H^2}{\alpha_H^4} \quad (3.6)$$

where  $\gamma$  is the damping factor associated with the ROF,  $\tau_{int} = 2n_{int}L_c/c$  the internal round trip time where  $n_{int}$  and  $L_c$  are the refractive index and the cavity length of the laser, respectively;  $C_l$  the external coupling coefficient from the facet to the external cavity (Equation 3.12) and  $\alpha_H$  the linewidth enhancement factor.

Last but not least, fig. 3.2 shows that for very high feedback strengths, the laser re-enters stable operation with a notable linewidth reduction and very high power. It is important to point out and emphasize that in order to achieve high enough feedback strengths, an anti-reflection coating on the laser output facet must be added. This regime corresponds to the extended cavity regime where the laser operates as a small gain medium in a long cavity. The back facet of the laser and the feedback reflector serve as cavity mirrors, where sufficient wavelength selectivity allows the laser to operate in a single longitudinal mode with narrow linewidth for all phases of feedback [19, 20, 21].

## 3.2 Analytical Approach of Optical Feedback

### 3.2.1 Rate Equations of a Laser Diode under Optical Feedback

The formalism of SCLs under optical feedback was first proposed by LK [1] in 1981 when the rate equation model was proposed for a single-mode laser, describing the evolution of the carriers and complex optical field. Over time, extensive research has been successfully carried out and promising results have been well-documented as the basis to further investigate the uncertain impact of optical feedback on a LD while improving the LK models. In their study only one round trip in the external cavity is considered, which suggests a relatively small amount of feedback. If  $E$  is the slowly varying envelope of the complex electric field and  $N$  the carrier density of the upper laser state, the rate equations for a solitary LD can be expressed as

$$\frac{dN}{dt} = \frac{I}{q} - \frac{N}{\tau_c} - G(N) |E|^2 \quad (3.7)$$

$$\frac{dE}{dt} = \frac{1 + i\alpha_H}{2} [G(N) - \frac{1}{\tau_p}] E \quad (3.8)$$

where  $G(N) = 1/\tau_p + G_N(N - N_{th})$  the gain per unit time,  $|E|^2$  the normalized complex amplitude (which corresponds to the number of photons inside the cavity) and  $\omega_0$  the angular optical frequency of the solitary device (i.e. without optical feedback). The solitary device is assumed to oscillate in a single longitudinal mode. The LK models included the influence of the optical feedback by considering the interference of the laser field with its own coherence delayed field that had propagated once through the external cavity [1, 22]. These equations have become the paradigm for investigating the dynamical behavior of LDs when subject to optical feedback [23]. Therefore, the rate equations of the laser subject to optical feedback can then be expressed as:

$$\frac{dN}{dt} = \frac{I}{q} - \frac{N}{\tau_c} - G(N) |E|^2 \quad (3.9)$$

$$\frac{dE}{dt} = \frac{1 + i\alpha_H}{2} [G(N) - \frac{1}{\tau_p}] E + \kappa E(t - \tau_{ext}) e^{-i\omega_0 \tau_{ext}} \quad (3.10)$$

The feedback appears in the last term of Equation (3.10), where external field,  $\mathcal{E} = E(t) e^{i\omega_0 \tau_{ext}}$  is incident on the facet subject to the re-injection with an amplitude coefficient  $E(t)$  for an electromagnetic field entering the laser where  $e^{i\omega_0 \tau_{ext}}$  is the fast lasing oscillations. The feedback coefficient  $\kappa$  is defined as:

$$\kappa = \frac{1}{\tau_{in}} 2C_l \sqrt{r_{ext}} \quad (3.11)$$

where  $C_l$ , the external coupling coefficient for a FP cavity, which represents the fractional amount of coupled field into the device is given by

$$C_l = \frac{1 - R_2}{2\sqrt{R_2}} \quad (3.12)$$

with  $R_2$  the reflection coefficient of the laser front facet subject to the re-injection. In the case of a DFB laser, the expression of  $C_l$  becomes much more complex and depends on the complex reflectivity at both laser facets [24]:

$$C_l = \frac{2(1 - |\rho_l|^2)e^{-i\varphi_l}(q^2 + k^2)L^2}{i\kappa L(1 + \rho_l^2) - 2\rho_l q L} \frac{1}{2qL - \sum_{k=l,r} \frac{(1 - \rho_k^2)\kappa L}{2iqL\rho_k + kL(1 + \rho_k^2)}} \quad (3.13)$$

In this equation,  $\rho_k = |\rho| e^{i\varphi_k}$  where  $k = l, r$ , is the complex reflectivity at the left or right facet, respectively (the right facet being the one towards the external cavity).  $L$  is the laser length,  $k$  the grating coupling coefficient of the DFB grating and  $q$  can be expressed as  $q = \alpha_{tot} + i\delta_0$  where  $\alpha_{tot}$  is the total internal losses and  $\delta_0$  the Bragg detuning, defined as the deviation between the lasing and the Bragg wavenumbers.

Now that the rate equations for the slowly varying envelope of the complex amplitude have been considered, the dynamics of the photon number  $S$  and the phase  $\phi$  must be considered also. By writing  $E = \sqrt{S}e^{i\phi}$ , the two rate equations can be deduced from Equation (3.10) for the photon density and phase of the electric field respectively:

$$\frac{dS}{dt} = \left(G(N) - \frac{1}{\tau_p}\right)S + 2\kappa\sqrt{S(t - \tau_{ext})}\sqrt{S(t)}\cos(\omega_0\tau_{ext} + \phi(t) - \phi(t - \tau_{ext})) \quad (3.14)$$

$$\frac{d\phi}{dt} = \frac{\alpha_H}{2}\left(G(N) - \frac{1}{\tau_p}\right) - \kappa\frac{\sqrt{S(t - \tau_{ext})}}{\sqrt{S(t)}}\sin(\omega_0\tau_{ext} + \phi(t) - \phi(t - \tau_{ext})) \quad (3.15)$$

### 3.2.2 Feedback-induced Frequency Shift

Under steady-state, the photon density  $S_s$  is constant and is defined as  $S_s = S_s(t) = S_s(t - \tau_{ext})$ . Therefore, the term in the  $\cos(\omega_0\tau_{ext} + \phi_s(t) - \phi_s(t - \tau_{ext}))$  must be time insensitive and the steady-state phase  $\phi_s$  can be written without loss of generality as  $\phi_s = (\omega_s - \omega_0)t$ .

Equation (3.15) under steady conditions yields:

$$\omega_s - \omega_0 = -\kappa[\alpha_H \cos(\omega_s \tau_{ext}) + \sin(\omega_s \tau_{ext})] \quad (3.16)$$

As discussed later on, this leads to several solutions for  $\omega_s$ , that are the angular frequencies of the external cavity modes, or fixed points. Among these frequencies, the laser will tend to operate on the mode with minimum linewidth, corresponding to the best phase stability [25].

### 3.2.3 Threshold Reduction

The steady-state equation resulting from Equation (3.14) yields:

$$G(N) - \frac{1}{\tau_p} + 2\kappa \cos(\omega_s \tau_{ext}) = 0 \quad (3.17)$$

where  $\omega_s$  is the solution of Equation (3.16) that has minimum linewidth. This means optical feedback has an influence on the threshold gain and therefore; on the threshold current of the laser, compared to the free-running state. The impact of the optical feedback on the threshold reduction is demonstrated in fig. 3.3.

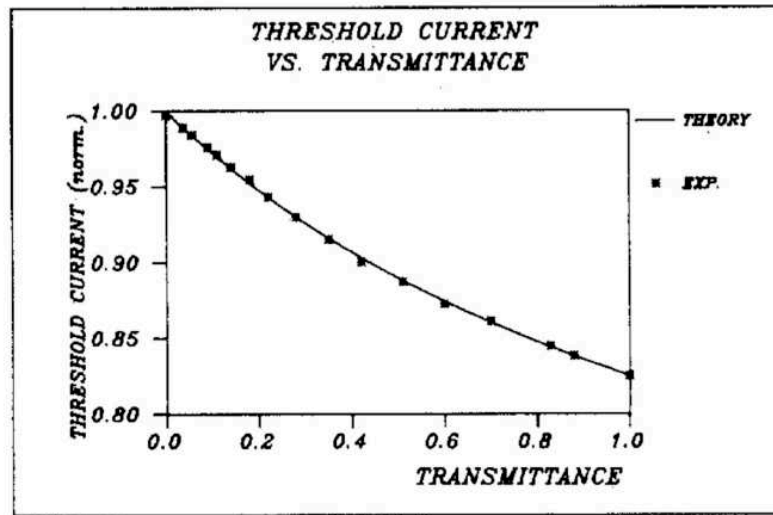


Figure 3.3: Threshold reduction with optical feedback, experimentally and theoretically. The transmittance in  $x$ -axis is proportional to the feedback strength [26].

Osmundsen and Gade [26] derived the expression of the threshold current by considering multiple round trips in the external cavity. In the limit case of small feedback strengths, ( $r_{ext} \ll 1$ ), the threshold current  $I_{th}$  can be expressed as:

$$I_{th} = I_o(1 - 2\kappa \cos(\omega_s \tau_{ext})) \quad (3.18)$$

This equation fits very well the experimental results shown in fig. 3.3

### 3.2.4 Linewidth Evolution

The linewidth of a semiconductor laser is due to the existence of spontaneous emission and the phase-amplitude coupling, leading to phase fluctuations that result in frequency noise [27]. In order to characterize the linewidth of a SCL, Langevin noise forces,  $F_N$ ,  $F_S$  and  $F_\phi$  must be added to the rate equations (3.9), (3.14) and (3.15) [28] to take the stochastic fluctuations arising from the laser's noise into account in addition to the spontaneous emission rate  $R_{sp}$ . By defining the phase fluctuation as  $\Delta\phi = \phi(t) - \phi(t - \tau_{ext}) + \omega_0\tau_{ext}$ , the rate equations can then be expressed as:

$$\frac{dN}{dt} = \frac{I}{q} - \frac{N}{\tau_c} - G(N)S + F_N(t) \quad (3.19)$$

$$\frac{dS}{dt} = (G(N) - \frac{1}{\tau_p})S + R_{sp} + 2\kappa\sqrt{S(t - \tau_{ext})S(t)} \cos(\Delta\phi) + F_s(t) \quad (3.20)$$

$$\frac{d\phi}{dt} = \frac{\alpha_H}{2}(G(N) - \frac{1}{\tau_p}) - \kappa\sqrt{\frac{S(t - \tau_{ext})}{S(t)}} \sin(\Delta\phi) + F_\phi(t) \quad (3.21)$$

where we consider the photon number  $S$  and the phase  $\phi$  instead of the complex electric field  $E$ .  $F_s(t)$  refers to the role of spontaneous emission, that is the amplitude and phase of the modal field are randomly perturbed by each spontaneously emitted photon that contributes to the mode. On the other hand,  $F_N(t)$  arises from the discrete nature of the carrier generation and recombination process but has little impact on the laser dynamics compared

to the spontaneous emission noise [23]. These rate equations can be solved by considering a small fluctuation around the steady results and assuming slow variations of the phase and intensity of the electric field.

Considering the power spectrum this leads to [27]:

$$\Delta v = \frac{\Delta v_o}{[1 + \kappa\tau_{ext}\sqrt{1 + \alpha_H^2} \cos(\omega_s\tau_{ext} + \tan^{-1}(\alpha_H))]}^2 \quad (3.22)$$

where  $\Delta v_o$  is the linewidth of the free-running laser [29]:

$$\Delta v_o = \frac{(1 + \alpha_H^2)v_g^2\hbar v_o G n_{sp}\alpha_m}{8\pi P_{opt}} \quad (3.23)$$

where  $v_g$  is the group velocity;  $\hbar$  the Planck's constant;  $v$  the emission frequency;  $G$  the gain;  $n_{sp} = R_{sp}/v_g G$  the spontaneous emission factor and  $P_{opt}$  the optical power.

Schunk and Petermann [30] linked the phase condition (3.16) and the linewidth Equation (3.22) to the different feedback regimes observed experimentally on the optical spectra as described earlier in this chapter. By defining a feedback parameter  $C = \kappa\tau_{ext}\sqrt{1 + \alpha_H^2}$ , they redefined the first regime as the regime where Equation (3.15) has only one solution, i.e. the case  $C < 1$ . Fig. 3.4, illustrates the impact of optical feedback on the laser's linewidth as it is scanned from Regime I-IV. This figure depicts the variation of the linewidth created by the feedback phase. The assumed parameters for fig. 3.4 are  $\tau_{ext} = 5$  ns,  $\tau_L = 9$  ps,  $R_2 = 0.32$ ,  $\alpha_H = 6$  and 5 mW/facet out. It is shown that for the given output power of 5 mW and 5 ns delay, the linewidth can however; vary depending on the initial phase  $\omega_0\tau_{ext}$ . The second regime appears for  $C > 1$ , where the phase condition (3.14) has several solutions. The solutions of Equation (3.16), that gives the laser wavelength as a function of the feedback parameters, lie on an ellipse in the  $\Delta G - \Delta\omega$  space, with  $\Delta\omega = \omega_s - \omega_0 = -k [\alpha_H \cos(\omega_s\tau_{ext}) + \sin(\omega_s\tau_{ext})]$  and  $\Delta G = G_N - 2k \cos(\omega_s\tau_{ext})$ , the gain change induced by optical feedback [31] is given by:

$$(2\Delta\omega - \alpha_H\Delta G)^2 + (\Delta G)^2 = 4k^2 \quad (3.24)$$

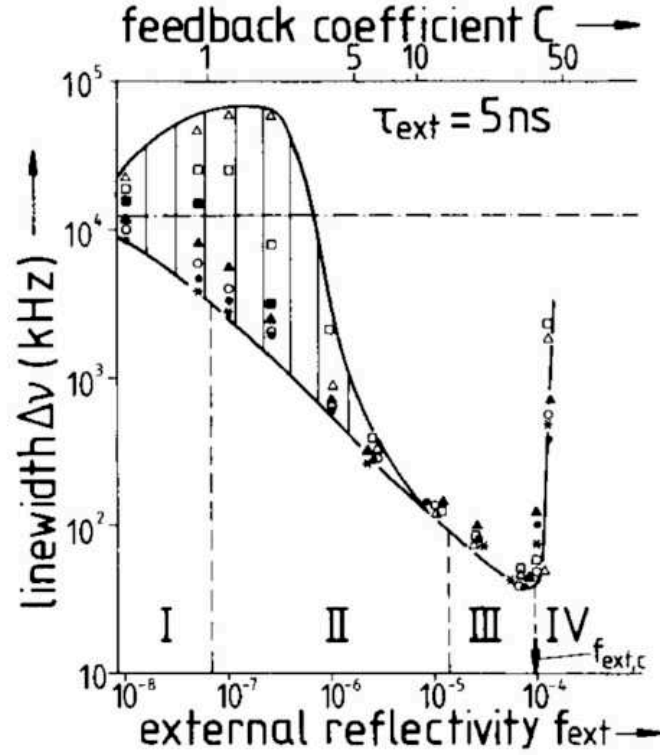


Figure 3.4: Evolution of the laser linewidth as a function of the feedback strength, for several initial phase conditions [32]. The roman numerals I-IV corresponds to the regimes given in fig 3.2.

The stable solutions are the modes of the external cavity (fixed points) and are located on the lower half of the ellipse (blue circles in fig. 3.5), whereas the unstable solutions, called antimodes, appear on the upper half of the ellipse (red circles in fig. 3.5).

Levine *et al.* [34] proved that, although the most stable mode is the mode with maximum gain (also the mode with minimum threshold, corresponding to the external cavity mode closest to lowest point of the ellipse given by  $\omega_s\tau_{ext} = 0$ ), the laser subject to optical feedback will tend to stabilize on the mode with minimum linewidth, which is the closer one to the free-running state, as illustrated in fig. 3.5 which corresponds to the third feedback regime. However, these two modes will enter in competition and then the CC regime occurs.

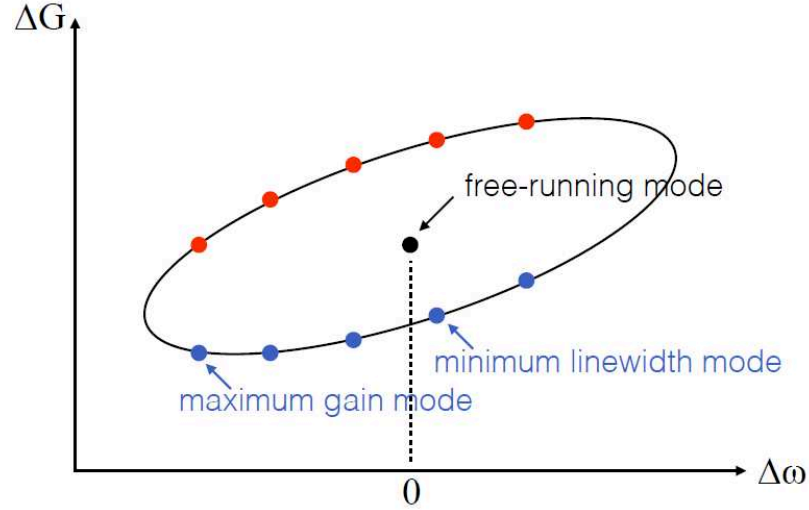


Figure 3.5: Ellipse of the feedback modes and anti-modes. In blue circles, stable external cavity modes, and in red circles, unstable anti-modes [33].

The term CC was introduced by Lenstra *et al.* [35], by realizing that the feedback terms in Equations (3.20) and (3.21) were interfering in the case of relatively strong optical feedback and therefore; these equations could no longer be linearized. By considering this inter-dependence of amplitude and phase, a drastic linewidth broadening as well as a strong decrease of the coherence length compared to the free-running case can be obtained numerically, that are in agreement with the experimental results.

### 3.3 Dynamical Properties of a Laser Diode under Optical Feedback

#### 3.3.1 Dimensionless Rate Equations with Optical Feedback

The dynamics of a LD subject to optical feedback are usually studied using dimensionless parameters [36], that can be extracted from the complex rate equations (3.9) and (3.10). Then, when these rate equations are normalized, we define a new set of dimensionless variables  $(Y, Z)$ , with  $Y$  the normalized complex electric field and  $Z$  the normalized carrier density. Therefore, the normalized equations can be re-written as:

$$\frac{dY}{ds} = (1 + i\alpha)ZY + \eta e^{-i\Omega\theta}Y(s - \theta) \quad (3.25)$$

$$T \frac{dZ}{ds} = P - Z - (1 + 2Z)|Y|^2 \quad (3.26)$$

where  $\eta = k\tau_p$  is the normalized feedback coefficient;  $\Omega = \omega_o\tau_p$  the normalized free-running frequency;  $\theta = \tau_{ext}/\tau_p$  the normalized external cavity round trip time or delay;  $T = \tau_c/\tau_p$  the carrier to photon lifetime ratio and  $P$  the normalized pump current; defined as:

$$P = \frac{\tau_p a N_{th}}{2} = \left( \frac{I}{I_{th}} - 1 \right) \quad (3.27)$$

In this last equation, the threshold current  $I_{th}$  and the carrier density  $N_{th}$  are linked by  $I_{th} = N_{th}q/\tau_c$  with  $q$  being the electron charge.

Solving the equation  $|M_j - \lambda I| = 0$  as demonstrated in Chapter II leads to the eigenvalues of the perturbed system  $\lambda_{\pm} = -\Gamma_{norm} \pm \sqrt{\Gamma_{norm}^2 - \Omega^2}$  with

$$\Omega = \sqrt{\frac{2P}{T}} \quad (3.28)$$

$$\Gamma_{norm} = \frac{1 + 2P}{2T} \quad (3.29)$$

where  $\Omega$  and  $\Gamma$  are the dimensionless variables when the LD is subject to optical feedback. The unnormalized rate equations of these two parameters were derived in Chapter II from the LK equations in the absence of feedback, Equations (2.42) and (2.43).

### 3.3.2 Bifurcation Diagram Representing the Laser Dynamics

The rate equations (3.25) and (3.26) are solved by using the Runge-Kutta method (RK4). For a given set of initial conditions, including a given feedback strength, the numerical time trace of the laser under optical feedback is built by iterations. The final point of the time

trace will then be used as the initial condition for the next feedback. A bifurcation diagram [37] is then built that represents the intensity extrema, extracted from the time series when excluding the transient part of the trace, as a function of the feedback strength. Fig. 3.6(a) presents an example of such diagram, for a traditional SCL in typical operating conditions, with a carrier to photon lifetime ratio  $T = 1700$  and an  $\alpha_H = 3$ , biased at  $P = 0.5$ , and for an external cavity length of 30 cm. The diagram shows a succession of stable and unstable behaviors when increasing the feedback strength.

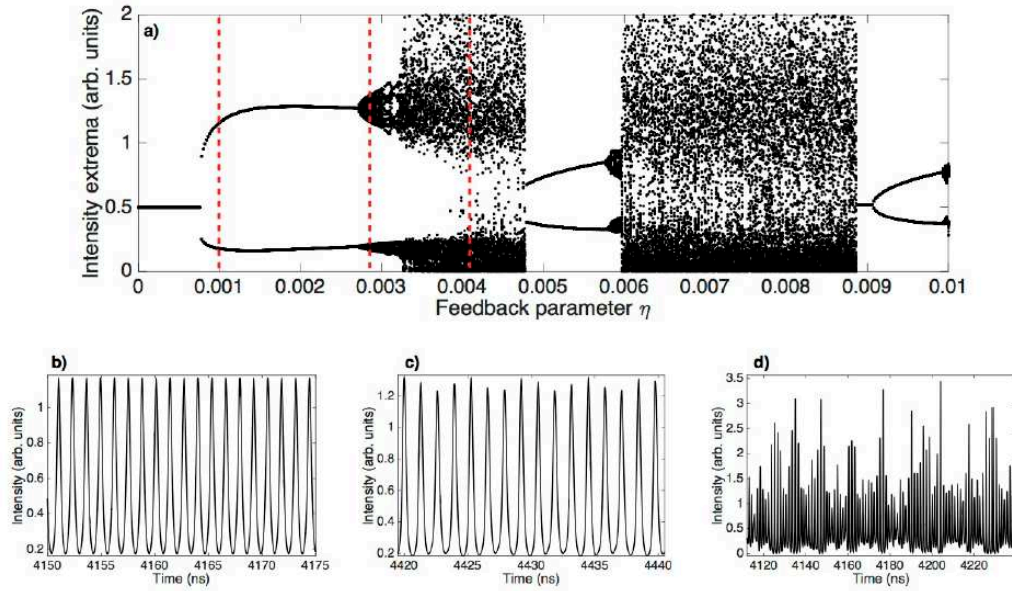


Figure 3.6: a) Numerical bifurcation diagram for  $T = 1700$ ,  $P = 0.5$ ,  $\theta = 500$  ( $L_{ext} \approx 30$  cm) and  $\alpha_H = 3$ . b) Corresponding time trace for  $\eta = 0.001$ . c) Time trace for  $\eta = 0.0027$ . d) Time trace for  $\eta = 0.0042$  [33].

For very low levels of feedback, the laser emission is stable, there is only one line on the bifurcation diagram and the only perturbation that appears on the time trace is due to noise. At a critical feedback level, here  $\eta \approx 0.0008$ , the minimum and maximum of the intensity split significantly. This particular point is called Hopf bifurcation (or Hopf point), and it corresponds to the appearance in the time trace of a periodic oscillation at the ROF as displayed in fig. 3.6(b). This regime is also called period 1 (P1). For higher feedback strengths, the diagram splits again as another oscillation frequency appears, that is superimposed on the first one as illustrated in fig. 3.6(c). More and more frequencies

are involved, until the oscillations become totally aperiodic as seen in fig. 3.6(d). These random pulsations do not correspond to noise, since they strongly depend on the initial conditions and are purely deterministic, i.e.; the pulsations can be fully anticipated by using a complete numerical model: the laser has a chaotic behavior (coherence collapse). As the feedback strength increases, the laser re-stabilizes on an external cavity mode, and the cycle starts again. Sometimes, although this was not observed in this particular example, for a very strong feedback value, the periodic oscillations occur at the external cavity frequency, but the first oscillations just after the first Hopf point always occur at the ROF. These results are consistent with experiments conducted on several SCLs [38] and with other numerical analyses presented in literature [39, 40]. The nonlinear dynamics described here is called the quasi-periodic route to chaos [41].

### 3.3.3 Influence of the Bias Current, the External Cavity Length and the $\alpha_H$ factor on the Bifurcation Diagram

The evolution of the laser dynamical behavior under optical feedback as a function of the bias current is depicted in fig. 3.7(a)-(c), corresponding to  $T = 1700$ ,  $\alpha_H = 3$ ,  $\theta = 500$  and  $P = 0.02$ ,  $P = 0.5$  and  $P = 1$  respectively. It can be seen that the first chaotic area strongly expands with the pump parameter. In addition, the feedback strength at which the first Hopf bifurcation occurs increases with the bias current. When the laser operates just above threshold, the dynamics are different from the one explained before. After the Hopf bifurcation, the laser does enter the period 1 regime and oscillates at the ROF, but the destabilization towards chaos occurs through period doubling, i.e.; the second frequency that appears is exactly twice the ROF. This dynamical regime is known as period 2 or P2. Afterwards, the period continues to double until it reaches the chaotic region [42]. Fig 3.7(d)-(f) represents the evolution of the bifurcation diagram when increasing the external cavity length, i.e.;  $\theta = 50$ ,  $\theta = 500$  and  $\theta = 1000$  respectively, at fixed  $T = 1700$ ,  $\alpha_H = 3$  and pump parameter  $P = 0.5$ .

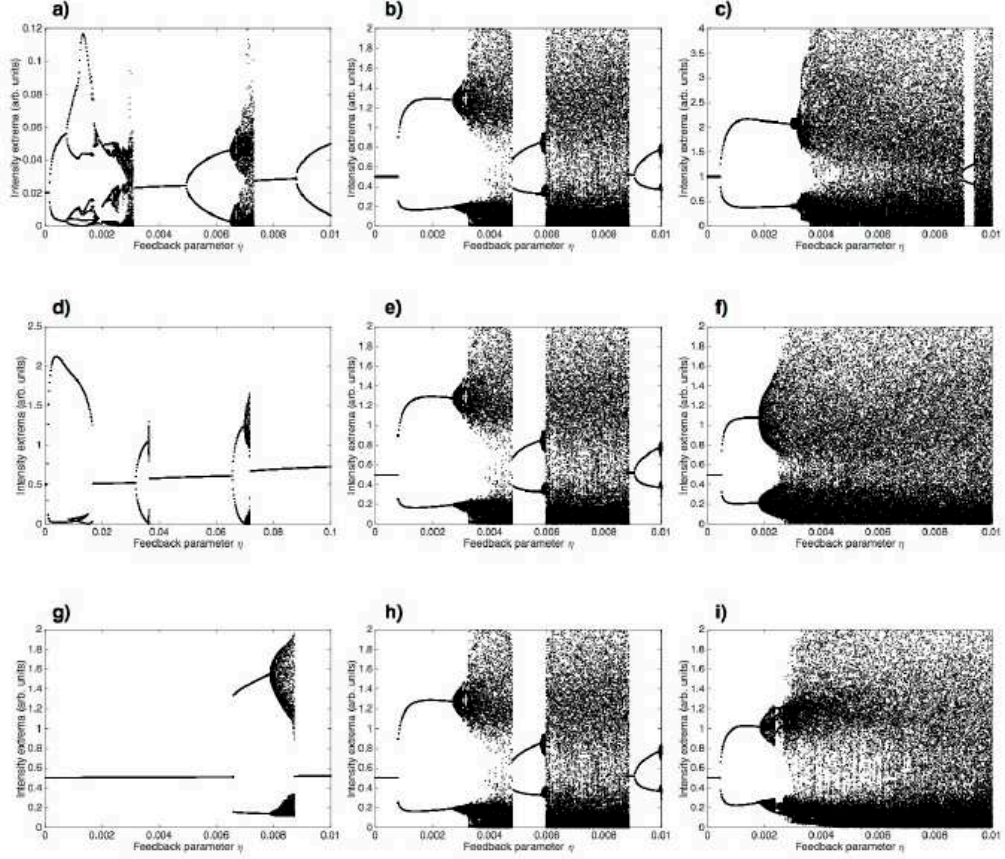


Figure 3.7: Evolution of the bifurcation diagram, calculated by increasing the feedback strength for  $T = 1700$ , as a function of the main parameters. First row: evolution with the pump current, for  $\alpha_H = 3$  and  $\theta = 500$ . a)  $P = 0.02$ . b)  $P = 0.5$ . c)  $P = 1$ . Second row: evolution with the external cavity length, for  $\alpha_H = 3$  and  $P = 0.5$ . d)  $\theta = 50$  ( $L_{ext} \approx 3$  cm).  $\theta = 500$  ( $L_{ext} \approx 30$  cm). f)  $\theta = 1000$  ( $L_{ext} \approx 60$  cm). Third row: evolution with the  $\alpha_H$ -factor, for  $P = 0.5$  and  $\theta = 500$ . g)  $\alpha_H = 1$ . h)  $\alpha_H = 3$ . i)  $\alpha_H = 5$  [33].

The position of the first Hopf point does not change significantly with the external cavity length, which is in agreement with the cartography of optical feedback (fig. 3.2). However, the extent of the chaotic zone increases significantly with the external cavity length. For the shortest cavity in this example, the time trace remains much longer in period 1, and the chaos occurs only at very high feedback strengths (note the larger  $x$ -scale of fig. 3.7(d) compared to the others). The limit case, as observed in the literature, is the disappearance of chaos for ultra-short cavities [43, 44, 45]. This occurs in the short-cavity regime, i.e.; when the  $f_r \tau_{ext} < 1$ , where  $f_r$  is the ROF. Finally, fig. 3.7(g)-(i) show the influence of the

$\alpha_H$  factor on the bifurcation diagram, with  $\alpha_H = 1$ ,  $\alpha_H = 3$  and  $\alpha_H = 5$  respectively, which correspond to typical values for LDs, at given  $T = 1700$ ,  $P = 0.5$  and  $\theta = 500$ . Increasing the  $\alpha_H$  results in decreasing the feedback strength at which the first Hopf bifurcation occurs as well as expanding the chaotic area. Furthermore, for very small  $\alpha_H$  values, the shape of the Hopf bifurcation differs significantly from the higher  $\alpha_H$  case [46]. When the bifurcation occurs on an external cavity antinode, this is called subcritical Hopf bifurcation. Supercritical Hopf bifurcations are the most common scenario in interband lasers under optical feedback, and correspond to bifurcations leading to stable periodic solutions, whereas subcritical bifurcations lead to unstable periodic solutions, and occur mainly in the short-cavity regime [46]. For LDs with extremely low  $\alpha_H$ , no chaos appears, and the dynamics correspond to a cascade of supercritical and subcritical Hopf bifurcations.

It is important to highlight that, contrary to the two previous parameters, the  $\alpha_H$  is not a degree of freedom during the experiment. However, the analysis of the influence of this parameter on the bifurcation diagram allows explaining the difference in behavior that has been observed from one structure to another when subject to optical feedback.

### 3.3.4 Phase Diagrams

Another representation of the laser dynamics consists in plotting the phase diagrams, corresponding to the carrier number versus optical power curves. When the emitted power remains constant that is when the laser is under steady-state, the device operates on an external cavity mode at an angular frequency  $\omega_s$  and it is represented as a single point on the first curve of fig. 3.8. Fig. 3.8(a) represents period 1 operation and the phase diagram is a circle around the steady-state point. Period 2 corresponds to the appearance of a second circle of different radius as shown in fig. 3.8(b), whereas chaos fig. 3.8(c) involves many frequencies, represented on the phase diagram by multiple concentric trajectories of various radii. All these phase diagrams are centered on the steady-state point. Therefore, the external cavity modes are also called fixed points, or attractors.

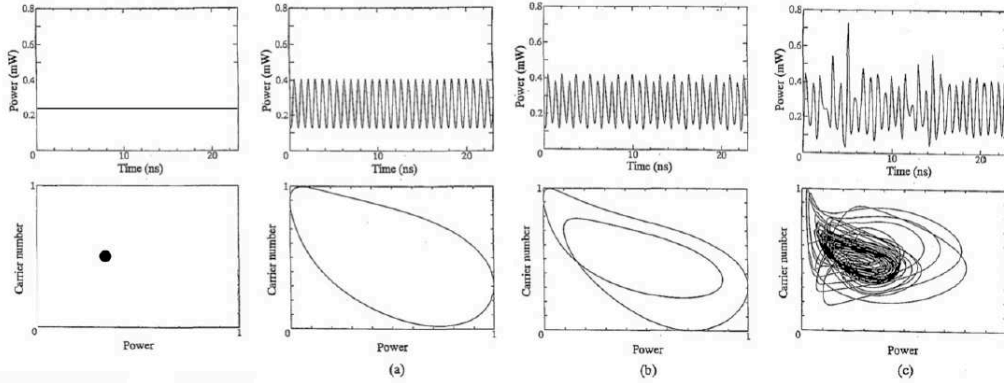


Figure 3.8: Numerical time traces and associated phase diagrams [47].

### 3.3.5 Coherence Collapse and Chaos

The chaos predicted numerically from the LK equations was also observed experimentally and was proven to coincide with the CC regime. The first hint of the appearance of chaos within the CC regime originated from the analysis of the experimental electrical spectra of a laser, which was shown to match the power spectral density derived from the numerical time traces [48]. A few years later, the time resolution of the photodiodes became sufficient to observe directly the experimental time series and experimental phase diagrams as displayed in fig. 3.9 [41].

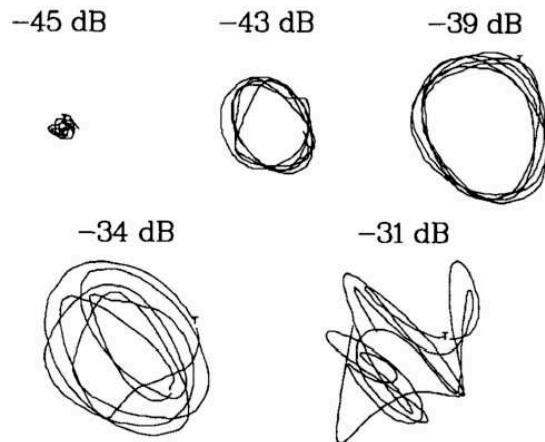


Figure 3.9: Experimental phase diagrams showing the route to chaos [41].

The two predicted routes to chaos, quasi-periodic or through period-doubling, were observed experimentally as reported in [41], the occurrence of one scenario or the other depending on the laser intrinsic characteristics and the initial conditions.

A careful sweep of the feedback strength in the experiment sometimes enables one to observe the whole route to chaos on the optical spectra, as shown in fig. 3.10 from measurements performed at Telecom ParisTech on a DFB QW laser [33].

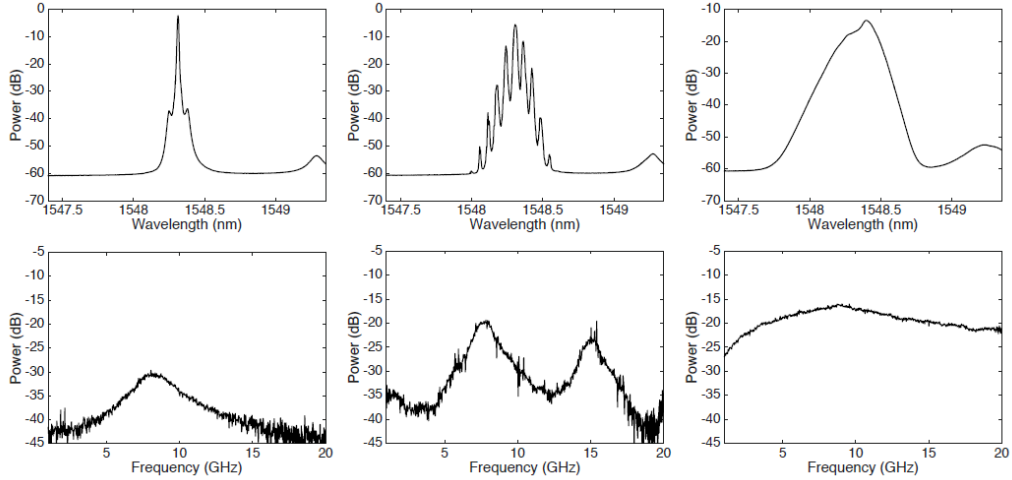


Figure 3.10: Optical and electrical spectra of a DFB quantum well laser under optical feedback, presenting the progressive appearance of coherence collapse [33].

While the optical spectrum is broadening, some peaks may appear on the spectrum corresponding to the ROF, as verified on the electrical spectrum. Then these peaks disappear, leaving a very broad spectrum both in the wavelength and frequency domains. The critical feedback level  $r_{crit}$  (Equation (3.6)) corresponding to the onset of CC, that was defined from the maximum frequency shift with respect to the free-running, it then corresponds to the occurrence of an unstable behavior in the laser, and can be considered as the maximum parasitic feedback strength that can be tolerated for stable operation.  $r_{crit}$  is derived from the laser transfer function (i.e., by looking at the instabilities from the poles, which make the transfer function diverging) after a cascade of approximations.

Another form of chaos may appear different from the aperiodic pulsations described above. This chaos is usually observed just above the solitary threshold and it takes the

form of sudden power drop-outs followed by a progressive recovery, or build-up on a time scale much larger than the period of the relaxation oscillations or the external cavity round trip. This striking phenomenon is known as the low frequency fluctuations (LFF) regime. Many efforts have been conducted to explain the origin of such power drop-outs. Henry and Kazarinov [31], followed by Mark *et al.* [49], attributed the LFF to a bistability between the mode with maximum gain and the mode with lower linewidth, and to the switching between the two modes due to noise and spontaneous emission. With this potential model, they were able to reproduce qualitatively one deterministic power drop-out and the associated recovery. However, this model can not explain the existence of more than one drop-out. The satisfying explanation was given by Sano [50] by studying the feedback ellipse representing the modes and anti-modes. During LFF, the build-up process comes from mode switching towards the mode with maximum gain. According to [14], the CC including the LFF phenomenon corresponds to the chaotic emission regime IV, in which the LFF occurs close to the transition to the stable emission regime V as demonstrated in [51]. A so-called crisis [50] occurs during the process, corresponding to a collision between a quasi-attractor, (i.e., an external cavity mode that temporarily loses its stability due to the occurrence of chaos) and the associated anti-mode. Due to the crisis, the  $\Delta G$  value will increase, and in order to restabilize, the laser frequency will shift until it meets the ellipse again on an antimode, and the stabilization then occurs on the corresponding low-power external cavity mode. This explanation allows us to understand the origin of LFF, and also to conclude that the presence of LFF in the dynamics of a laser under optical feedback is a manifestation of deterministic chaos. Many different phenomena can lead to slow fluctuations in a SCL under optical feedback, such as a misaligned optical cavity [52]. To recognize LFF among these fluctuations, the study of the statistics of the period between two consecutive drop-outs is necessary [53, 54, 55, 56]. In most cases, the LFF appears very close to threshold, but it has also been observed at higher bias currents, where LFF and CC may coexist, until the fully developed CC regime takes over at high bias current or

high feedback strengths. LFF can even coexist with stable emission close to threshold at very high feedback strengths as depicted in fig 3.11 and in [57].

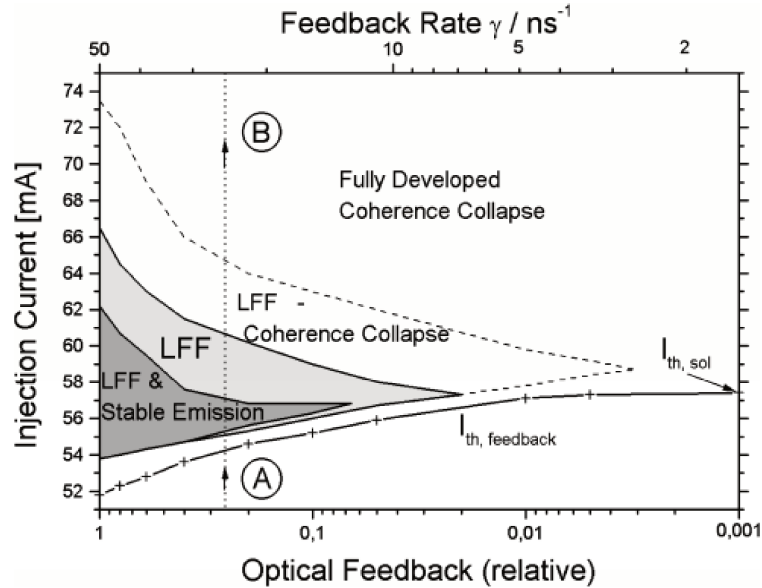


Figure 3.11: Mapping of the appearance of LFF as a function of the feedback strength and the bias. The LFF regime is depicted in light gray. The dark-gray region embedded in the LFF regime corresponds to the region of coexistence of the stable emission state and the LFF state. The unshaded region encompassed by the dashed line corresponds to the continuous transition between the LFF regime and the fully developed coherence collapse regime. current [57].

In this figure, the resulting dynamic behavior of the SCL and the respective LFF as a function of optical feedback strength and injection current can be observed. Increasing the injection current along the vertical dotted line from A to B corresponding to a feedback rate of  $25 \text{ ns}^{-1}$ , one reaches every dynamical regime present in the feedback-injection current space [57].

In what follows in Chapter IV, the impact of both short and long-cavity optical feedback is studied in hybrid III-V Si SCLs. The results obtained show that many types of instabilities can arise when these devices are subject to variations of feedback strengths. In addition, enhancement of the chaotic bandwidth by either suppressing or increasing the optical feedback levels is experimentally demonstrated in view of developing secured communications integrated on chip.

## REFERENCES

- [1] R. Lang and K. Kobayashi, "External optical feedback effects on semiconductor injection laser properties," *IEEE Journal of Quantum Electronics*, vol. 16, no. 3, pp. 347–355, 1980.
- [2] R. Broom, E. Mohn, C. Risch, and R. Salathe, "Microwave self-modulation of a diode laser coupled to an external cavity," *IEEE Journal of Quantum Electronics*, vol. 6, no. 6, pp. 328–334, 1970.
- [3] I. Ikushima and M. Maeda, "Self-coupled phenomena of semiconductor lasers caused by an optical fiber," *IEEE Journal of Quantum Electronics*, vol. 14, no. 5, pp. 331–332, 1978.
- [4] H. Huang, "Optical nonlinearities in quantum dot lasers for high-speed communications," PhD thesis, Télécom ParisTech, Mar. 2017.
- [5] Y. Cunyun, *Tunable external cavity diode lasers*. WORLD SCIENTIFIC, 2004.
- [6] Éléonore Hardy, *Optical feedback in lasers*, <http://mylaserspectrum.com/2016/09/optical-feedback-lasers/>, Sep. 2016.
- [7] V. Kovanis, A. Gavrielides, and P. Alsing, "Taming chaos in semiconductor lasers subject to optical feedback," in *Proceedings of LEOS 93*, IEEE.
- [8] D. M. Kane and K. A. Shore, Eds., *Unlocking dynamical diversity*. Wiley, 2005.
- [9] S. H. Strogatz, *Nonlinear dynamics and chaos: With applications to physics, biology, chemistry and engineering (studies in nonlinearity)*. CRC Press, 1994, ISBN: 0-201-54344-3.
- [10] E. Rosencher, B. Vinter, and P. G. Piva, *Optoelectronics*. Cambridge University Press, 2002.
- [11] G. P. P. F. T. Arecchi G. L. Lippi and J. R. Tredicce, *Deterministic chaos in lasers with injected signal*, O. Communications, Ed., Oct. 1984.
- [12] F. Favre, D. L. Guen, and J. Simon, "Optical feedback effects upon laser diode oscillation field spectrum," *IEEE Transactions on Microwave Theory and Techniques*, vol. 30, no. 10, pp. 1700–1705, 1982.

- [13] L. Goldberg, H. Taylor, A. Dandridge, J. Weller, and R. Miles, "Spectral characteristics of semiconductor lasers with optical feedback," *IEEE Transactions on Microwave Theory and Techniques*, vol. 30, no. 4, pp. 401–410, 1982.
- [14] R. Tkach and A. Chraplyvy, "Regimes of feedback effects in 1.5- $\mu\text{m}$  distributed feedback lasers," *Journal of Lightwave Technology*, vol. 4, no. 11, pp. 1655–1661, 1986.
- [15] Y. Chung and Y. Lee, "Spectral characteristics of vertical-cavity surface-emitting lasers with external optical feedback," *IEEE Photonics Technology Letters*, vol. 3, no. 7, pp. 597–599, 1991.
- [16] S. Donati and R.-H. Horng, "The diagram of feedback regimes revisited," *IEEE Journal of Selected Topics in Quantum Electronics*, vol. 19, no. 4, pp. 1 500 309–1 500 309, 2013.
- [17] J. S. Lawrence, D. M. Kane, and P. S. Spencer, "Suppression of coherence collapse in semiconductor diode lasers with short external cavities," in *Advanced Semiconductor Lasers and Their Applications*, OSA, 1999.
- [18] D. O'Brien, S. P. Hegarty, G. Huyet, and A. V. Uskov, "Sensitivity of quantum-dot semiconductor lasers to optical feedback," *Optics Letters*, vol. 29, no. 10, p. 1072, 2004.
- [19] M. Fleming and A. Mooradian, "Spectral characteristics of external-cavity controlled semiconductor lasers," *IEEE Journal of Quantum Electronics*, vol. 17, no. 1, pp. 44–59, 1981.
- [20] R. Wyatt and W. Devlin, "10 kHz linewidth 1.5  $\mu\text{m}$  InGaAsP external cavity laser with 55 nm tuning range," *Electronics Letters*, vol. 19, no. 3, p. 110, 1983.
- [21] H. Temkin, N. Olsson, J. Abeles, R. Logan, and M. Panish, "Reflection noise in index-guided InGaAsP lasers," *IEEE Journal of Quantum Electronics*, vol. 22, no. 2, pp. 286–293, 1986.
- [22] M. C. Soriano, J. García-Ojalvo, C. R. Mirasso, and I. Fischer, "Complex photonics: Dynamics and applications of delay-coupled semiconductor lasers," *Reviews of Modern Physics*, vol. 85, no. 1, pp. 421–470, 2013.
- [23] F. Rogister, "Nonlinear dynamics of semiconductor lasers subject to optical feedback," PhD thesis, Polytechnique de Mons, Oct. 2001.
- [24] F. Grillot, "On the effects of an antireflection coating impairment on the sensitivity to optical feedback of AR/HR semiconductor DFB lasers," *IEEE Journal of Quantum Electronics*, vol. 45, no. 6, pp. 720–729, 2009.

- [25] J. Mork, M. Semkow, and B. Tromborg, “Measurement and theory of mode hopping in external cavity lasers,” *Electronics Letters*, vol. 26, no. 9, p. 609, 1990.
- [26] J. Osmundsen and N. Gade, “Influence of optical feedback on laser frequency spectrum and threshold conditions,” *IEEE Journal of Quantum Electronics*, vol. 19, no. 3, pp. 465–469, 1983.
- [27] G. Agrawal, “Line narrowing in a single-mode injection laser due to external optical feedback,” *IEEE Journal of Quantum Electronics*, vol. 20, no. 5, pp. 468–471, 1984.
- [28] K. Petermann, *Laser diode modulation and noise*. Springer Netherlands, 1988.
- [29] C. Henry, “Theory of the linewidth of semiconductor lasers,” *IEEE Journal of Quantum Electronics*, vol. 18, no. 2, pp. 259–264, 1982.
- [30] N. Schunk and K. Petermann, “Numerical analysis of the feedback regimes for a single-mode semiconductor laser with external feedback,” *IEEE Journal of Quantum Electronics*, vol. 24, no. 7, pp. 1242–1247, 1988.
- [31] C. Henry and R. Kazarinov, “Instability of semiconductor lasers due to optical feedback from distant reflectors,” *IEEE Journal of Quantum Electronics*, vol. 22, no. 2, pp. 294–301, 1986.
- [32] K. Petermann, “External optical feedback phenomena in semiconductor lasers,” *IEEE Journal of Selected Topics in Quantum Electronics*, vol. 1, no. 2, pp. 480–489, 1995.
- [33] L. JUMPERTZ, “Photonique non-linéaire dans les lasers à cascade quantique moyen infrarouges,” PhD thesis, TELECOM ParisTech, Nov. 2016.
- [34] A. M. Levine, G. H. M. van Tartwijk, D. Lenstra, and T. Erneux, “Diode lasers with optical feedback: Stability of the maximum gain mode,” *Physical Review A*, vol. 52, no. 5, R3436–R3439, 1995.
- [35] D. Lenstra, B. Verbeek, and A. D. Boef, “Coherence collapse in single-mode semiconductor lasers due to optical feedback,” *IEEE Journal of Quantum Electronics*, vol. 21, no. 6, pp. 674–679, 1985.
- [36] P. M. Alsing, V. Kovanis, A. Gavrielides, and T. Erneux, “Lang and kobayashi phase equation,” *Physical Review A*, vol. 53, no. 6, pp. 4429–4434, 1996.
- [37] S. H. Strogatz, *Nonlinear dynamics and chaos*. CRC Press, 2018.
- [38] A. Hohl and A. Gavrielides, “Bifurcation cascade in a semiconductor laser subject to optical feedback,” *Physical Review Letters*, vol. 82, no. 6, pp. 1148–1151, 1999.

- [39] A. Ryan, G. Agrawal, G. Gray, and E. Gage, "Optical-feedback-induced chaos and its control in multimode semiconductor lasers," *IEEE Journal of Quantum Electronics*, vol. 30, no. 3, pp. 668–679, 1994.
- [40] J. Law and G. Agrawal, "Effects of optical feedback on static and dynamic characteristics of vertical-cavity surface-emitting lasers," *IEEE Journal of Selected Topics in Quantum Electronics*, vol. 3, no. 2, pp. 353–358, 1997.
- [41] J. Mork, B. Tromborg, and J. Mark, "Chaos in semiconductor lasers with optical feedback: Theory and experiment," *IEEE Journal of Quantum Electronics*, vol. 28, no. 1, pp. 93–108, 1992.
- [42] T. Mukai and K. Otsuka, "New route to optical chaos: Successive-subharmonic-oscillation cascade in a semiconductor laser coupled to an external cavity," *Physical Review Letters*, vol. 55, no. 17, pp. 1711–1714, 1985.
- [43] T. Heil, I. Fischer, W. Elsässer, and A. Gavrielides, "Dynamics of semiconductor lasers subject to delayed optical feedback: The short cavity regime," *Physical Review Letters*, vol. 87, no. 24, 2001.
- [44] R. Jones, J. Lawrence, D. Kane, and P. Spencer, "Influence of external cavity length on the coherence collapse regime in laser diodes subject to optical feedback," *IEE Proceedings - Optoelectronics*, vol. 148, no. 1, pp. 7–12, 2001.
- [45] O. B.H.-J. W. O. Ushakov S. Bauer and F. Henneberger, "Dynamics of lasers with ultra-short optical feedback," vol. 5349, SPIE, 2004, pp. 348–357.
- [46] M. Sciamanna, P. Megret, and M. Blondel, "Hopf bifurcation cascade in small- $\alpha$  laser diodes subject to optical feedback," *Physical Review E*, vol. 69, no. 4, 2004.
- [47] J. Ohtsubo, "Feedback induced instability and chaos in semiconductor lasers and their applications," *Optical Review*, vol. 6, no. 1, pp. 1–15, 1999.
- [48] G. Dente, P. Durkin, K. Wilson, and C. Moeller, "Chaos in the coherence collapse of semiconductor lasers," *IEEE Journal of Quantum Electronics*, vol. 24, no. 12, pp. 2441–2447, 1988.
- [49] J. Mork, B. Tromborg, and P. Christiansen, "Bistability and low-frequency fluctuations in semiconductor lasers with optical feedback: A theoretical analysis," *IEEE Journal of Quantum Electronics*, vol. 24, no. 2, pp. 123–133, 1988.
- [50] T. Sano, "Antimode dynamics and chaotic itinerancy in the coherence collapse of semiconductor lasers with optical feedback," *Physical Review A*, vol. 50, no. 3, pp. 2719–2726, 1994.

- [51] M.-W. Pan, B.-P. Shi, and G. R. Gray, “Semiconductor laser dynamics subject to strong optical feedback,” *Optics Letters*, vol. 22, no. 3, p. 166, 1997.
- [52] P. Besnard, B. Meziane, and G. Stephan, “Feedback phenomena in a semiconductor laser induced by distant reflectors,” *IEEE Journal of Quantum Electronics*, vol. 29, no. 5, pp. 1271–1284, 1993.
- [53] D. W. Sukow, J. R. Gardner, and D. J. Gauthier, “Statistics of power-dropout events in semiconductor lasers with time-delayed optical feedback,” *Physical Review A*, vol. 56, no. 5, R3370–R3373, 1997.
- [54] J. Sacher, W. Elsässer, and E. O. Göbel, “Intermittency in the coherence collapse of a semiconductor laser with external feedback,” *Physical Review Letters*, vol. 63, no. 20, pp. 2224–2227, 1989.
- [55] C. Sun, M. T. Wade, Y. Lee, J. S. Orcutt, L. Alloatti, M. S. Georgas, A. S. Waterman, J. M. Shainline, R. R. Avizienis, S. Lin, B. R. Moss, R. Kumar, F. Pavanello, A. H. Atabaki, H. M. Cook, A. J. Ou, J. C. Leu, Y.-H. Chen, K. Asanović, R. J. Ram, M. A. Popović, and V. M. Stojanović, “Single-chip microprocessor that communicates directly using light,” *Nature*, vol. 528, no. 7583, pp. 534–538, 2015.
- [56] M. C. Eguia and G. B. Mindlin, “Semiconductor laser with optical feedback: From excitable to deterministic low-frequency fluctuations,” *Physical Review E*, vol. 60, no. 2, pp. 1551–1557, 1999.
- [57] T. Heil, I. Fischer, and W. Elsässer, “Coexistence of low-frequency fluctuations and stable emission on a single high-gain mode in semiconductor lasers with external optical feedback,” *Physical Review A*, vol. 58, no. 4, R2672–R2675, 1998.

## CHAPTER 4

### HYBRID III-V/SI SEMICONDUCTOR LASERS

In the case of integrated photonics, identifying the sensitivity to optical feedback of novel laser sources involves studying the impact of external cavities below a few centimeters to a few meters long to simulate reflections from nearby components and short fiber networks. Indeed, identifying sources of parasitic reflections inside the laser cavity, such as at the interface between the III-V material and the Si waveguide [1] remains a critical challenge that must continue to be addressed to further understand the stability constraints of such integrated lasers.

As discussed in Chapter III, optical feedback should not only be seen as a detrimental phenomenon but also as a well-established technique used to create, i.e., chaotic transmitters for secure transmissions and random bit generation [2, 3]. Several encoding and decoding schemes for communication applications have already been demonstrated by using the synchronization of chaos in SCLs [4]. As the results below demonstrate, the ROF is indicative of the maximum possible rate of data transmission in chaotic systems of SCLs [5] and can be greatly enhanced by optical feedback [6]. Therefore, SCLs with a high frequency of chaotic carrier are desirable as a light source of chaotic communications to perform high data rate transmissions. Thus, understanding the behavior of these devices when subject to optical feedback is important to introduce new approaches for secure communications since any parasitic reflection may make it difficult to transpose such well-known technique to SiPh.

In [7], an integrated laser with a filtered-feedback configuration is studied, where the dynamics of such device were investigated as a function of the feedback phase and injection current, revealing both stable and unstable single-frequency regimes. In this chapter, the response of three different hybrid III-V/Si SCLs in the steady and dynamic states is

carefully analyzed to assess the sensitivity of the output intensity to both amplitude and phase variations. Several measurements are performed using different feedback strengths at different distances to reflection in order to investigate the impact on the performance characteristics of the devices when subject to short-cavity, long-cavity and subsequently a combination of both types of feedbacks.

In this work, I provide the very first experimental investigation of these novel hybrid III-V/Si SCLs subject to optical feedback. Compared to recently reported devices directly grown on Si [8], the SCLs under test allow studying the dynamics of the III-V active region within a Si optical cavity. A description of the devices is first presented followed by comprehensive experimental results of the FP and the DFB laser under a combination of two types of optical feedbacks: very short-cavity free-space feedback and long-cavity fibered feedback. The long fibered feedback cavity was created within the experimental set-up to study the route to chaos of these devices under long-cavity feedback. The short-cavity reflection measurements were conducted by coupling the laser using a cleaved fiber, thus creating a free-space cavity between the laser and the tip of the fiber to determine the impact of the feedback's phase on this route. The dynamics of a TUL based on an extension of the FP laser design just mentioned is also investigated but under long-cavity feedback only. The impact of sub-cavities in the Si waveguide is also of great interest for the development of PIC and are also discussed.

Short-cavity reflections within a PIC can potentially destabilize these lasers due to the tight heterogeneous integration of optical components as previously discussed. The sensitivity of these devices to this short-cavity feedback was examined by comparing measurements performed with both a cleaved and an AR coated lensed fiber, and revealed the modal and temporal dynamics created by such cavity. Results demonstrate that short-cavity feedback significantly impacts the behavior of the SCLs and influences the route to chaos under long-cavity feedback. A combination of short and long-cavity feedback can successfully generate chaotic dynamics in these type of devices, ideal to carry out chaotic secure

communications. The information gathered shows that accurate manipulation of the feedback strength can be performed to dynamically control deterministic chaos [9] and tune the bandwidth based on the desired application and performance.

Last but not least, direct modulation measurements at 10 Gbps for a 10 km transmission are also conducted on the DFB device only to closely examine its ability to enable a floor-free transmission with low power penalty degradation. Information on the CC is provided and the transition to chaotic state due to the non-linear dynamics effects is experimentally demonstrated. The devices under investigation play an extremely important role in digital communications because they offer precise control of the lasing wavelength; therefore, understanding their limitations and identifying their strengths is of paramount importance for the rising generation of data centers to meet the increased bandwidth demand. The experimental results reported herein, can serve as a source of information to assist researchers in the field with making informed decisions for technology improvements and to optimize the development for practical applications such as future high-speed integrated circuits. The motivation to study these complex structures was two-fold: to compare the performance results between different laser configurations and to identify their potential as chaotic transmitters.

#### **4.1 Devices under Study and Experimental Set-up**

The first two devices studied are based on a FP laser cavity inspired from [10]. The fabrication starts with 200 mm SOI wafers with a 440 nm thick Si top layer. The III-V region consists of a *p*-InGaAs contact layer, a *p*-InP cladding layer and 6 InGaAsP QWs surrounded by two InGaAsP separate confinement heterostructure layers, and an *n*-InP layer. Fig. 4.1 illustrates the the FP laser and a TUL under investigation. The FP laser consists of a 1.2 mm-long optical cavity. The InP-based amplification section, sitting above the Si waveguide, occupies most of the cavity and each end is tapered to allow modal transfer between the III-V and Si waveguides. About 140  $\mu\text{m}$  away from the tip of each tapers,

DBRs with reflectivities of 30% and 100%, form the optical cavity. Outside the cavity, additional Bragg gratings with reflectivities below 1% are placed about  $130\ \mu\text{m}$  away from the cavity's DBRs to allow vertical output fiber coupling [11]. The design of the TUL is more complex, with an active region only  $400\ \mu\text{m}$ -long and Si waveguides that include two ring resonators with metal heaters on top of the rings for thermal wavelength tuning. These have FSRs of 400 and 440 GHz, respectively, allowing selection of a single cavity mode if tuned properly, thus enabling tunable single mode emission. As will be discussed later, the TUL studied in this work is cleaved in the III-V region, thus removing one of the tapers as well as the Si waveguide containing the cavity's lower-reflectivity mirror and the VBG as depicted below.

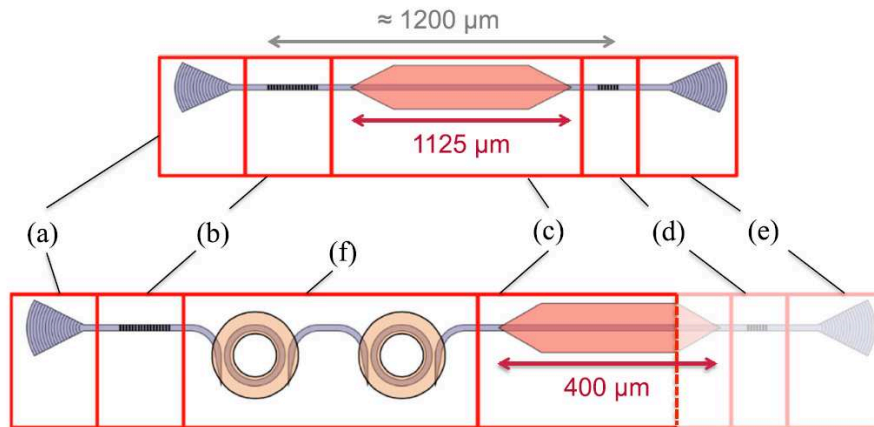


Figure 4.1: Schematic view of the FP (top) and TUL (bottom) under study, with the Si waveguides shown in grey. The lettered sections correspond to (a) and (e) vertical couplers, (b) high-reflectivity DBR, (c) III-V gain section, (d) low-reflectivity DBR, and (f) Si rings. The dotted red line on the TUL design shows where the samples used in this study were cleaved.

The third device under investigation is a 1 mm-long hybrid III-V/Si DFB laser as illustrated in fig. 4.2. As described in [10], the hybrid III-V SOI is fabricated using a III-V QW active medium bonded on top of a processed Si waveguide consisting of a DBF laser with tapers on each side. To ensure single-mode operation, a 50 nm-deep and 600 m-long Bragg grating with a quarter-wavelength phase shift in the center is etched on the Si wave-

uide below the III-V material. The strength of the grating is chosen such that the product  $kL_{Bragg}$  is of a few units, and the period of the grating is 240 nm. The light is coupled from the Si waveguide to the III-V material with adiabatic tapers, and outcoupled using VBG on both sides of the device. The VBG couples the light out of the laser with an angle of  $80^\circ$  from the waveguide; therefore, light must thus be coupled vertically using a fiber positioned above the laser, with a  $10^\circ$  angle from the normal to the laser's surface.

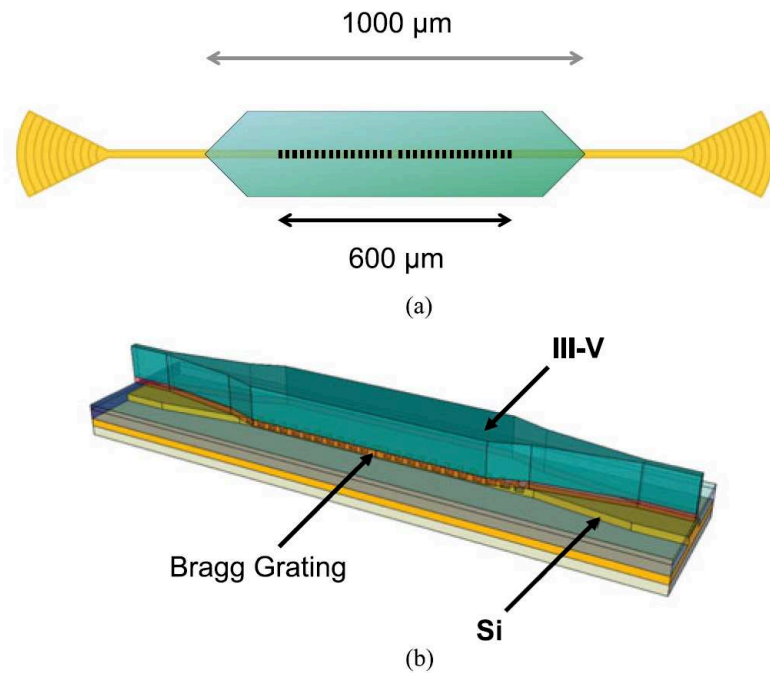


Figure 4.2: (a) Schematic and (b) structure of the device studied, showing the Si waveguide (yellow) and the III-V material (green). The vertical couplers are represented in (a) at both extremities of the Si waveguide.

Fig. 4.3 presents a schematic of the experimental fiber setup used to characterize the free-running lasers and to conduct the optical feedback study. Two external cavities can be considered. First, a short free-space cavity (blue arrow on the schematic) of the order of  $20 \mu\text{m}$  for the FP/TUL and about  $100 \mu\text{m}$  for the DFB study (corresponding to an external round trip time on the order of a few ps) created by the tip of the cleaved fiber [12], was used to both collect the light emitted by the devices and inject the light from the longer cavity. The re-injected light of the short free-space feedback cavity into the device is  $\approx 3\%$ . The

latter is a fiber cavity (red arrow on the schematic) about 7 m long (corresponding to an external round trip time of 70 ns), created using a Yenista back-reflector (BKR) module equivalent to a mirror with adjustable losses, as depicted on the experimental diagram. The re-injected light of the fibered set-up into the device is  $\approx 8\%$ . While the back-reflector preserves the light's polarization over its whole range of attenuation, it is unclear whether the phase changes as the attenuation is changed. A 90/10 coupler was employed to split the light in two directions: 90% of the light collected from the laser was used for the long external cavity. The remaining 10% of the light was analyzed using a power-meter (PM) as well as an optical spectrum analyzer (OSA) and an electrical spectrum analyzer (ESA).

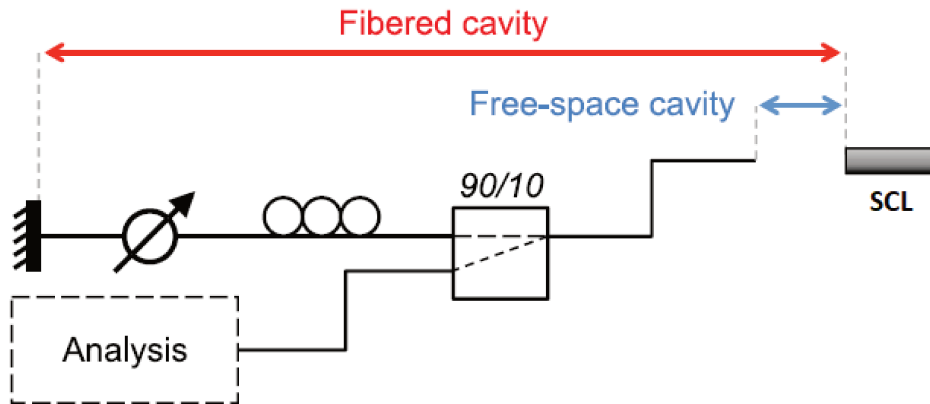


Figure 4.3: Experimental set-up. The blue and red arrows show the short and long external cavities, respectively. The analysis block consist of a combination of a power-meter as well as an optical and an electrical spectrum analyzer.

The fabricated lasers are tested on the wafer through the use of VBGs. The VBGs were only necessary for testing purposes, in order to characterize several unprocessed devices on the same bar but in a PIC the VBGs would not have been positioned after the laser. Therefore, it is important to note that due to the transmission losses of the vertical couplers, a difference must be made between the light re-injected into the component and the light that reaches the laser's cavity. The maximum feedback strengths considering the light that reaches the laser cavity are thus 0.1% and 0.3% for the short and long cavity respectively. Using either fiber and controlling the attenuation of the long feedback allows studying the

three structures described above to assess their sensitivity against optical feedback into the following four scenarios:

1. Free-running with only parasitic reflection from the set-up
2. Short-cavity feedback only (free-space)
3. Long-cavity feedback only (all devices)
4. Under a combination of short and long-cavity feedback

For the short feedback, while the feedback strength is fixed by the refractive index of the fiber, the phase can be tuned using a piezoelectric actuator allowing gradual movement of the fiber towards or away from the device. Concerning the long feedback path, while the feedback phase can be changed in the same manner, this does not impact the laser's behavior's given the long external cavity length. Feedback strength can however be tuned by changing the attenuation of the BKR. Similarly, it is not possible to independently control the strength and phase of the optical feedback reflected by the tip of the fiber: a Melles Griot three-axis piezo-micropositioner was used to optimize the coupling and move the fiber closer towards or away from the device, which affected both feedback phase and strength due to the divergence of the beam emitted by the devices. Depending on the type of fiber used, the short-cavity feedback can either be enhanced or suppressed. On the other hand, as it will be explained in Section 4.1.2, a long-focus AR coated lensed fiber was used with the TULs in order to minimize any parasitic feedback coming from the fiber and study the effect of long-cavity feedback alone. In this case, only light from the set-up can be re-injected into the device.

### 4.1.1 FP Laser

#### *Short-Cavity Feedback*

In this section, the effects of a short-cavity feedback on a FP laser are studied. The external mirror of the cavity is created by the facet of a cleaved fiber placed on a mount holding it with an angle of  $10^\circ$  to the vertical corresponding to the emission angle of the vertical couplers. The shortest achievable distance between the facet of the fiber and that of the laser being around  $10 \mu\text{m}$  and the piezo-micropositioner having a fine displacement range of  $20 \mu\text{m}$ , the average length of the external cavity is estimated to be of  $20 \mu\text{m}$  ( $\tau_{ext} = 1.3 \text{ ps}$ ). The FP laser is kept at a temperature of  $20^\circ\text{C}$ , where its threshold current is  $23 \text{ mA}$ . To verify the effects of the fiber position on the laser, measurements of the power collected by the fiber were performed for minute displacements of the fiber along the vertical axis. Fig. 4.4 presents the coupled power for various voltages applied to the actuator, with the laser biased at  $55 \text{ mA}$ .

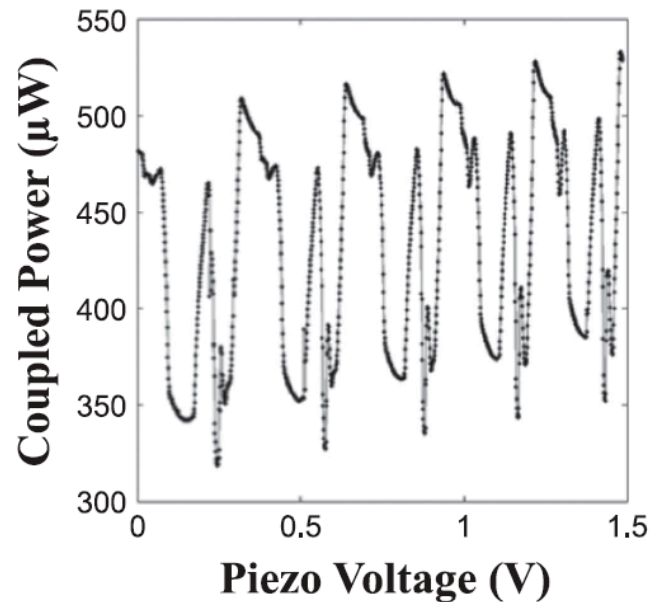


Figure 4.4: Evolution of the coupled light against the voltage applied to the piezo-electric actuator for different fiber displacements along the vertical axis.

The fiber displacement does not appear to linearly follow the applied voltage, as these actuators also exhibit hysteresis, hence the applied voltage is used in the following graphs in place of the actual distance between the fiber and laser facets. Note that this distance increases as the voltage decreases, thus in fig. 4.4 the fiber is the closest to the laser for an applied voltage of 1.5 V. It can be seen that the overall power tends to drop as the voltage decreases, which corresponds to the loss in coupling resulting from the fiber displacement away from the laser. The graph presents a clear periodicity, which confirms that the fiber position influences the laser output and that a short-cavity feedback is created, its phase changing as the fiber moves. It is however difficult to estimate how the feedback strength is evolving. Fig. 4.5 presents the evolution of the optical spectrum of the laser for two slightly different positions of the cleaved fiber.

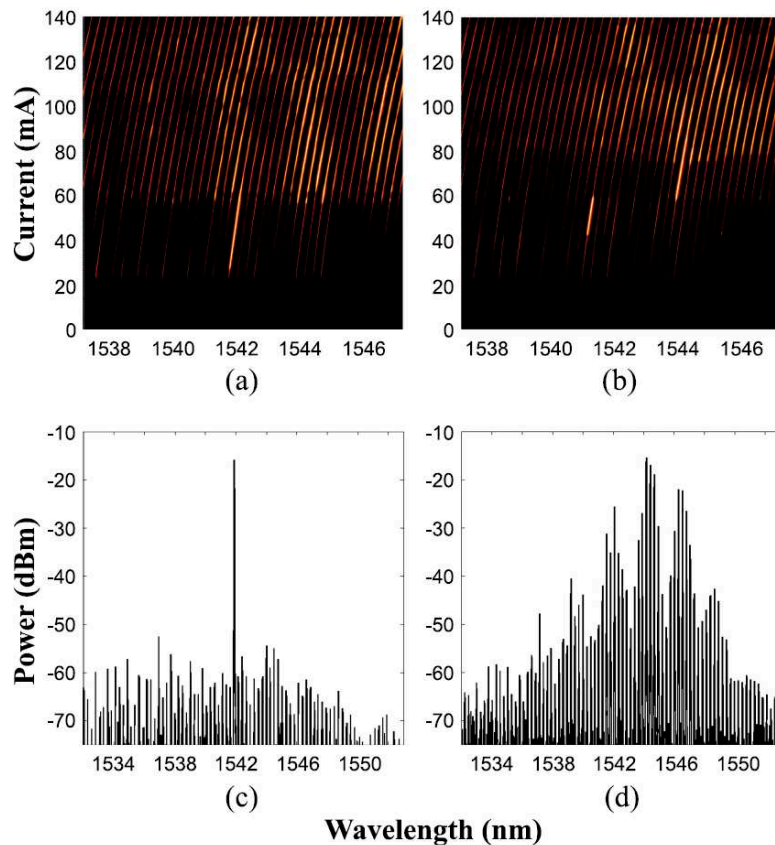


Figure 4.5: Top, optical spectrum evolution of the FP laser for two randomly selected positions of the cleaved fiber. Bottom, excerpts from (a) showing spectra at (c) 40 and (d) 80 mA.

After reaching threshold, emission at a single frequency dominates while all other FP modes are rejected by, e.g., more than 35 dB at 40 mA, as it can be seen in fig. 4.5(c). Above 60 mA, dissimilar behaviors are observed for the different positions of the fiber: in fig. 4.5(b), the laser emits in a multi-mode fashion while in fig. 4.5(a) the laser remains single-mode but switches to another longitudinal mode. Multi-mode emission is only achieved for currents above 75 mA. In addition, it can be seen in fig. 4.5(d) that multi-mode emission does not show a typical gain profile but exhibits a modulation of the spectrum that can be distinguished in both maps. This evolution of the spectrum is very similar to that of recent lasers with an integrated filtered-feedback section [7]. The Fourier transforms of below and above threshold optical spectra were used to identify the various FSRs of the cavities leading to the observed spectra. Assuming a group index of 4, that of the Si waveguides, the FSR corresponding to the overall modulation of the spectrum would correspond to a cavity between 130 and 150  $\mu\text{m}$ . Unlike a traditional external cavity scheme, where the external reflector creates a cavity that is longer than the laser cavity, a sub-cavity within the laser cavity is also observed in this case. Comparing the calculated sub-cavity length with the dimensions of the Si waveguides, the sub-cavity may either stem from reflections between the DBRs and the taper regions, in which case it would be inside the laser cavity, or correspond to the cavity between the fiber facet and the low reflectivity DBR, which would make it a parasitic cavity outside the laser cavity.

These two cases are in fact similar as they both correspond to a sub-cavity outside the gain region, with most of the cavity within the Si waveguide, and therefore; further studies of the proposed laser design are necessary to determine whether or not the taper region can indeed generate enough reflections to create the sub-cavity in question. We thus observe that the FP laser exhibits great sensitivity to short-cavity feedback, in addition to the emission spectrum being strongly affected by a sub-cavity shorter than the laser cavity. Since this impact results in various modal behaviors depending on the position of the fiber, the effect of the short feedback on the behavior of the device under long-feedback is also

investigated and discussed in the following section.

### *Short and Long Cavity Feedbacks*

Fig. 4.6 presents the evolution of the coupled power depending on the two degrees of freedom corresponding to each cavity, with the laser biased at 55 mA. Here, the short-cavity feedback phase and strength are still controlled by the voltage applied to the piezo-micropositioner, but the long-cavity feedback strength is now controlled by the attenuation of the back-reflector.

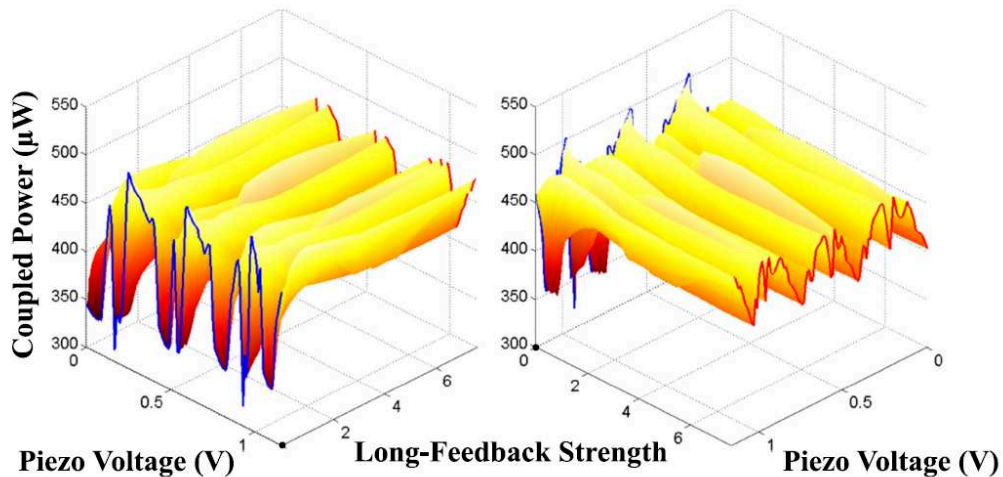


Figure 4.6: Coupled light evolution for both the voltage applied to the piezoelectric actuator (controlling the short cavity-feedback) and the long-feedback strength. The same 3D plot is shown from two angles: one revealing the periodicity of the short-feedback for a long-feedback strength of 0% (blue curve), the other for a long-feedback strength of 7.6% (red curve).

Note that changes in the position of the fiber also affect the phase of the long-cavity feedback; however, this has proven to have little effect on the behavior of reference DFB and FP lasers previously tested in the same setup, and we thus make the assumption that this effect is negligible. The same 3D plot is shown following two angles in order to observe the evolution of the power with the position of the fiber when the long-feedback strength is minimum (blue line) and maximum (red line). For a long-feedback strength of 0% (at the minimum feedback level of 64 dB), the blue line reveals the same pattern as that shown in

fig. 4.4. As the long-feedback strength increases, the FP laser appears to follow different routes depending on the fiber position. Indeed, under maximum long-feedback strength, the red line shows a different pattern than the blue line but with the same periodicity.

Fig. 4.7 presents the evolution of the optical spectrum corresponding to the variation in coupled power. In fig. 4.7(a), the same pattern as in fig. 4.4 can be recognized. Fig. 4.7(b) presents the evolution of the optical spectrum as the fiber is moved, without long-cavity feedback. Drastic changes in the optical spectrum can be observed as the short-feedback parameters change. When the long-cavity feedback is added to the short-cavity it can be seen that, while the modes broaden, the power distribution does not change and the same modes remain dominant.

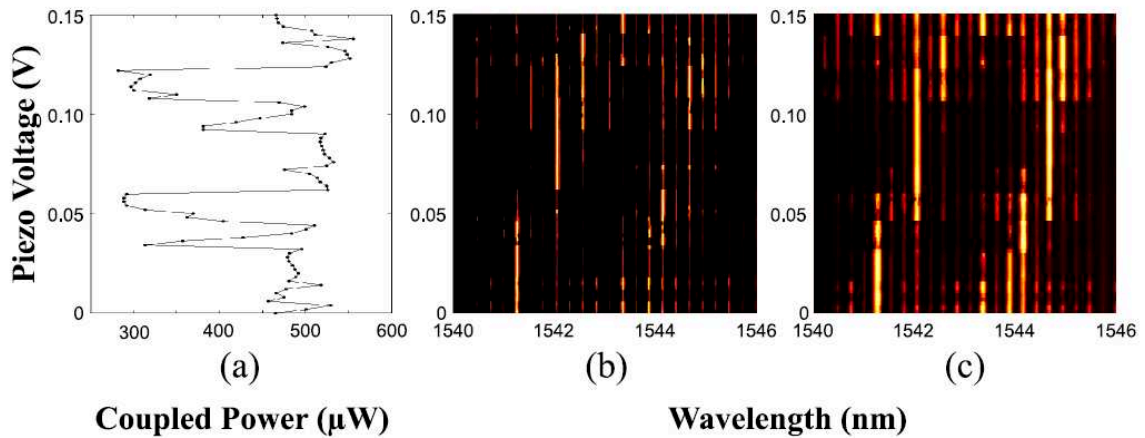


Figure 4.7: Evolution of the voltage applied to the piezoelectric actuator for (a) the coupled power, and the optical spectrum with a long-feedback strength of (b) 0% and (c) 7.6%.

The broadening of the modes is indicative of the apparition of chaotic dynamics. Fig. 4.8 thus presents electrical spectra measured for three different voltages applied to the micro-positioner, and with three levels of long-feedback strength. The black curves show the radio-frequency (RF) spectra of the laser without long-cavity feedback. The main differences between these spectra are the low frequency components, which correspond to partition noise. Fig. 4.8(a) presents the evolution of the RF spectra for a voltage of 0.03 V, as observed in fig. 4.7(b), at this voltage one mode dominates hence the modal competition

is weak and the partition noise is lower than in the other two cases.

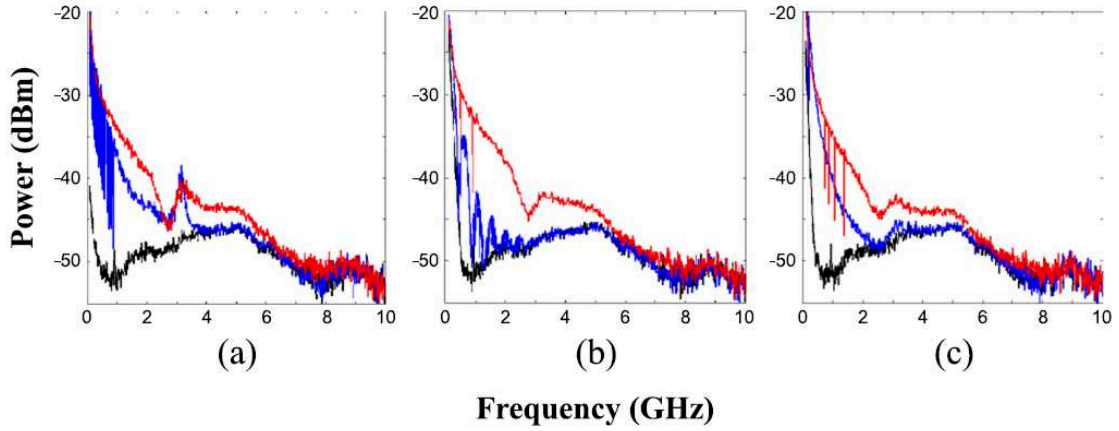


Figure 4.8: Evolution of the electrical spectra for the following piezo-micropositioner voltages: (a) 0.03 V, (b) 0.1 V, (c) 0.14 V. The different long feedback strengths corresponds to 0% (black curves), 4% (blue curves) and 7.6% (red curves).

The route followed by this mode as the long-feedback strength is increased resembles a traditional route to chaos, where relaxation oscillations undamp and lead to a chaotic regime, which can be identified in the RF spectrum by first the apparition of a peak at the ROF of the laser, followed by a strong increase of the spectrum pedestal. However, it can be seen that for the other two fiber positions, different routes to chaos are observed and the chaotic spectra differ slightly. The parasitic effect of the short-cavity feedback thus has a great impact on the behavior of the laser in a long-cavity feedback scheme. In fact, the modal behavior under long-cavity feedback is dictated by the short-cavity feedback, which acts as a seed. Diverse routes to chaos, each leading to chaotic signals with slightly different spectra, can thus be observed for a given operation point of the FP laser.

#### 4.1.2 Tunable Laser

To further understand the behavior and capability of hybrid III-V/Si devices under optical feedback, a TUL is also studied using only long-cavity feedback. As previously mentioned, this device was cleaved within the III-V region towards the end of the taper region, allowing us to perform optical feedback experiments by injecting light directly into the active region.

This configuration also removed a potential source of reflections as both the low-reflectivity DBR and one of the vertical coupler were cut away. For practical applications, these devices are meant to be biased below 100 mA and the two ring resonators must be tuned to obtain stable single-mode emission.

In order to study the laser in unstable regimes, a biased current of 100 mA was applied to the device and the resonators were tuned to obtain single-mode emission. We then mapped the optical and electrical spectra of the free-running TUL for bias currents up to 200 mA to capture evolutionary effects on the laser's properties.

Fig. 4.9 presents the evolution of the optical and electrical spectra as the bias current is increased. The optical spectra shows that, as the laser red-shifts and is detuned from the ring resonators, it enters regions of bi-modal emission.

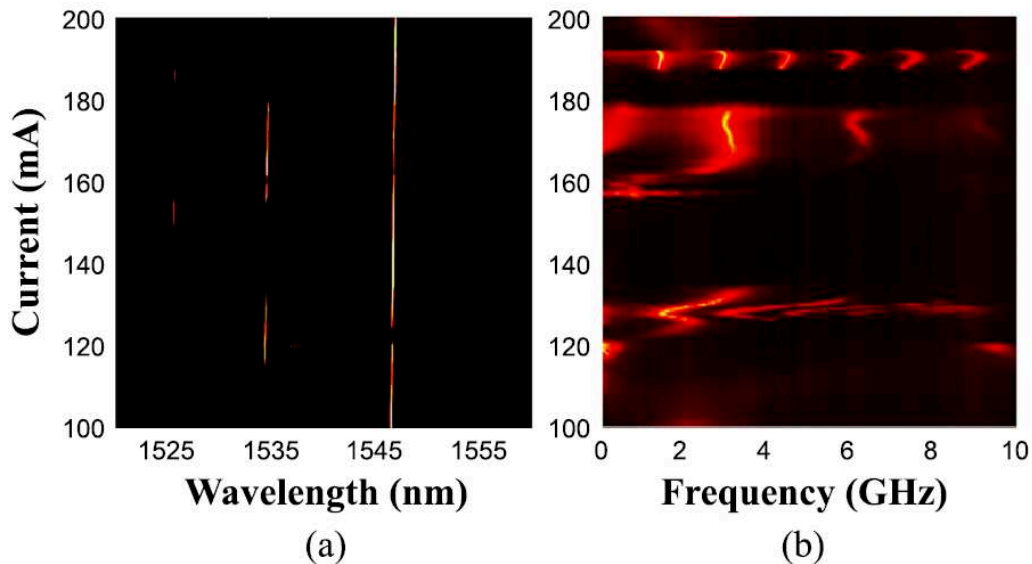


Figure 4.9: Mapping of the (a) optical and (b) electrical spectrum of the free-running TUL as a function of the bias current.

Fig. 4.9(b) shows that these regions of bi-modal emission correspond to regions of oscillations. While these oscillations resemble exalted relaxation oscillations with harmonics, the evolution of the main oscillation frequency does not evolve in the expected manner as the bias current increases. Around 190 mA, the single-mode laser enters a region of strong pe-

riodic oscillations. Unlike the FP laser studied previously, the TUL is here in free-running operation: a long-focus AR coated lensed fiber is used to collect the light emitted by the laser, thus suppressing any short-cavity feedback that could be potentially created by the tip of the fiber, and the laser is not yet subject to long-cavity feedback.

This was indeed verified by repeating measurements for various positions of the fiber, which this time had no effect on the dynamics of the laser. Therefore, any source of instability may thus come from the laser cavity itself as the Si section of the TUL consists of several Si waveguides including the ring resonators. Finally, fig. 4.10 presents the evolution of the electrical spectra of the TUL with its bias current in free-running operation and under strong long-cavity feedback. The two maps look very similar and reveal that instead of following a route to chaos for all currents, the laser only seems to take a route towards a chaotic regime from its free-running dynamics.

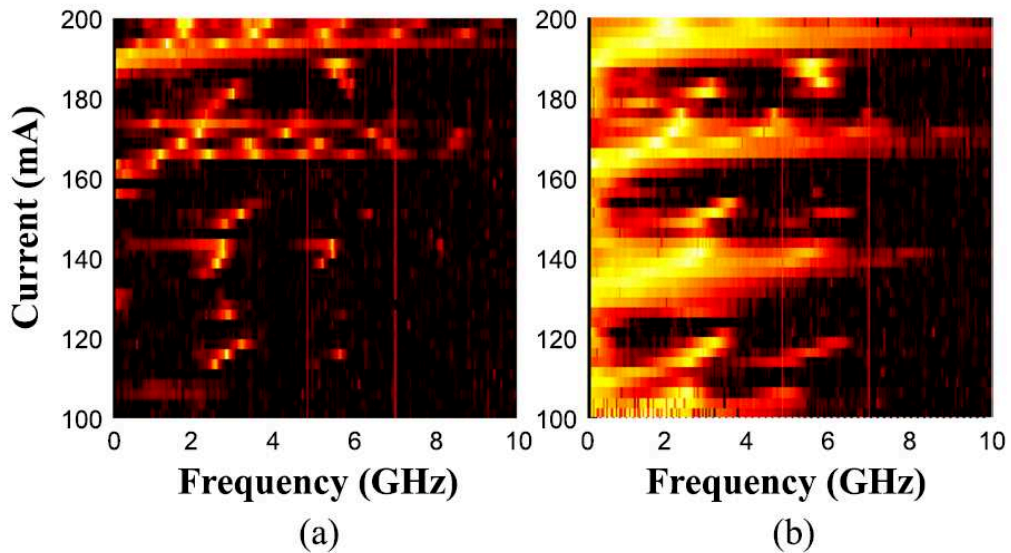


Figure 4.10: Mapping of the electrical spectrum of the TUL with bias current (a) in free-running operation and (b) under long-cavity feedback with a 7.5% strength. The two vertical red lines are measurement artifacts stemming from the RF spectra processing.

Around 120 mA, where the free-running laser is stable, the laser does not exhibit chaotic dynamics under strong long-cavity feedback and only low-frequency components can be observed. Without being subject to an additional short-cavity feedback, the overall behavior

of the TUL is very similar to that of the FP laser. While the FP laser was destabilized intentionally using a short-cavity feedback, the TUL appears to suffer from instabilities that could stem from sub-cavities within the laser cavity itself since no external cavity short-cavity is created in this case. In a similar fashion to the modal behavior of the FP laser, the dynamic behavior of the TUL under long-cavity feedback builds upon the instabilities caused by these sub-cavities.

#### 4.1.3 Hybrid III-V/Si DFB Laser

Due to a relatively high ROF of 15 GHz and the destabilization of the laser by both the short and the long cavity, very wide chaos can be achieved as demonstrated when combining both types of feedbacks. This study thus reveals the great impact parasitic reflections can have on the characteristics of a hybrid III-V/Si DFB laser as well as how these reflections can affect its dynamics in a well-known optical feedback scheme. It is important to point out that the VBGs, however, affected the study in two ways: first via their transmission losses of approximately 7 dB, which will be discussed later, and secondly by their parasitic reflectivity (below -23 dB), which affected laser operation when biased high above threshold.

##### *Static Characterization*

The experimental set-up used to characterize the device under solitary conditions is shown in fig. 4.11. In this case, the DFB laser was isolated from the set-up and the light from the device was coupled using an AR coated lensed fiber. 10% of the light was used to monitor the coupled optical power with a PM. The remaining 90% was amplified using an Erbium-doped fiber amplifier (EDFA) with a fixed output power of 10 dBm, and equally split between the optical and electrical spectrum analyzers. The EDFA was only required to increase the accuracy of the ROF measurements.

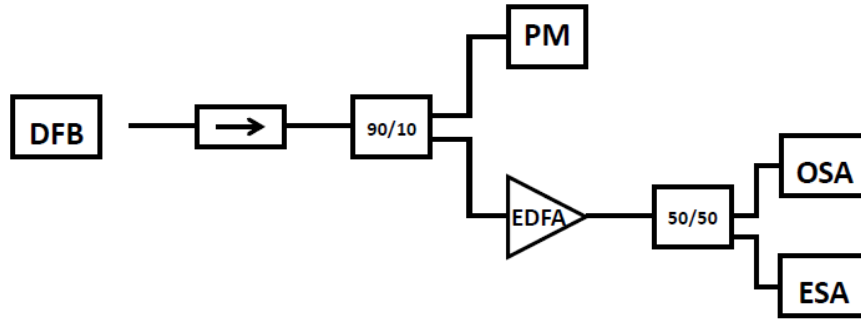


Figure 4.11: Experimental set-up; PM: power-meter, OSA: optical spectrum analyzer, ESA: electrical spectrum analyzer.

Fig. 4.12(a) presents the evolution of the power coupled into the AR coated lens-ended fiber against the applied bias current of the free-running device. The measurements presented in this section were also performed at room temperature. Important information of the dynamical properties of the device can be gained from light-current (L-I) diagram. For instance, it can be noted that around the threshold current of about 45 mA, the laser exhibited slight competition between two modes which translates into a visible subtle kink of the curve. Between 50 to 150 mA, a very stable single-mode operation is observed with a SMSR above 50 dB. Above 4 times the threshold, the laser revealed power drops, which were also observed on another laser from the same bar but differed from device to device. Such behavior is indicative of the presence of parasitic reflections within these devices: the vertical couplers and tapers create reflections which only seems to affect the laser far above the threshold through the variation of the optical power or changes in the ROF as it will be discussed next. Based on this observation, we can say that even the slightest change in the experimental conditions may result in considerable changes, specially in the vicinity of the of the kink. As the amount of parasitic reflections varies from device to device, different sorts of power variations would indeed be expected between different lasers. Fig. 4.12(b) displays the spectrum of the laser at 140 mA, showing the dominant mode along with the well suppressed side-modes in addition to the visible sideband characteristic of relaxation oscillations. These spectra were measured using a Yenista OSA20 OSA with a

20 pm resolution. The sidebands could also be measured due to the rather high value of the ROF.

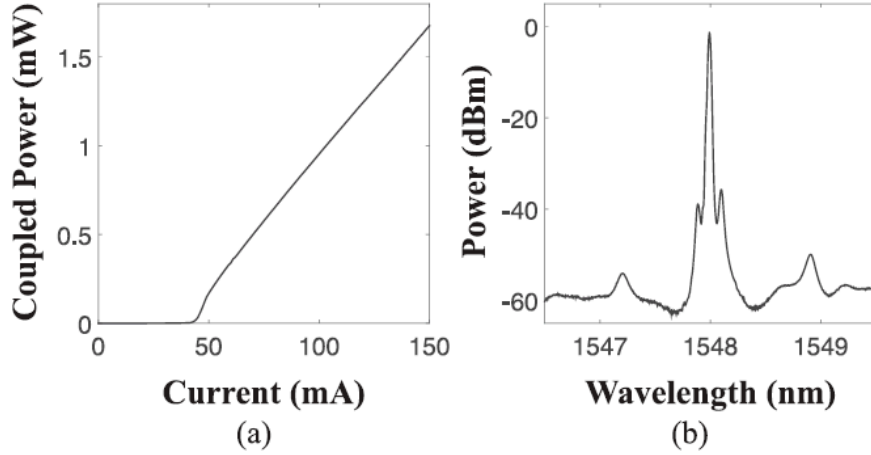


Figure 4.12: (a) Applied current against the output light intensity - Evolution of the power couple using an AR-coated lensed fiber against the bias current applied to the free-running device. (b) Optical spectrum of the laser for  $I = 140$  mA.

Fig. 4.13 presents the evolution of the ROF as a function of the square root of the current overdrive above threshold. In SCLs the ROF  $f_r$  is expressed as

$$\omega_r^2 = (2\pi f_r)^2 \approx \frac{G_N S}{\tau_p} \quad (4.1)$$

$f_r$  refers to an attempt by the photons and carriers to relax to their steady-state values. It can be noted that very high frequencies are observed as the ROF reaches 14 GHz at 150 mA, approximately 3 times the threshold. Usually, due to gain compression, the power evolves in a sub-linear fashion with increasing bias current, and the squared ROF follows the same trend. Here, it can be seen that the ROF evolves in the opposite way as it gradually increases above the linear fitting shown as a dashed line.

At above the threshold, the photon density  $S$  is proportional to  $I - I_{th}$  and the ROF  $f_r$  is proportional to  $\sqrt{I - I_{th}}$ , which is conveyed by figure 4.13. Also, it is known that the ROF of a SCL depends on the square root of the differential gain [13]. Therefore, it is desirable to enhance the differential gain and minimize the volume of the mode ( $\Gamma/V =$

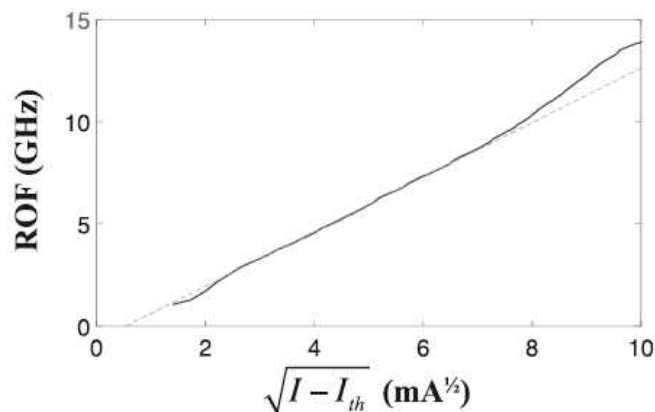


Figure 4.13: Evolution of the ROF with the square root of the current overdrive above threshold.

$1/V_p$ ) and maximize the current relative to threshold for maximum bandwidth. Indeed the 3dB frequency bandwidth scales with ROF (i.e.,  $f_{-3dB} \sim 1.55f_r$ ) [13]. Let us note that if we want to keep the overall drive current low, then we should also try to minimize the threshold current, (i.e., increasing the transmission loss). If, however, we are more concerned about keeping the photon density low (e.g., to reduce the risk of facet damage), then we should try to decrease the cavity lifetime instead, (i.e., decreasing the transmission loss) [13]. The transmission loss coefficient depends on both the facet power reflectivities and the cavity length (see the last term of 2.13).

It is suspected that these high values of ROF obtained during the characterization might come from the use of Aluminium in the III-V compound forming the QW [14], but also from the aftermentioned internal feedback. Under optical feedback, the ROF can oscillate around its free-running value depending on the feedback strength and delay [5]. Here, the internal feedback conditions do allow for a small enhancement of the ROF for some bias currents, showing an effect of parasitic feedback very different from the detrimental impact it can have further above the threshold.

The response of the RF spectrum under different bias currents was also recorded. In fig. 4.14(a) at  $2 \times I_{th}$  (red) the laser exhibits some stability but as the bias value start to rise to 3 and 4 times above  $I_{th}$  (green and blue respectively) the laser experiences broadening of

the spectrum. Fig 4.14(b) displays the evolution of the ROF as the bias current is increased which is in agreement with previous efforts [15]. This dependence is attributed to the larger intra-cavity photon density and the increased damping rate at higher bias currents.

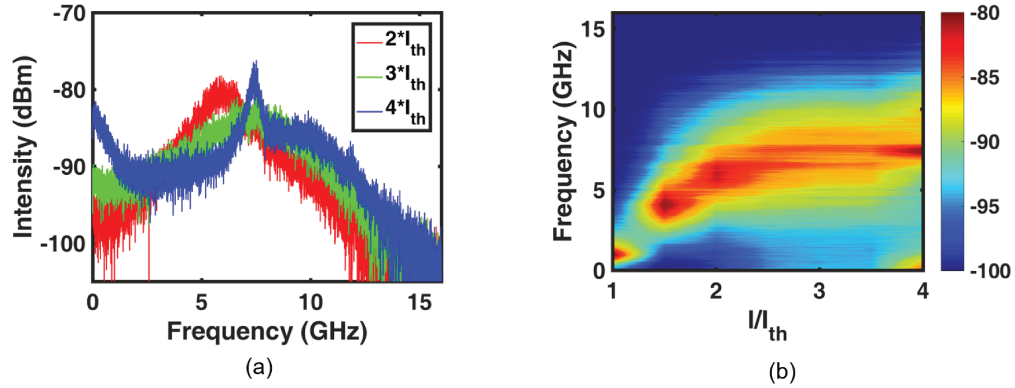


Figure 4.14: Solitary Characteristics of a hybrid III-V/Si DBF Laser at room temperature for different bias currents (a) RF Spectrum and (b) Evolution of the ROF.

Overall, this device offers much more stable operation than the multi and single-mode devices studied in the previous section [16] since no temporal or modal instability were observed in the free-running laser. In both of the previous devices as well as the described in this section, the optical cavity was created using Bragg reflectors in the optical waveguide. However, in our previous study the Bragg reflectors were located in regions of the Si waveguide, which was not covered with active material. Also, the tapered region where light was coupled between Si and III-V waveguides was believed to act as an optical interface creating reflections within the optical cavity. For the DFB lasers, while the Bragg grating is still in the Si waveguide, the optical cavity is confined to the region where Si and III-V overlap, and the taper regions are thus outside the cavity.

#### *Long-Cavity Feedback*

In order to assess the potential of a hybrid III-V/Si laser as chaotic emitters, we first studied that route to chaos that the device follows under long optical feedback. The cavity used for this experiment is too long to realistically represent an external cavity that would be

realistically integrated into a PIC, however, this configuration permits pushing the laser into chaotic operation where the phase of the long feedback has little impact on the dynamic properties of the device. This technique allows to dissociate the effect of the combined short and long feedbacks, as it can be assumed that the feedback phase will only affect the dynamics induced by the short feedback. During the long and short-cavity characterization, the DFB is kept at a bias current of 146 mA and also at temperature of 20°C.

Fig. 4.15 represents the evolution of the optical and RF spectra with long feedback strength using the AR-coated lensed fiber. The measurements performed with this type of fiber have very little dependence on the fiber position and thus the feedback phase, as demonstrated later in the case of the free-running laser. Routes to chaos under long feedback were then found to be identical for different fiber positions.

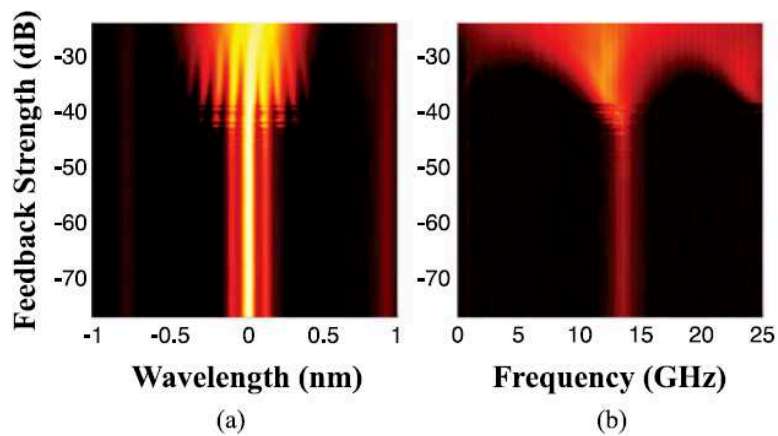


Figure 4.15: Evolution of the (a) Optical and (b) RF spectra following the route to chaos under long feedback using an AR-coated lensed fiber.

The route observed in the results obtained is typical of a DFB laser when subject to optical feedback despite the major difference in the device structures: first of all, the hybrid III-V/Si DFB laser consists of two evanescently couple waveguides, one passive and one active unlike the standard III-V DFB. In addition, in the hybrid device, the tapered regions on each side of the DFB structure may slightly amplify the light back-reflected into the laser or even act as a source of internal reflection [16]. The proposed chaos bandwidth

enhancement method could also be applied to a standard III-V DFB, for which higher feedback strengths could also be achieved. Demonstrating the changes in ROF and bandwidth in the case of a hybrid laser is very interesting as it shows that the complexity of the light sources used in PICs does not necessarily affect their behavior under optical feedback.

For very low feedback strengths, the ROF can be seen at 14 GHz in the RF spectrum. At around -43 dB of feedback strength, temporally unstable periodic oscillations start to appear and stabilize above -40 dB. These periodic oscillations correspond to an excitation of the relaxation oscillations that turn into chaotic dynamics above -30 dB of feedback strength. Under maximum feedback, the bandwidth of the chaotic spectra is 14.5 GHz. The routes exhibited by both lasers appeared to be very similar. Along the feedback strength axis, the routes are shifted by 6 dB as the III-V DFB reaches chaotic operation for only -36 dB of the feedback strength. Note that in the case of the III-V laser, higher feedback were achievable with the same set-up as there were no extra losses between the fiber and the laser cavity.

Fig. 4.16 compares the route to chaos of the hybrid III-V/Si DFB and a traditional commercial Nokia III-V DFB laser. The laser is operated at three times its threshold where a ROF of 8 GHz is achieved.

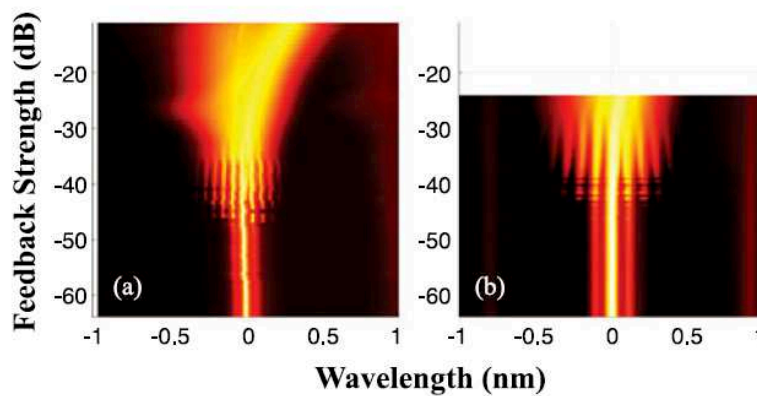


Figure 4.16: Evolution of the optical spectra of (a) a conventional III-V laser and (b) hybrid III-V/Si DFB laser under long optical feedback strength using an AR-coated lensed fiber.

Therefore, it can be seen that with the hybrid III-V/Si DFB, the laser merely enters the chaotic regime, and that much broader spectra could be observed for stronger feedbacks levels. Along the wavelength axis, broader spectra are observed for the hybrid DFB in the region of periodic oscillations as the base frequency of these oscillations is the ROF. It is then expected that the spectra observed in the traditional III-V DFB laser could also be obtained for the hybrid III-V/Si device, broadened by a factor close to the ratio between the two ROFs.

### *Short-Cavity Feedback*

Using the cleaved fiber and setting the long feedback strength to its minimum of -79 dB allows studying the hybrid DFB under short feedback only. Fig. 4.17 depicts the variation of the coupled power as a function of the voltage applied to the piezoelectric actuator.

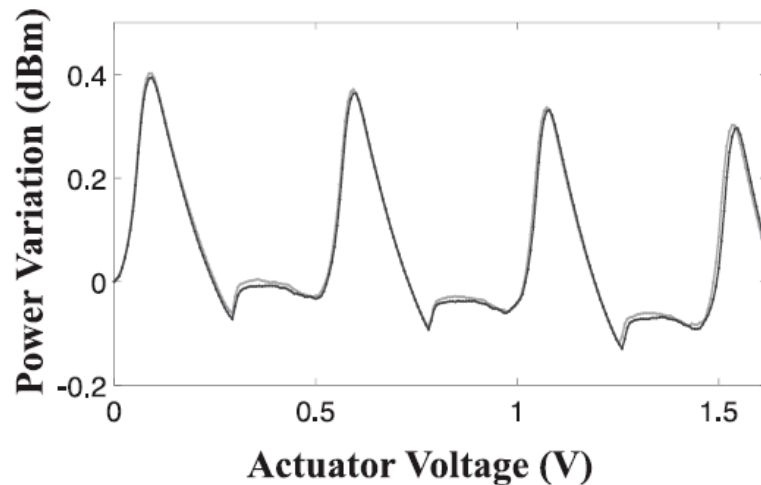


Figure 4.17: Variation of the power coupled with the cleaved fiber as a function of the voltage applied to the piezoelectric actuator. Two measurements for different fiber positions are presented in black and grey.

As the coupling is only optimized for a voltage of 0 V, the power fades as the fiber is moved away from the device and the output image appears skewed. However, a clear periodicity can be observed in the evolution of the power as the phase is altered for the short feedback. For convenience, the main peaks at the beginning of each period were

selected and considered that between each peak; the phase is varied from 0 to  $2\pi$ . Note that this does not represent the absolute phase of the feedback, but only a representation of the phase shift within a period. Such variation of the output power under optical feedback corresponds to the effect of a medium feedback strength and usually exhibits bistability when the mirror is moved either way [5]. Even the lowest levels of intensity noise can create instability on the laser.

Fig. 4.18 compares the evolution of the power and spectrum when the fiber is moved in both directions as well as reference measurements performed with the AR-coated lensed fiber.

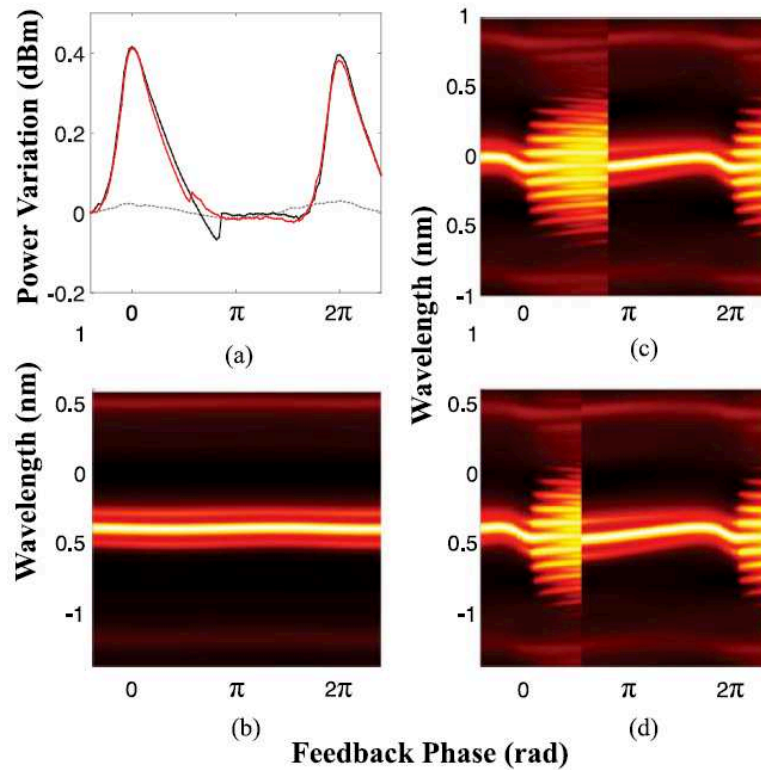


Figure 4.18: (a) Variation of the power coupled with the cleaved fiber within one period when the fiber is moved away (black) and towards (red) the laser. The gray dashed line represents the power coupled when using the AR-coated lensed fiber. (b) Evolution of the optical spectrum when using the AR-coated lensed fiber. (c), (d) Evolution of the optical spectrum when moving the fiber away or towards the laser, respectively.

The reference measurements unveil the weak impact of all parasitic reflections from the experimental set-up and show that the cavity created by the cleaved fiber is mainly respon-

sible for the power variation above. In fig. 4.18(a), the gray dashed lines shows that the power is oscillating sinusoidally with a low amplitude, which corresponds to the impact associated with the weak feedback. Fig. 4.18(b) shows that the wavelength varies in a similar fashion confirming that any other variation of the power or wavelength is only due to the feedback created by the cleaved fiber. Fig. 4.18(a) also reveals a slight bistability in the evolution of the power, as the kinks observed after the peak occur for a phase shift of  $0.3\pi$  for one direction and  $0.4\pi$  for the other. While the bistability in the output power is negligible, it makes a significant difference in the optical spectrum. Note that all spectrum maps presented in this section are plotted in dBm, with a logarithmic color scale. Fig. 4.18(c) reveals that during each period, the laser exhibits periodic dynamics between phases of 0 and  $0.4\pi$ , with period doubling above  $0.2\pi$ . When the kink occurs in the optical power, the laser suddenly stabilises and it can be seen from the sidebands that the ROF changes with the phase. Fig 4.18(d) reveals that the same behavior is also observed when the fiber is moved in the opposite direction, thus leading to a wider region of stability. This wider region is of paramount importance for this study as it appears that the largest ROFs are achieved within the bistability window when the laser is stable, as this is where the mode's sidebands appear to be the farthest apart.

Fig. 4.19 shows the evolution of the optical and RF spectra of the hybrid DFB as the fiber is moved towards the device at a shorter distance. In order to clearly see the peak of the relaxation oscillation in the RF spectra, an EDFA set to a fixed output power of 10 dBm was used to amplify the light before detection. A photodetector with a bandwidth of 30 GHz and a Rhode Schwartz FSP 40 GHz electrical spectrum analyzer were used to perform the spectrum measurements. A slightly larger stability region is obtained and the RF spectra shows that within one period, the ROF varies between a minimum of 11 GHz and a maximum of 16 GHz, thus allowing reaching frequencies 2 GHz higher than the free-running ROF.

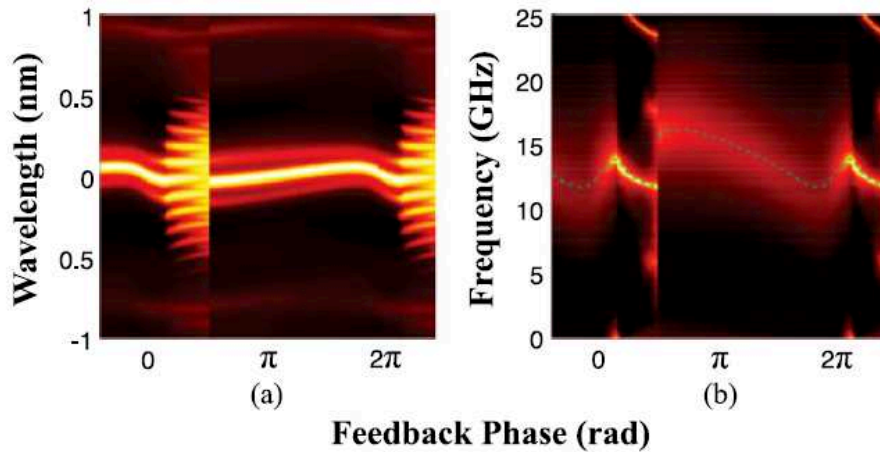


Figure 4.19: Evolution of the (a) optical and (b) RF spectra within one period. The green dashed line shows the evolution of the ROF.

#### *Combination of both Short and Long-Cavity Feedback*

Under long feedback only, the hybrid DFB exhibits a classic route to chaos where chaotic dynamics are obtained from the excitation of the relaxation oscillations. Under short feedback only, it is possible to tune the value of the ROF while keeping the laser in stable operation. Combining both types of optical feedback allows the study of the device whether the enhancement of the ROF under short feedback is used to generate broader chaos by first tailoring the ROF or by exciting relaxation oscillations into chaotic ones. In this section, the laser is thus subject to a combination of short and long feedbacks by using the cleaved fiber and varying the long feedback strength.

Fig. 4.20 presents the bifurcation diagrams of the dynamics as a function of the phase of the short feedback, under minimum and maximum long feedback strengths. Under minimum long feedback strength, the diagram clearly shows the apparition of the periodic oscillations and the sudden transition from oscillating to stable operation. Under maximum feedback, it can be seen that the chaotic signal changes significantly with the short feedback phase.

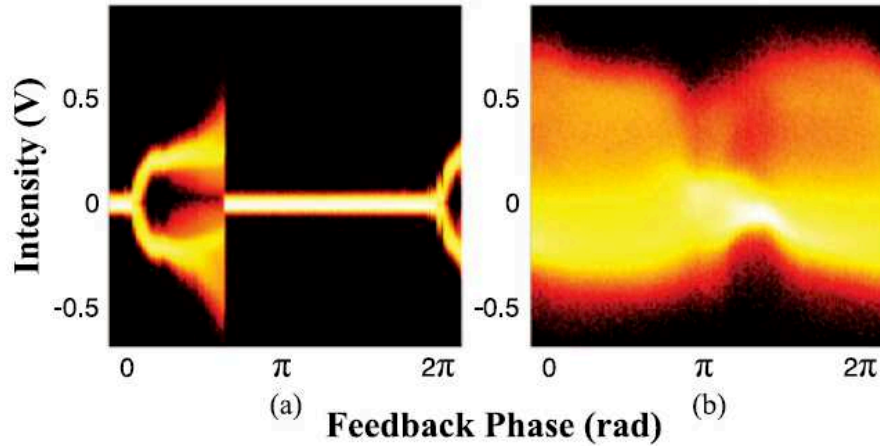


Figure 4.20: Bifurcation diagrams as a function of the short feedback phase under (a) minimum and (b) maximum long feedback strength.

Fig. 4.21 presents the evolution of optical and RF spectra with the position of the cleaved fiber for four levels of long feedback strength: the minimum of -79 dB, -42 dB, -36 dB and the maximum of -26 dB. No optical amplification was used for the RF spectrum measurements. The route towards chaos under long feedback clearly changes with the short feedback phase and interesting instabilities are clearly observed as periodic dynamics appear for different long feedback strengths at the different positions of the cleaved fiber. Regions where periodic oscillations occur under short feedback alone appear to enter chaotic operation first. The sharp transition between oscillating and stable operation gradually disappears as the long feedback strength is increased. The response of this device corresponds to results previously published in literature where the LD exhibits chaos over a bounded range of injection levels while following a period doubling route in and out of chaos [17, 18]. In a similar way as in figs. 4.15 and 4.16, some points exhibit temporally unstable dynamics for feedback phases between  $1.3\pi$  and  $1.5\pi$  and feedback strengths of -42 and -36 dB, which can be seen as a disappearance of the dynamics for some isolated feedback phases. It is interesting to observe that, as the long feedback strength is increased, the wavelength of the spectrum peak oscillates in a more and more sinusoidal fashion, such that no bistability was observed under maximum long feedback strength.

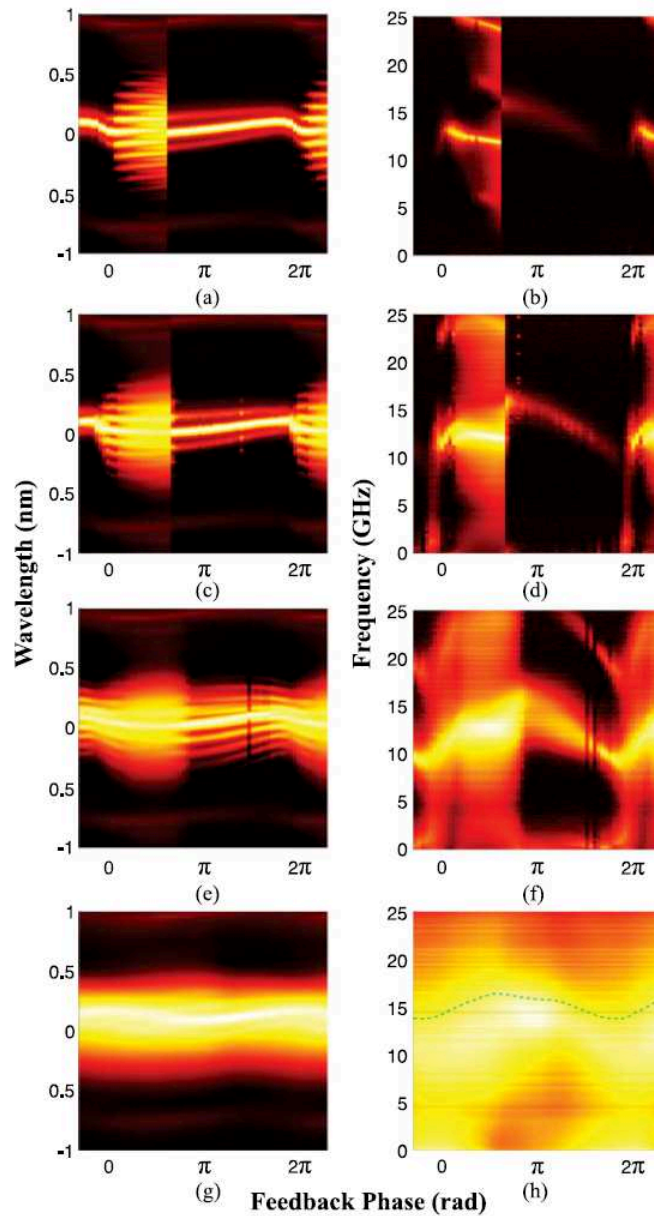


Figure 4.21: Evolution of optical (left) and RF (right) spectra with the position of the cleaved fiber for long feedback strengths of (a), (b) -79 dB, (c), (d) -42 dB, (e), (f) -36 dB and (g), (h) -26 dB. In (h) the black line shows the chaos bandwidth under long feedback only, and the green dashed line shows the evolution of chaos bandwidth with the phase of the short feedback.

The long-cavity feedback strength necessary to reach chaotic operation seems to depend on the short feedback phase, and it can be seen in fig. 4.21(g) and (h) that the width of the chaotic spectrum varies with the feedback phase too. In fig. 4.21(h), the superimposed green dashed line shows the evolution of the chaos bandwidth with the short feedback phase. The black dotted line shows as a reference the bandwidth of the chaos measured under maximum long feedback only, corresponding to the spectrum under maximum long feedback strength in fig. 4.15(b). With the addition of short-cavity feedback, the chaos bandwidth oscillates between 13.7 and 16.4 GHz by following very closely the evolution of the ROF in fig. 4.19(b). Minimum and maximum chaos bandwidth are indeed respectively found close to the feedback phases where minimum and maximum ROF are observed in the absence of long feedback.

Three specific routes to chaos are thus of interest: those where short feedback does not destabilize the laser but induces either a reduction of the ROF to its minimum value of 11 GHz (phase of  $1.9\pi$ ) or an increase to its maximum value of 16 GHz (phase of  $0.3\pi$ ), and one where short feedback induces the strongest periodic oscillations (phase of  $0.25\pi$ ). Fig. 4.22 presents these three routes. In the first two routes, the laser remains stable until slightly higher feedback strengths than compared to fig. 4.15(a). The window where periodic oscillations are observed is however very narrow, as chaos appears around the same feedback strength of about -30 dB. In the last route, chaotic dynamics seem to appear for a lower long feedback strength of -38 dB, but under maximum long-cavity feedback the end of the route appears similar to that in fig. 4.22(d). This is however not surprising given that the last two routes are measured for short feedback phases that are rather close, and that no discontinuity can be seen in fig. 4.21(g) and (h) between these phases.

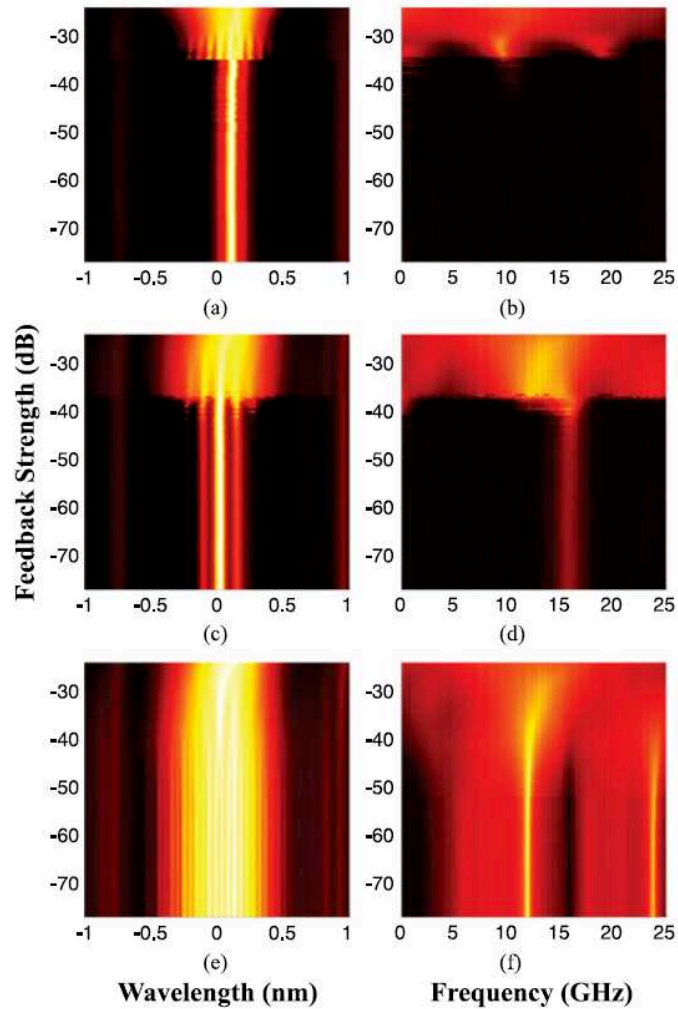


Figure 4.22: Evolution of the optical (left) and RF (right) spectra with the long feedback strength for three positions of the cleaved fiber. a) and b) correspond to a feedback phase of  $1.9\pi$  (minimum ROF, stable). c) and d) correspond to a feedback phase of  $0.3\pi$  (maximum ROF, stable). e) and f) correspond to a feedback phase of  $0.25\pi$  (strongest oscillations).

The optical and RF spectra obtained under maximum long feedback for these three operating conditions are shown in fig. 4.23, along with the free-running spectra and the chaotic ones obtained under maximum long feedback alone. Fig. 4.23(b) shows that the chaotic spectrum obtained for a feedback phase of  $1.9\pi$  leads to the minimum bandwidth of 13.7 GHz observed in fig. 4.21(h). The other routes both lead to a bandwidth of 16.2 GHz, despite slight differences in the chaotic spectra.

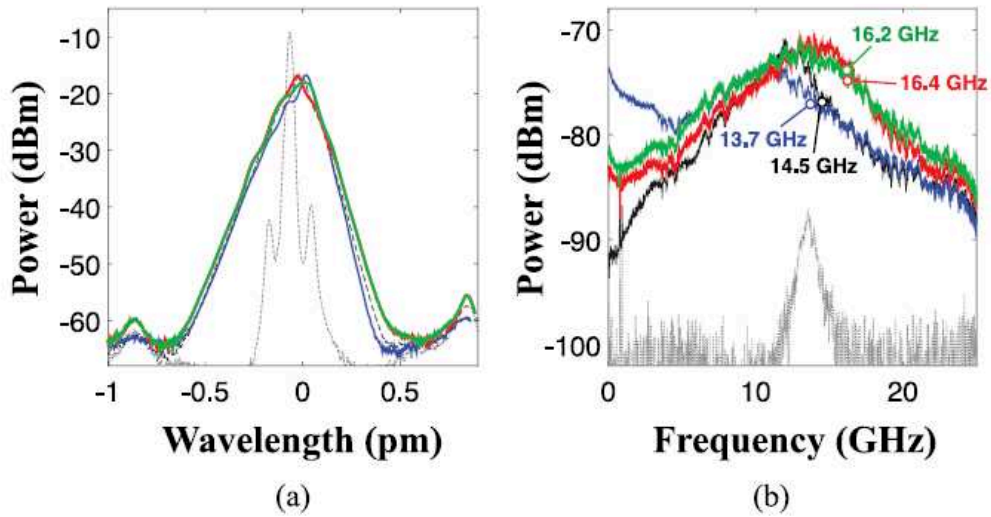


Figure 4.23: Optical (left) and RF (right) spectra under maximum long feedback and their bandwidth, the dashed lines showing the free-running spectra as reference. The black curve corresponds to maximum long feedback alone. The blue (resp. red) curve corresponds to both feedbacks with minimum (maximum) ROF. The green curve corresponds to both feedbacks with strongest periodic oscillations.

Due to large ROF of the free-running DFB, chaotic dynamics with a bandwidth of 14.5 GHz can be generated using long external feedback cavity. In this case, the route to chaos appears to be very similar to that of a standard commercial III-V DFBs, but due to the transmission losses of the device's vertical couplers, maximum feedback strengths of only 0.3% were achieved. The impact of the short external cavity on the laser dynamics revealed a variation of the ROF of 5 GHz, with a maximum value of 16 GHz. When combining short and long feedbacks, this 2 GHz increase of the ROF translates into a similar increase of the chaos bandwidth, which reaches 16.4 GHz.

## 4.2 Direct Modulation

Directly modulated lasers (DML) are optical components for short reach and access networks. Today, power efficient and lower cost optical sources are necessary for the deployment of access and metropolitan networks as well as for supporting new services such as HDTV (High-Definition television), Video-On-Demand (VOD) and cloud-computing among others [19]. In an attempt to provide new services and improve functionality, directly modulated (DM) DFB lasers used as 10 Gbps transmitters offer the desired size reduction, high output power, enhanced optical bandwidth and cost efficiency; hence, these devices are being investigated as a potential solution to satisfy existing hyper-connectivity requirements. In this section, the sensitivity to long-cavity feedback of the hybrid III-V DFB structure described in Section 4.1 (fig. 4.2) is investigated in a back-to-back (B2B) configuration and after transmission using a 10 km fiber coil. Different measurements were collected to better understand direct modulation properties at 10 Gbps and the impact of temperature variation on the performance of the device. A floor-free transmission with a power penalty below 1.5 dB is successfully achieved.

### 4.2.1 Static Characterization

The L-I characteristics of the device were discussed in Section 4.1.3 (fig. 4.12). However, additional measurements of the free-running device were also collected during this part of the characterizations at a higher temperatures of 35°C using the same set-up configuration depicted in fig. 4.3 to investigate the impact of thermal variation on the performance of the hybrid DFB. Fig. 4.24(a) compares the L-I curves and the optical spectra of the device recorded at the two different temperatures also measured at a bias current of 141 mA. The threshold of this device is clearly affected by the temperature differential and it is evident that the threshold current raises and efficiently falls as the temperature increases. At a higher temperature value, the transition time between spontaneous and stimulated emission

increases with a  $I_{th}$  value of 50 mA and a maximum output power of 1 mW. The thermal effects on the device can also be observed in the optical spectrum (fig. 4.24(b)), where the lasing mode shifts from 1548.1 nm and 1549.6 nm for 20°C and 35°C respectively.

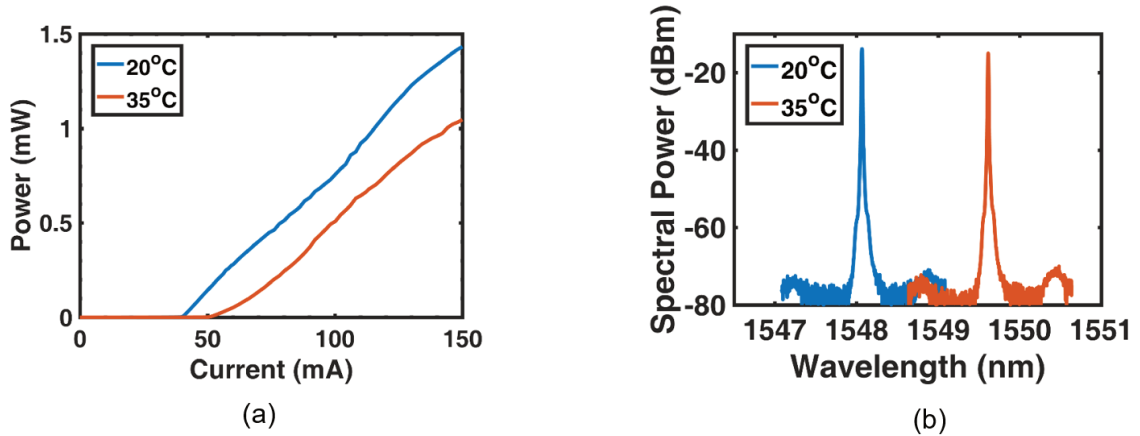


Figure 4.24: Solitary Characteristics of a hybrid III-V/Si DBF Laser at  $I = 141$  mA for  $T = 20^\circ\text{C}$  and  $35^\circ\text{C}$  (a) L-I curve and (b) Optical Spectrum .

#### 4.2.2 High-speed Test Bed Experimental Set-up

Fig. 4.25 represents the test-bed utilized to conduct the direct modulation measurements. The long feedback path was created using a back-reflector (BKR) module, equivalent to a mirror with variable losses in order to generate the different feedback strengths. A 50/50 splitter was used to send 50% of the light to the BKR and the remaining 50% was amplified with an EDFA and analyzed by both the error detector and oscilloscope before and after transmission through a 10 km fiber coil. A pseudo-random bit sequence (PRBS) of 31 bits bit error rate (BER) transmission stress pattern was used with 2 V pp amplitude to estimate the BER output at 10 Gb/s.

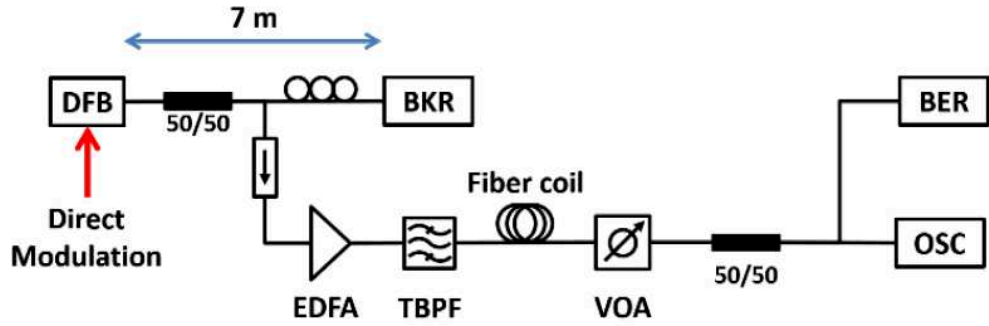


Figure 4.25: Experimental set-up used for optical feedback investigation.

The optical spectra of the hybrid III-V/Si DFB at the two different temperatures 20°C and 35°C when subject to different feedback strengths are displayed in fig. 4.26. At  $T = 20^\circ\text{C}$ , the laser exhibits a stable operation for low feedback ratios as seen in fig. 4.26(a); however, depending on the phase condition, the laser's output can exhibit small broadening of the spectrum as demonstrated in fig. 4.26(b) where relaxations oscillation are clearly observed. For a higher temperature value of  $T = 35^\circ\text{C}$ , the same behavior is demonstrated as depicted in fig. 4.26(c) but a slight shift in the wavelength occurs as evidenced in fig. 4.26(d). Overall, fig. 4.26 shows that the hybrid III-V/Si DFB laser remains mostly stable at low levels of feedback strengths; however, a small shift corresponding to the FP modes is observed without a sign of significant spectral broadening until stronger optical feedback is applied.

Fig. 4.27 and 4.28 illustrate the Continuous Wave (CW) operation of the device. The cartography of the feedback sensitivity in the optical domain as a function of the feedback strength and the optical spectrum are depicted in fig. 4.27(a) and (b) respectively. The green dotted line in fig. 4.27(a) at about -16 dB equivalent to about 2.5% of the injected optical feedback indicates the static critical feedback level,  $r_{crit}$  at which the laser begins to destabilize. From this value on, the laser exhibits undamping of the relaxation oscillations, which strongly affects the laser modulation performance [20].

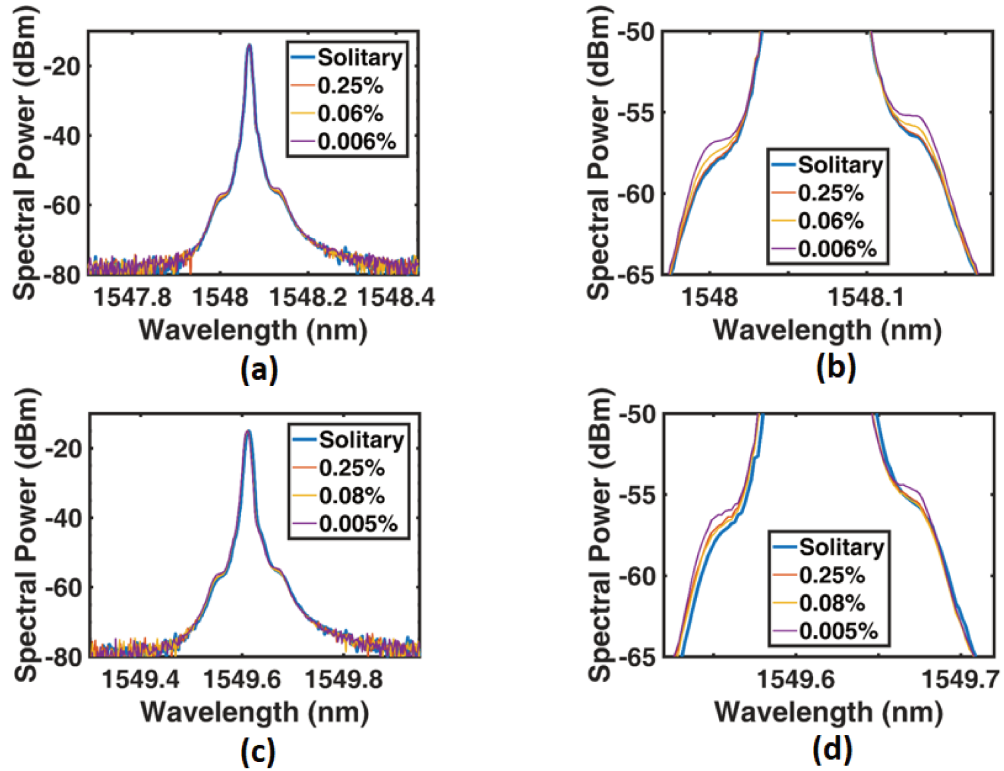


Figure 4.26: Optical Spectra of the hybrid III-V/Si DFB device at 20°C and 35°C under different feedback strengths: (a). Full spectrum, at  $T = 20^\circ\text{C}$ ; (b) Zoomed-in spectrum at  $T = 20^\circ\text{C}$ ; (c) Full shifted spectrum, at  $T = 35^\circ\text{C}$  and; (d) Zoomed-in shifted spectrum at  $T = 35^\circ\text{C}$ .

Fig. 4.27(b) provides the full spectrum of the device with and without optical feedback. The wavelength in the absence of feedback is denoted by the black curve and in the presence of 3.81% of the injected optical feedback equivalent to -14.2 dB optical feedback strength, the response of the device is depicted in blue. In these two figures, the exaltation of the relaxation oscillation is distinctly present and the enhanced peaks with a broader spectrum within the chaotic state are clearly observed. Therefore, depending on the phase condition, the laser's output may exhibit a stable or single frequency emission with a narrow linewidth or a strong mode-hopping phenomena. Fig. 4.27(c) and (d) display the feedback sensitivity of the device in the frequency domain as a function of the feedback strength and the frequency spectrum, respectively. In fig. 4.27(c) several modes can be observed at the beginning of the CC reaching frequency values close to 14 GHz and as  $r_{ext}$  increases the

electrical response in fig. 4.27(d) depicts a higher destabilization of the device as indicated in blue and low-frequency peaks in the absence of optical feedback as indicated by the black curve.

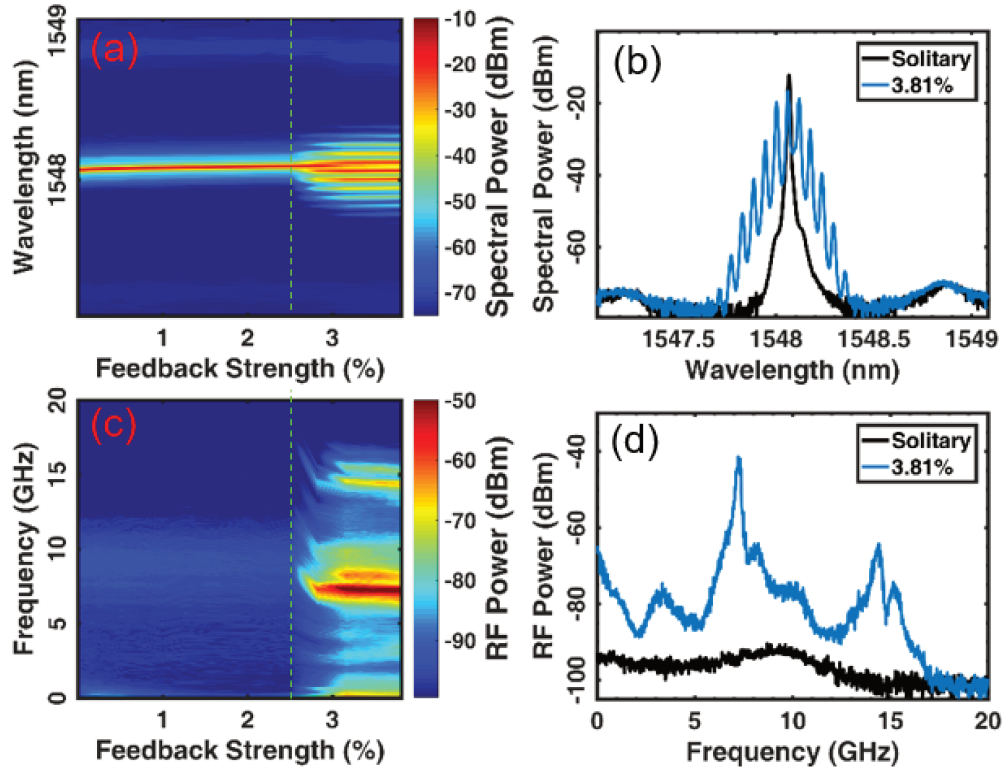


Figure 4.27: Critical feedback at 20°C: (a) Feedback sensitivity in the optical domain; (b) Optical Spectrum; (c) Feedback sensitivity in the frequency domain and; (d) RF spectrum. The green dotted line at about -16 dB equivalent to about 2.5% of the injected optical feedback indicates the static critical feedback level,  $r_{crit}$  at which the laser begins to destabilize.

The same measurements of the optical and frequency spectra were recorded for  $T = 35^\circ\text{C}$ , where similar behavior was also observed. However, in this case, the static critical level,  $r_{crit}$  at which the laser begins to destabilize when operating at a higher temperature is around 2.2% as denoted by the green dotted line in fig. 4.28(a). Fig. 4.28(b) provides the full optical spectrum of the device with and without optical feedback. The wavelength in the absence of feedback is denoted by the black curve and in the presence of 3.02% of the injected optical feedback, the response of the device is depicted in blue indicating

the that this type of device is susceptible to thermal variations above room temperature, which can significantly affect the transmission capability as demonstrated in the following section. Fig. 4.28(c) and (d) display the feedback sensitivity of the device in the frequency domain as a function of the feedback strength and the frequency spectrum, respectively. In fig. 4.28(c), fewer modes are observed at the beginning of the CC and the dominant mode can reach a frequency value of close to 7 GHz. This information can also be deduced from fig 4.28(d) where the frequency response in the presence of optical feedback is denoted by the blue curve and the low-frequency peaks denoted by the black curve represents the experimental response of the device in the absence of optical feedback. The shift in the mode between fig. 4.27(b) and 4.28(b) is clearly observed as previously depicted in fig. 4.24(b).

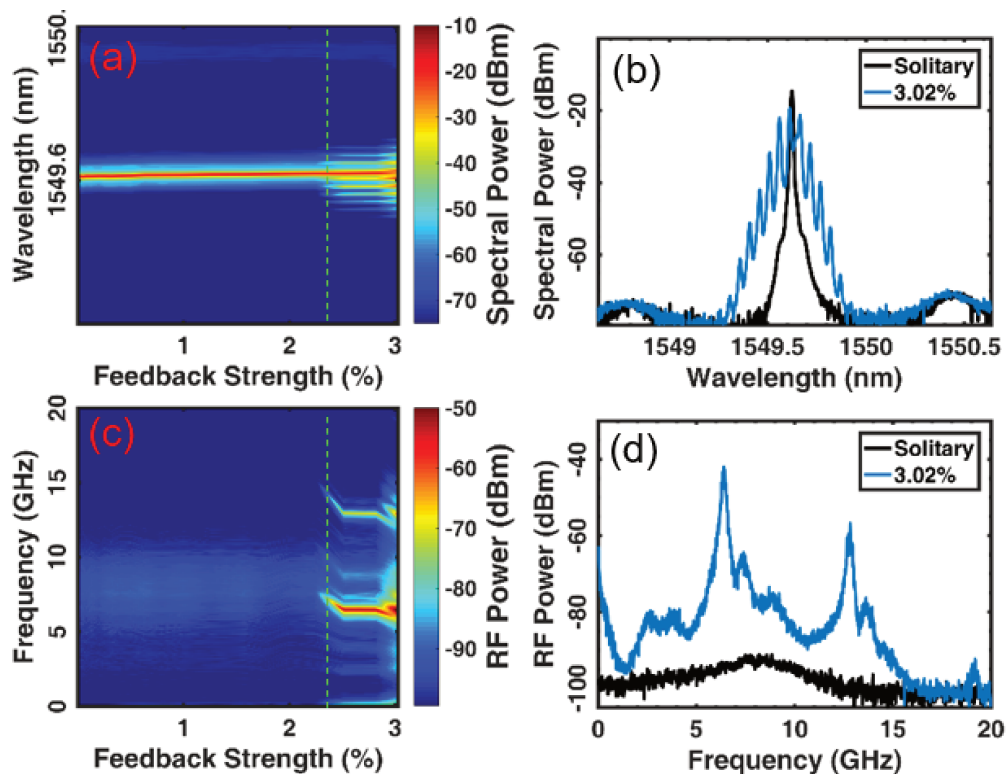


Figure 4.28: Critical Feedback at 35°C: (a) Feedback sensitivity in the optical domain; (b) Optical Spectrum; (c) Feedback sensitivity in the frequency domain and; (d) RF spectrum. The green dotted line is equivalent to about 2.2% of the injected optical feedback indicates the static critical feedback level,  $r_{crit}$  at which the laser begins to destabilize.

With the increase of  $r_{ext}$  the rate of mode-hopping decreases until the transition to regime III, where the laser restabilizes and operates on the mode with the minimum linewidth. This regime is insensitive to the phase of the delayed field, as already pointed out in Chapter III. However, this regime occurs in a very small window of operation, which makes it extremely difficult to observe, especially at low output powers [21]. Fig. 4.27 and 4.28 illustrate the difficulties to locate such a regime. Based on these observations we can then say that these figures certainly illustrate the impact of the oscillation frequencies on the transmission characteristics of the device as demonstrated in the following section, which should be minimized in order to avoid errors and floors when the laser is subject to direct modulation and optical feedback.

#### 4.2.3 Eye Diagram and Bit Error Rate

In this section the effects of the temperature differential in the BER and power penalty degradation are investigated for the first time. Fig. 4.29(a)-(b) and fig, 4.29(c)-(d) represent the eye diagrams of the directly-modulated DFB laser at 10 Gbps under solitary conditions (i.e. without optical feedback), before and after propagation through a 10 km fiber coil at  $T = 20^{\circ}\text{C}$  and  $35^{\circ}\text{C}$ , respectively. In this scenario, a PRBS of 31 bits BER transmission stress pattern is used to estimate the BER output. Fig 4.29(a) clearly shows that the eye is very opened when measured back to back and then it starts to compress after the transmission has occurred as illustrated in fig. 4.29(b), which then decreases the extinction ratio. The overshoots in the intensity output are also well suppressed after transmission. Similar behavior is encountered at a higher temperature. Fig. 4.29(c) shows the eye opened; however, after transmission a significant shrinking of the eye occurs and the overshooting is also suppressed as exemplified in fig. 4.29(d).

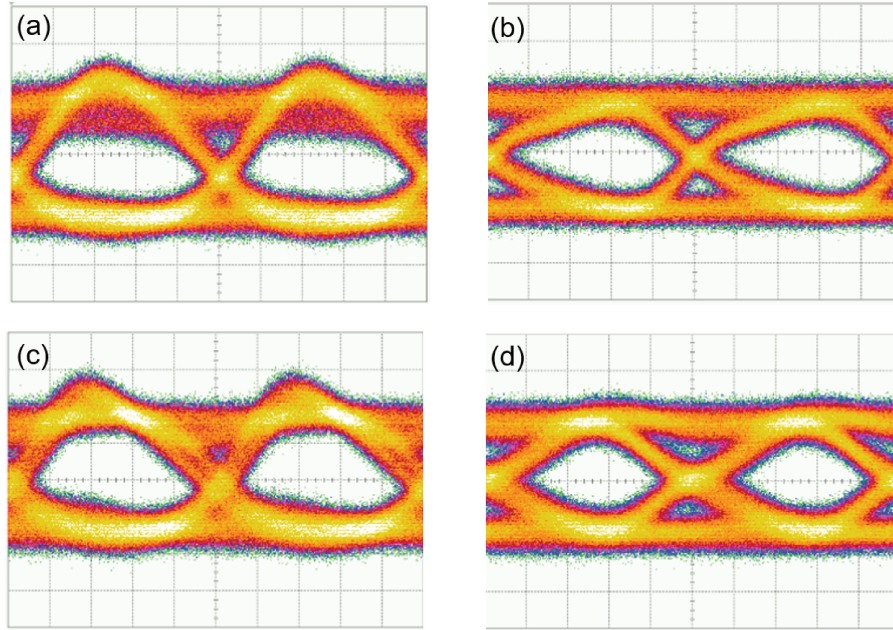


Figure 4.29: Eye diagrams in (a) back-to-back (solitary) for  $T = 20^{\circ}\text{C}$ , (b) after 10 km transmission (solitary)  $T = 20^{\circ}\text{C}$ , (c) back-to-back (solitary) for  $T = 35^{\circ}\text{C}$ , (d) after 10 km transmission (solitary)  $T = 35^{\circ}\text{C}$  .

Fig. 4.30 reveals the BER plots measured at different feedback strengths after transmission. In fig. 4.30(a), the plot measured without optical feedback (red) is used as the reference and unveils a 10-Gbps transmission without penalty and BER floor. While introducing the feedback to the stage, the BER increases due to the optical feedback induced noise into the laser cavity. At the maximum feedback level (-26 dB), an error-free transmission is still achieved with a power penalty below 1.5 dB at  $10^{-9}$  BER. Note that -26 dB optical feedback strength corresponds to the critical level at which the transmission starts being degraded due to the enhanced relaxation oscillations. Certainly, the static critical feedback level originally estimated at -16 dB from Fig. 4.28(a) is actually decreased by the modulation down to -26 dB [22]. Fig. 4.30(b) illustrates the transmission result at a higher temperature ( $35^{\circ}\text{C}$ ) for an optical feedback level of -33 dB, which corresponds to the critical feedback level for this experimental condition. Results confirm that a 10 Gbps floor-free transmission is still preserved with a power penalty still much below 1 dB.

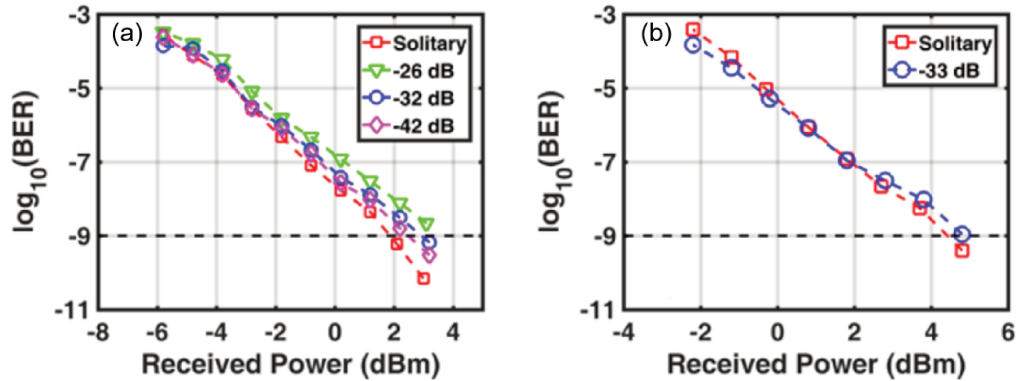


Figure 4.30: Bit Error Rate plots after 10-km transmission distance at different optical feedback strengths for (a)  $T = 20^{\circ}\text{C}$ , (b)  $T = 35^{\circ}\text{C}$ .

Measurements were conducted on the same device by direct modulation at 2.5 Gbps for a 25 km transmission distance at room temperature with different feedback conditions. The results reported in [23] also show that the long delay optical feedback degrades the B2B and the transmission with a power penalty of less than 1.5 dB for a return loss of more than -10.5 dB.

### 4.3 Conclusions

In this chapter two significant achievements have been successfully reported:

1. The existence of internal reflections within hybrid III-V/Si SCLs
2. Manipulation of the chaos bandwidth through the use of short and long delay feedbacks

The FP configurations in Sections 4.1.1 and 4.1.2 exhibited extreme sensitivity to external optical feedback. In the first laser, this sensitivity translates into complex modal behaviors. If the FP laser were to be used in a PIC, any component reflecting light towards it within the microchip would thus greatly affect its operation. Modal competition being suppressed in the TUL, this instability appeared as strong periodic oscillations of the total output power of the laser. The results obtained indicate that these two devices are significantly affected by

sub-cavities in the Si waveguides, which are however extremely difficult to detect without being able to individually examine the various sections of the laser corresponding to a transition from one waveguide to the other. Nevertheless, the first two scenarios of the hybrid III-V/Si lasers studied demonstrate that the combination of an involved laser design with external perturbations indeed leads to complex behaviors.

In addition, the characterization of the DFB structure studied in Section 4.1.3, demonstrates that a combination of short and long-cavity feedback can be successfully used to generate chaotic dynamics in this type of device and also to tune the chaos bandwidth. The dynamics of hybrid III-V/Si SCLs under such combination of feedbacks show the high potential to achieve passive chaos bandwidth enhancement in PICs.

As the wide bandwidth relies primarily on the large ROF of the laser, the design of the device is extremely important and for these applications QW sources may be more appealing than QD sources as QW lasers generally exhibit much higher ROFs than QD devices. In the case of Si PIC applications, the design of the Si waveguides is also very important, since all possible sources of reflections within the PIC will affect the dynamics of the laser. In this work, at least two feedback cavities allow pushing the ROF towards the values reported here: the cavity created by the cleaved fiber, but also the internal parasitic sources of feedback which seem to enhance the ROF of the free-running laser. If sources of feedback are inevitable in a PIC, they can thus be designed to potentially enhance the laser's operation instead of hindering it. Depending on the type of fiber used, the short-cavity feedback can either be enhanced or suppressed. By varying the phase of the short feedback and strength of the long one, the chaos enhancement can be controlled based on the desired application.

Furthermore, Section 4.2 investigates the performance of the DFB laser directly modulated at 10 Gbps directly modulated under different optical feedback strengths. The dynamical properties of the device were carefully analyzed in a B2B configuration and after a 10 km transmission distance. Results obtained demonstrated a power penalty degradation

of less than 1.5 dB at maximum feedback making these transmitters very promising for isolator-free applications such as metro, access networks and PICs. Similar efforts have also been carried out to characterize a high Quality  $Q$  hybrid III-V/Si DFB under direct and external modulation as discussed in the following chapter.

## REFERENCES

- [1] G. Kurczveil, P. Pintus, M. J. R. Heck, J. D. Peters, and J. E. Bowers, “Characterization of insertion loss and back reflection in passive hybrid silicon tapers,” *IEEE Photonics Journal*, vol. 5, no. 2, pp. 6 600 410–6 600 410, 2013.
- [2] A. Argyris, M. Hamacher, K. E. Chlouverakis, A. Bogris, and D. Syvridis, “Photonic integrated device for chaos applications in communications,” *Physical Review Letters*, vol. 100, no. 19, 2008.
- [3] A. Uchida, K. Amano, M. Inoue, K. Hirano, S. Naito, H. Someya, I. Oowada, T. Kurashige, M. Shiki, S. Yoshimori, K. Yoshimura, and P. Davis, “Fast physical random bit generation with chaotic semiconductor lasers,” *Nature Photonics*, vol. 2, no. 12, pp. 728–732, 2008.
- [4] A. Uchida, *Optical communication with chaotic lasers: Applications of nonlinear dynamics and synchronization*. Wiley-VCH, 2012, ISBN: 9783527408696.
- [5] J. Ohtsubo, *Semiconductor lasers*. Springer Berlin Heidelberg, 2013.
- [6] J. Wang, M. Haldar, L. Li, and F. Mendis, “Enhancement of modulation bandwidth of laser diodes by injection locking,” *IEEE Photonics Technology Letters*, vol. 8, no. 1, pp. 34–36, 1996.
- [7] J. Zhao, D. Lenstra, R. Santos, M. J. Wale, M. K. Smit, and X. J. Leijtens, “Stability of a monolithic integrated filtered-feedback laser,” *Optics Express*, vol. 20, no. 26, B270, 2012.
- [8] S. Chen, W. Li, J. Wu, Q. Jiang, M. Tang, S. Shutts, S. N. Elliott, A. Sobiesierski, A. J. Seeds, I. Ross, P. M. Smowton, and H. Liu, “Electrically pumped continuous-wave III–V quantum dot lasers on silicon,” *Nature Photonics*, vol. 10, no. 5, pp. 307–311, 2016.
- [9] V. Kovanis, A. Gavrielides, and P. Alsing, “Taming chaos in semiconductor lasers subject to optical feedback,” in *Proceedings of LEOS 93*, IEEE.
- [10] G.-H. Duan, C. Jany, A. L. Liepvre, A. Accard, M. Lamponi, D. Make, P. Kaspar, G. Levaufre, N. Girard, F. Lelarge, J.-M. Fedeli, A. Descos, B. B. Bakir, S. Messaoudene, D. Bordel, S. Menezo, G. de Valicourt, S. Keyvaninia, G. Roelkens, D. V. Thourhout, D. J. Thomson, F. Y. Gardes, and G. T. Reed, “Hybrid III-V on silicon lasers for photonic integrated circuits on silicon,” *IEEE Journal of Selected Topics in Quantum Electronics*, vol. 20, no. 4, pp. 158–170, 2014.

- [11] P. Dong, Y.-K. Chen, G.-H. Duan, and D. T. Neilson, “Silicon photonic devices and integrated circuits,” *Nanophotonics*, vol. 3, no. 4-5, 2014.
- [12] B. R. Cemlyn, M. J. Adams, I. D. Henning, and D. Labukhin, “Detuning boundaries of linear and nonlinear dynamics in a system of coupled lasers,” *IEEE Journal of Selected Topics in Quantum Electronics*, vol. 21, no. 6, pp. 514–521, 2015.
- [13] L. A. Coldren, S. W. Corzine, and M. L. Mašanović, *Diode lasers and photonic integrated circuits*. John Wiley & Sons, Inc., 2012.
- [14] D. Tauber and J. E. Bowers, “Dynamics of wide bandwidth semiconductor lasers,” *International Journal of High Speed Electronics and Systems*, vol. 08, no. 03, pp. 377–416, 1997.
- [15] S. Azouigui, B. Dagens, F. Lelarge, J.-G. Provost, D. Make, O. L. Gouezigou, A. Accard, A. Martinez, K. Merghem, F. Grillot, O. Dehaese, R. Piron, S. Loualiche, Q. Zou, and A. Ramdane, “Optical feedback tolerance of quantum-dot- and quantum-dash-based semiconductor lasers operating at 1.55  $\mu\text{m}$ ,” *IEEE Journal of Selected Topics in Quantum Electronics*, vol. 15, no. 3, pp. 764–773, 2009.
- [16] K. Schires, N. Girard, G. Baili, G.-H. Duan, S. Gomez, and F. Grillot, “Dynamics of hybrid III-v silicon semiconductor lasers for integrated photonics,” *IEEE Journal of Selected Topics in Quantum Electronics*, vol. 22, no. 6, pp. 43–49, 2016.
- [17] V. Kovanis, “Instabilities and chaos in semiconductor lasers with optical injection,” in *LEOS 95. IEEE Lasers and Electro-Optics Society 1995 Annual Meeting. 8th Annual Meeting. Conference Proceedings*, IEEE.
- [18] T. B. Simpson, J. M. Liu, A. Gavrielides, V. Kovanis, and P. M. Alsing, “Period-doubling cascades and chaos in a semiconductor laser with optical injection,” *Physical Review A*, vol. 51, no. 5, pp. 4181–4185, 1995.
- [19] K. Kechaou, F. Grillot, J.-G. Provost, B. Thedrez, and D. Erasme, “Self-injected semiconductor distributed feedback lasers for frequency chirp stabilization,” *Optics Express*, vol. 20, no. 23, p. 26 062, 2012.
- [20] F. Grillot, B. Thedrez, J. Py, O. Gauthier-Lafaye, V. Voiriot, and J. Lafrayette, “2.5-gb/s transmission characteristics of 1.3- $\mu\text{m}$  DFB lasers with external optical feedback,” *IEEE Photonics Technology Letters*, vol. 14, no. 1, pp. 101–103, 2002.
- [21] R. Tkach and A. Chraplyvy, “Regimes of feedback effects in 1.5- $\mu\text{m}$  distributed feedback lasers,” *Journal of Lightwave Technology*, vol. 4, no. 11, pp. 1655–1661, 1986.

- [22] H. Su, L. Zhang, A. Gray, R. Wang, T. Newell, K. Malloy, and L. Lester, “High external feedback resistance of laterally loss-coupled distributed feedback quantum dot semiconductor lasers,” *IEEE Photonics Technology Letters*, vol. 15, no. 11, pp. 1504–1506, 2003.
- [23] A. Gallet, K. Schires, H. Huang, M. Song, A. Accard, D. Make, S. Olivier, G.-H. Duan, and F. Grillot, “Long delay optical feedback sensitivity of hybrid III-v/SOI directly modulated DFB lasers,” in *2017 IEEE 14th International Conference on Group IV Photonics (GFP)*, IEEE, 2017.

## CHAPTER 5

### HYBRID III-V/SI DISTRIBUTED FEEDBACK LASER WITH HIGH QUALITY FACTOR

Very recently, multiple solutions to reach optical feedback insensitivity have been investigated. For instance, a new type of optical feedback insensitive integrated semiconductor ring laser was introduced with an optical isolator included in the optical cavity [1]. However, despite the observed 5 dB of isolation and 3 dB increase of tolerance for external optical feedback, the gain in terms of feedback insensitivity is quite limited due to a very complex structure where additional parasitic reflections may occur [1].

In order to maintain a much simpler laser design, other configurations can be considered such as those based on nano-lasers [2] or QD material systems [3]. In the former configuration, it was shown that such nano-devices can strongly suppress the dynamic instabilities induced by external optical feedback in spite of a limited optical output power. Interestingly, owing to a unique reduction of the ROF characteristics, a possible total suppression of the CC associated to chaotic oscillations was pointed out [2]. In the latter configuration, it was demonstrated that QD lasers with robust single-state emission, large damping and low linewidth enhancement factor are powerful candidates capable of reaching a high level of feedback insensitivity [4, 5]. In case of epitaxial lasers on silicon, this effect can be further accelerated due to the epitaxial defects which may contribute to reduce the carrier lifetime [6, 7]. At the system level, an InAs/GaAs QD transmitter integrated on Si substrate without optical isolator was proposed for core I/O applications with a 25 Gbps floor-free transmission [8]. In addition to that, other efforts are steered towards the feedback insensitivity by considering a semiconductor laser cavity having a resonator with a high quality ( $Q$ ) factor [9].

In this chapter the high-speed dynamics of an externally modulated high coherence hybrid III-V/Si DFB SCL heterogeneously integrated onto Si is experimentally investigated in the presence of external optical feedback at different temperature conditions to evaluate its sensitivity. The impact of these two parameters on the BER and power penalty degradation is also analyzed and carefully investigated. Pioneering efforts have already been proposed in the context of narrow phase noise measurements where a high- $Q$  passive Si resonator has also evidenced superior robustness against optical feedback [10].

The work presented in this section builds up on these prior efforts by considering a low-noise hybrid laser, which is based on the same design concept hence a high- $Q$  factor III-V on Si device consisting of a harmonic optical potential well cavity. Fig. 5.1 compares the relative intensity noise (RIN) of a standard  $\lambda/4$  phase shift hybrid DFB against the high- $Q$  device under investigation measured at a bias current of 120 mA [11].

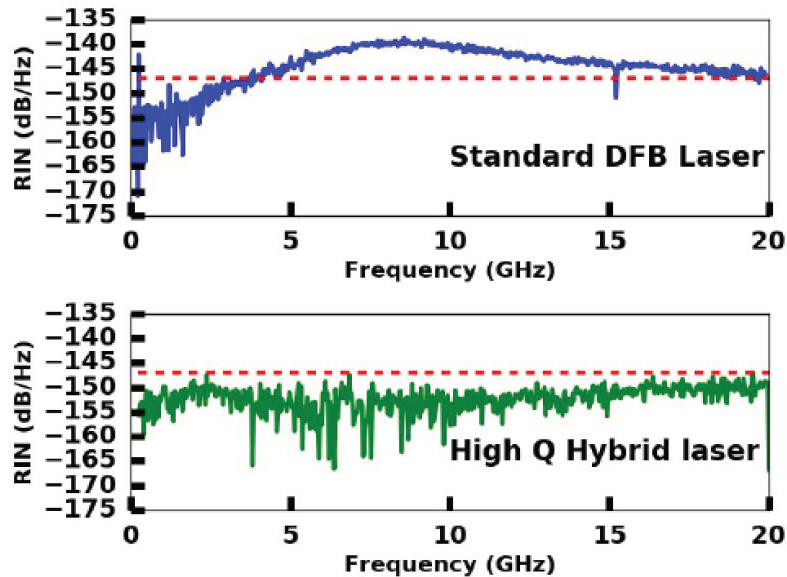


Figure 5.1: Relative intensity noise measurements at bias current of 120 mA with similar threshold values for: (a) A standard  $\lambda/4$  phase shifted hybrid DFB laser design (top) and a high- $Q$  hybrid laser (bottom) [11].

A flat RIN with level below 147 dB/Hz with a constant level over 20 GHz can be observed in the high- $Q$  device with a slight increase due to the  $f_r$ . In this work, the optical feedback investigation is performed in greater depth including a side by side comparison against

existing technologies based on QWs. In [12], a photon lifetime as high as 100 ps has already been reported. The fabrication of the novel laser under investigation relies on proper modal engineering [13] in which light is generated in the III-V material and stored in the low-loss Si region in order to substantially enhance the quality factor of the cavity resonator. The results presented here successfully demonstrate a floor-free transmission at 10 Gbps under optical feedback with a power penalty below 2 dB, thereby paving the way to isolator-free PICs. In addition, a qualitative interpretation is also provided by linking the standard feedback equations to the quality factor of the resonator.

### 5.1 Device Under Study

The device under investigation is a hybrid III-V/Si high- $Q$  DFB laser made in the 500/300 nm SOI standard platform of LETI. Fig. 5.2(a) illustrates the cross section of the high- $Q$  laser structure, bonding a Si photonic layer onto a QW gain material. The geometry is optimized in such a way that the mode is buried into a rib Si waveguide with a shallow grating of 30 nm deep teeth. The width of the grating is tapered longitudinally to create an effective confining potential which allows a single, bell-shaped longitudinal mode within the stop band of the DFB [9]. It has been demonstrated that this mode has a large internal  $Q$  factor leading to a cavity photon lifetime of  $\sim 100$  ps. The  $Q$  factor term is an alternative description of the laser's losses meaning that high- $Q$  lasers are simply low-loss devices. In order to harness the low internal loss of the Si resonator, the contribution to loss from the active material has to then be reduced, by decreasing the overlap between the optical field and the gain material. The modal gain is decreased as well, but it remains large enough to compensate for losses. The choice of a large Si waveguide with width  $W_{Si} = 2 \mu\text{m}$  leads to the desired overlap of about 5% as shown in fig. 5.2(b).

The mirror losses, more precisely the coupling rate of the cavity to the output is adjusted to ensure mild overcoupling, hence improving differential efficiency without increasing the threshold. The total length of the cavity consist of three sections as illustrated in fig. 5.3

[11]. The first section corresponds to the parabolic tapered grating with length  $L_c$  and the other two are related to uniform sections at each side with length  $L_b$ . The total cavity length  $L = 2L_b + L_c$  is varied from 400 to 900  $\mu\text{m}$ .

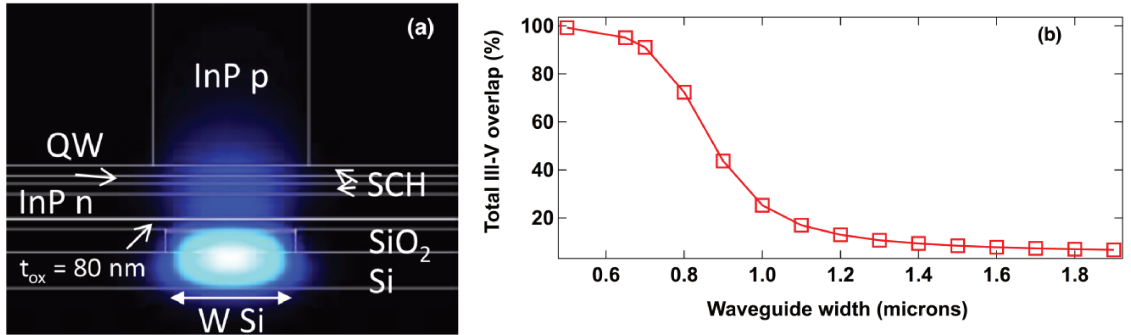


Figure 5.2: (a) Schematic of the high- $Q$  DFB laser cross-section; (b) III-V total overlap versus Si waveguide width

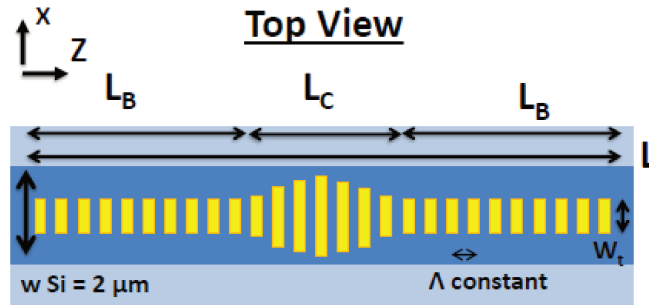


Figure 5.3: Top view of of the high- $Q$ . The 300 nm slab is in light blue, the 500 nm waveguide in darker blue and the 30 nm tooth etched regions in yellow. The grating has two regions: a parabolic tapered grating in the centre and a uniform grating at each side

The inset of fig. 5.4(a) depicts the light-current (L-I) characteristics of the free-running device having a total cavity length of 900  $\mu\text{m}$ . The threshold current  $I_{th}$  is close to 40 mA at room temperature (293K) whereas the optical spectrum in fig. 5.4(a) confirms the single mode behavior with a SMSR  $> 50 \text{ dB}$  at  $3 \times I_{th}$  (114 mA) and a dominant emission wavelength of 1562.6 nm. In this fabrication, the internal  $Q$  factor is maximized by increasing the device length hence allowing a stronger grating coupling coefficient at the center of the cavity ( $\approx 200 \text{ cm}^{-1}$ ) and a large cavity photon lifetime. Fig. 5.4(b) shows that  $Q$  can reach

up to  $4 \times 10^5$  when  $W_{Si}$  is increased to 2 microns, which results in a substantial reduction of the threshold current.

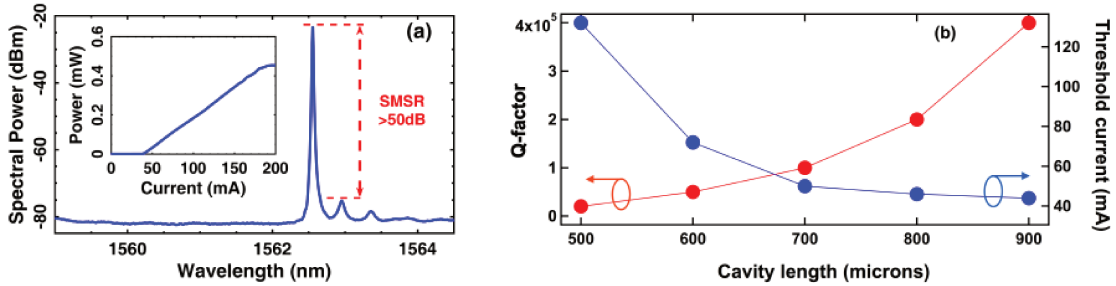


Figure 5.4: (a) Optical spectrum of the high- $Q$  DFB laser and L-I curve (inset) at  $3 \times I_{th}$ ; (b) The calculated  $Q$  factor and threshold current as a function of the total cavity length.

Let us stress that the latter saturates since increasing the cavity length also decreases the carrier density for the same injected current. Here, the  $Q$  is computed by evaluating the DFB loss and the III-V overlap with the Si waveguide as well as with the  $p$  and  $n$  doped InP regions ((5.2(b)). The former analysis is performed with the Transfer Matrix Method (TMM) [14] whereas the latter is conducted using to a commercial software [15].

Fig. 5.5(a) depicts the L-I characteristics of the free-running device captured at different temperatures ( $20^\circ\text{C}$ ,  $25^\circ\text{C}$ ,  $30^\circ\text{C}$  and  $35^\circ\text{C}$ ) corresponding to  $I_{th} = 38, 41, 44, 47$  mA respectively. The thermal variation on the high- $Q$  lasers causes a shift on the threshold value.

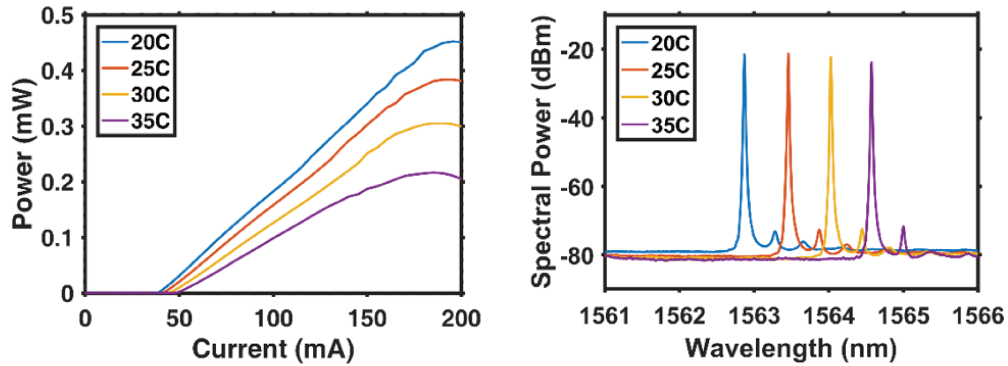


Figure 5.5: High- $Q$  DFB laser at  $T = 20^\circ\text{C}$ ,  $25^\circ\text{C}$ ,  $30^\circ\text{C}$ , and  $35^\circ\text{C}$ : (a) L-I curve; (b) Optical spectrum

It is also observed that the laser efficiency falls off with increasing temperature. At the highest temperature, the maximum output power drops from 0.45 mW down to 0.2 mW and the threshold level is approximately 10 mA higher than the room temperature value. The optical spectrum displayed in fig. 5.5(b) confirms the single mode operation of the high- $Q$  hybrid laser with SMSR consistently greater than 50 dB at  $3 \times I_{th}$  for all temperature values with minimum relaxation oscillation. However, as temperature rises, the laser's dominant emission wavelength shifts concurrently:  $\lambda = 1562.6, 1563.5, 1564.2$  and  $1564.6$  nm respectively. Temperature variations affect the bandgap of the SCL junction and therefore, the peak wavelength of the gain profile. However, for this particular device, thermal differentials do not impact the BER and floor-free transmission is still achievable as demonstrated in Section 5.3.

## 5.2 Optical Feedback Set-up

Fig. 5.6 represents the experimental setup used to investigate the effects of optical feedback under both static and dynamic configurations. The emission from the SCL is coupled by a lens-end fiber with AR coating. A 90/10 splitter is used to send 90% of the coupled light to the BKR in order to control the feedback amount, which, on this stage, ranges between 0 to about 4% of the emitting power, i.e. the maximal attainable amount of feedback is -14 dB. In the following, the feedback strength  $r_{ext}$  defined as the ratio between the reflected power and the free-space emitting power at the front facet is normalized to the maximal level, hence ranging from 0 to 100%. The 7-meter long external cavity length (corresponding to  $\tau_{ext} = 0.70$  ns) implies a long-delay feedback scenario, meaning that the effects associated with the phase of the back-reflected field can be neglected. The remaining 10% is amplified with an EDFA and filtered by a thin band-pass filter (TBPF). A second 90/10 splitter is also used to send 10% of this light to the PM, OSA and ESA to monitor the coupled light via an optical switch (SWT). The remaining 90% is then modulated by a Mach-Zehnder modulator (MZM) and analyzed by both the error detector (ED) and oscilloscope (OSC) before

and after transmission through a 10 km fiber coil. A PRBS of 31 bits BER transmission stress pattern is used with 2 V<sub>pp</sub> amplitude to estimate the BER output at 10 Gbps.

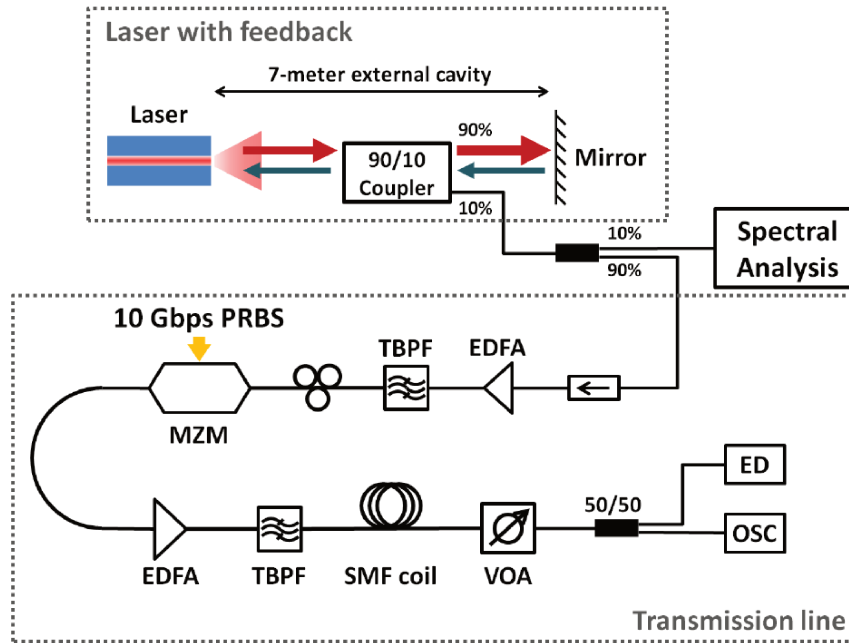


Figure 5.6: Experimental set-up used for optical feedback investigation.

### 5.3 Results and discussion

In what follows, the experiments are all performed at room temperature and at three times the threshold. Fig. 5.7 illustrates the optical and electrical spectra maps of the high- $Q$  DFB laser. Fig. 5.7(a) unveils a steady operation of the device under a variation of optical feedback strengths. In this case, the device does not exhibit any perturbations up to  $r_{ext} = 100\%$  (ie., -14 dB), which is indicative of the enhanced tolerance high- $Q$  lasers have against the detrimental effects of parasitic reflections. The electrical spectrum of the device is displayed in fig. 5.7(b) where a stable operation can also be observed without any evidence of ROF often expected from a precursor regime associated with the CC operation. This last statement is in agreement with the very long photon lifetime and large damping factor already reported in [12].

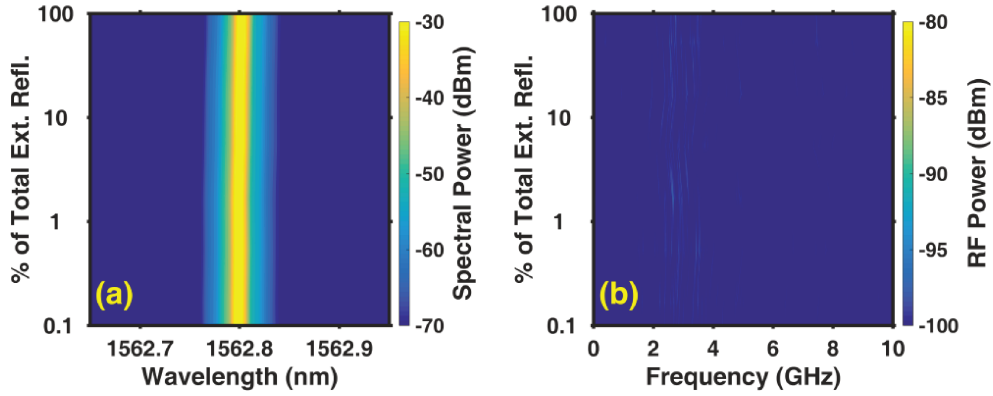


Figure 5.7: (a) Optical and (b) electrical spectral map of the high- $Q$  DFB laser with respect to the optical feedback strength.

As a reference, fig. 5.8(a) and 5.8(b) displays the optical and radio frequency (RF) spectral evolution of a conventional QW DFB laser. The total reflection ratio is kept at the same level as in the high- $Q$  DFB laser to quantitatively assess the strengths and limitations exhibited by these two types of structures. As we can see, the strong periodic oscillations displayed by the QW DFB laser during the route to chaos are well pronounced: first, the laser remains stably operating in both the optical and the RF domain, the red shift of the lasing mode visible in fig. 5.8(a) is attributed to the reduction of the carrier density due to the increasing feedback; then as the feedback value reaches 1% of the total reflection, the laser is suddenly destabilized with periodic oscillations gradually raising up.

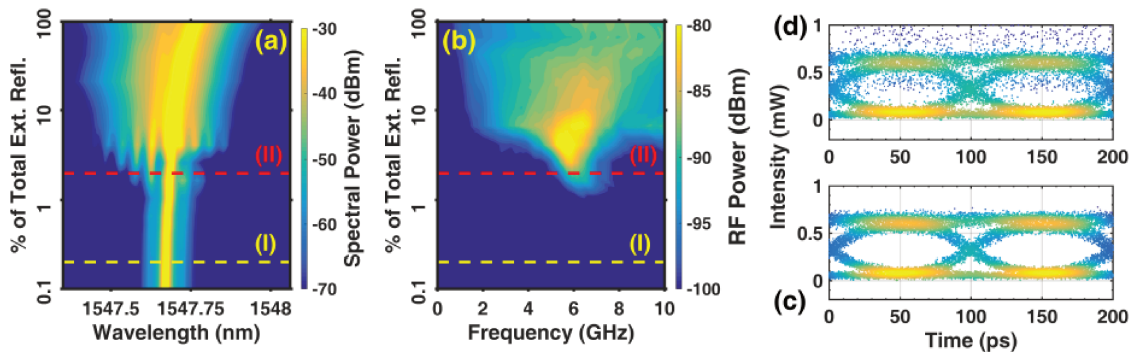


Figure 5.8: (a) Optical and (b) RF spectral map of a conventional QW DFB laser; eye diagrams at (c) level (I) and (d) level (II) marked in the map.

It is also evident that as the feedback strength continues to raise, the lasing operation of the device becomes progressively chaotic which translates into a largely broadened lasing mode and an extended RF signal span in the optical and RF spectra. It is well known that any change in the feedback phase inside the cavity have a significant impact on the overall performance of the QW DFB laser and strongly affects its operation. Under a variation of optical feedback strengths, the relaxation oscillations of a conventional QW DFB device become easily excited subsequently leading to a chaotic oscillation state of the laser's output [16].

Fig. 5.8(c) and fig. 5.8(d) display the eye diagrams under the back-to-back (B2B) configuration (absence of transmission across the optical fiber) for two different feedback levels: (I) where the laser is mostly stable ( $r_{ext} \approx 0.3\%$  (ie., -40 dB)), and (II) at the beginning of destabilization ( $r_{ext} \approx 3\%$  (ie. -30 dB)). At level (I), a clear eye diagram is obtained; as the optical feedback goes beyond level (II), the eye diagram starts to deteriorate due to CC operation which then limits the amount of data transmitted. Although the eye diagrams remains pretty open for both cases, the corresponding BER increases to approximately  $10^{-5}$  at stronger feedback levels thus transmitting such signal through conventional single-mode fibers in an error-free state is no longer possible.

On the other hand, we unveil a much higher tolerance offered by high- $Q$  devices when subject to optical feedback as shown in fig. 5.9. Fig. 5.9 depicts the BER characteristics and the eye diagram of the high- $Q$  DFB laser for the different experimental conditions. In Fig. 5.9(a), the red squares represent the reference curve without the presence of optical feedback, and the blue triangles are obtained when the laser is subject to the maximum feedback (ie.,  $r_{ext} = 100\%$ ) for B2B measurements. After transmissions, floor-free results are also achieved successfully. The magenta squares represent the reference curve for the solitary conditions and the cyan triangles are obtained at the maximum feedback strength. To sum, this work validates that the high- $Q$  factor prevents any degradation of the laser's performance under strong optical feedback conditions without any CC regime operation.

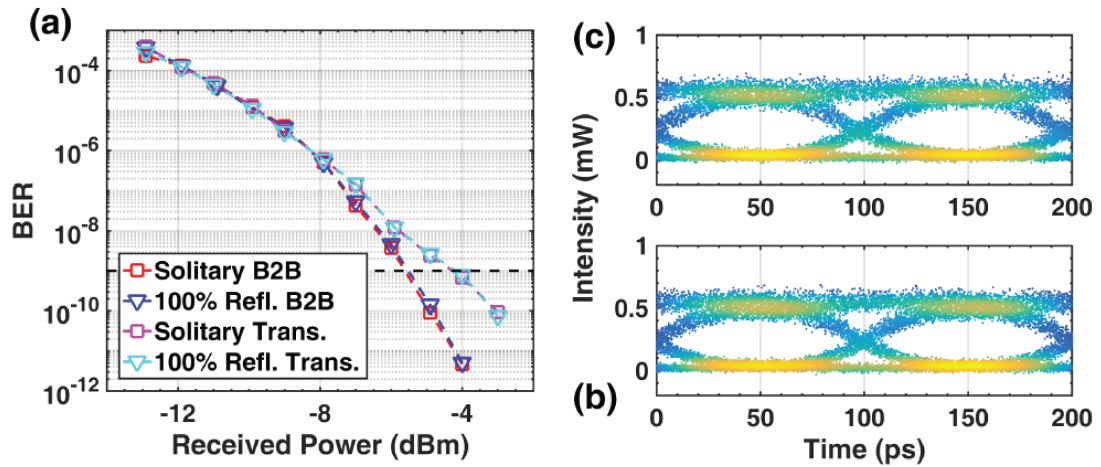


Figure 5.9: (a) BER characteristics of the high- $Q$  laser with (blue and cyan triangles) and without (red and magenta squares) feedback; eye diagrams (b) in B2B without feedback and (c) with maximal feedback after transmission.

Overall, the overlapping curves for both sets of measurements demonstrate that the high- $Q$  hybrid laser's performance is not altered by external feedback and that an error-free transmission can be achieved close to  $10^{-12}$  and  $10^{-10}$  BER for B2B and transmission operation respectively, implying that the power penalty of  $\sim 1.5$  dB is primarily caused by the fiber dispersion during the transmission. Fig. 5.9(b) and 5.9(c) display the eye diagrams for the B2B solitary device and after transmission with maximum feedback. In both diagrams, the eye remains clean and well opened. The results presented herein indicate that high- $Q$  lasers exhibit an enhanced tolerance against optical perturbations and serve as a tool to potentially achieve error-free transmission at higher bit rates.

#### 5.4 Physical interpretation

The improved performance and the relative optical feedback insensitivity powered by this device is due to its unique structural engineering design, which leads to a large quality factor. If  $\omega$  is the laser's angular frequency, the total, internal and external quality factors are:

$$Q = \omega\tau_p = \frac{\omega}{v_g(\alpha_i + \alpha_m)} \quad (5.1)$$

$$Q_i = \frac{\omega}{v_g\alpha_i} \quad (5.2)$$

and

$$Q_e = \frac{\omega}{v_g\alpha_m} \quad (5.3)$$

where  $v_g$  is the group velocity,  $\alpha_i$  the internal loss,  $\alpha_m$  the transmission loss and  $\tau_p$  the cavity photon lifetime. From Equations (5.1), (5.2), and (5.3), it is possible to link  $Q$ ,  $Q_i$ , and  $Q_e$  such that

$$Q^{-1} = Q_i^{-1} + Q_e^{-1} \quad (5.4)$$

The high- $Q$  laser mitigates the losses described above thus increasing the photon lifetime to about 100 ps [12]. It is also noted that  $Q_e$  should not be above  $Q_i$  to keep a reasonable external efficiency. Although the QW overlap can be significantly reduced by the proposed laser design, this doesn't imply a high threshold current as the low QW overlap is balance by low losses. Therefore, the threshold is obtained when the gain compensate the losses such as

$$G(N_{th}) = \Gamma_{QW}G_N(N_{th} - N_{tr}) = \frac{2\pi\nu}{v_gQ} \quad (5.5)$$

$\Gamma_{QW}$  is the QW overlap. Interestingly, this novel laser design, the carrier density at threshold  $N_{th}$  (threshold current) can be reduced by decreasing  $\Gamma_{QW}$ . In order to obtain a high output power, a balance between  $Q_i$  and  $Q_e$  must be achieved to reach an adequate differential efficiency,  $\eta_d$ , which is given by [17]

$$\eta_d = \frac{\hbar\nu}{q} \frac{1}{2} \frac{\alpha_m}{\alpha_i + \alpha_m} = \frac{1}{2} \frac{Q}{Q_e} = \frac{1}{2} \frac{1}{1 + \frac{Q_e}{Q_i}} \quad (5.6)$$

This equation indicates shows that it is not useful to increase  $Q_e$  above  $Q_i$ . In addition, it is known that the external optical feedback induces an angular frequency shift whose expression is given by Equation (3.16). This angular frequency shift can also be expressed as [18]:

$$\Delta\omega\tau_{ext} = -C \sin(\varphi + \tan^{-1} \alpha_H) \quad (5.7)$$

where  $\varphi = \omega_s\tau_{ext}$  is the phase of the feedback wave,  $\tau_{ext}$  the roundtrip time in the external cavity,  $\Delta\omega = \omega - \omega_s$ ,  $\alpha_H$  the linewidth enhancement factor and  $C$  the coupling coefficient expressed as

$$C = \frac{\tau_{ext}}{\tau_{int}} \frac{1-R}{\sqrt{R}} \sqrt{1 + \alpha_H^2 \sqrt{r_{ext}}} \quad (5.8)$$

with  $\tau_{int}$  the photon round trip time within the laser's cavity, and  $R$  the power reflectivity of the output facet coupled to the external cavity. Usually, large values of  $C$  increase the number of external cavity modes giving rise to modal competition where at large feedback strengths leads to the CC regime [19]. By incorporating  $Q_e$  into Equation (5.8),  $C$  can be rewritten as follows

$$C = \omega\tau_{ext}Q_e^{-1} \sqrt{1 + \alpha_H^2 \sqrt{r_{ext}}} \quad (5.9)$$

It is essential to note that this novel equation holds under the assumption that the high- $Q$  laser has a perfect power reflectivity approaching unity hence the quality factor can directly be described as a function of the transmission loss. Despite Equation (5.9) being a limiting case of Equation (5.8), it gives a qualitative insight on how  $Q_e$  impacts the laser's feedback sensitivity. When the external  $Q_e$  factor is large, the  $C$  coefficient can be kept to a low

value thus providing a relative feedback insensitivity regardless of the feedback strength.

On the other hand, it was shown that the onset of the CC can be determined when the frequency shift (Equation 5.4) is maximized or a certain critical feedback level is greater than the ROF such as  $\Delta\omega_{max} \geq \omega_r$  [20]. Using Equation (5.5) and (5.7), the onset of the CC  $r_{crit}$  can be linked to  $Q_e$  such as

$$r_{crit} \geq \left(\frac{\omega_r}{\omega}\right)^2 \frac{Q_e^2}{1 + \alpha_H^2} \quad (5.10)$$

Equation (5.8) unveils that the  $r_{crit}$  of a high- $Q$  laser occurs at a high feedback level. For the laser under study,  $\omega/2\pi = 200$  THz,  $\omega_r/2\pi = 2$  GHz,  $\tau_p = 100$  ps, and  $\alpha_H = 2.5$ . Altogether, it is found  $Q_e = \omega \times \tau_p = 1.2 \times 10^5$  leading to a  $r_{crit}$  beyond -10 dB. This last value corresponds to an upper limit case of the CC level which can not be reached in our experiments due to the loss in the fiberized setup. Despite that, the high stability achieved herein for the high- $Q$  laser shows a high CC level beyond  $r_{ext}=100\%$  (ie.  $> -14$  dB), which corresponds to a strong improvement when compared to the QW DFB laser for which the CC level pops-up at  $r_{ext} = 3\%$  (ie. -30 dB).

## 5.5 Conclusions

To conclude, the dynamics of a high- $Q$  hybrid DFB laser heterogeneously integrated onto Si is experimentally investigated at different temperature values. Results obtained demonstrate that this novel device is found to be inherently less sensitive to optical feedback compared to all their III-V counterparts [21] making these devices excellent candidates for isolator-free applications.

The development of feedback insensitive lasers remain a major challenge for the SiPh integration to alleviate the risk of undesired reflections. The work presented in this chapter shows a step towards achieving light sources with absolute feedback insensitivity paving

the path for the design of single-mode lasers that can function without the need for optical isolators. Optical isolators are bulky and cost prohibitive, therefore, high- $Q$  devices such as the one presented here can be advantageous in terms of footprint and operation cost.

The low  $f_r$  exhibited by this device stems from the high photon lifetime estimated to be  $\tau_p = 103$  ps, which is in agreement with the calculated quality factor. The high damping of the ROF is confirmed by RIN measurements remaining below -147 dB/Hz over 20 GHz. It was observed that the increase in  $I_{th}$  and decrease in the slope efficiency comes from the rise in temperature but as demonstrated, these changes did not affect the overall performance of the device. This unique laser design provides prolonged photon cavity lifetime of the lasing mode due to the material absorption properties. Owing to the large quality factor, a high CC suppression is unveiled which transforms into a 10 Gbps floor-free transmission under the most stringent optical feedback conditions.

The hybrid device under investigation is found to be not susceptible to parasitic reflections with a power penalty not exceeding 1.5 dB at room temperature. These results indicate the vast potential these devices have to serve as an alternative solution for the development of isolator-free applications in future PICs eliminating the need for nonreciprocal devices. This work brings novel findings and insights towards the understanding of efficient semiconductor lasers operating without optical isolator which is of vital importance for integrated photonics technologies since the incorporation of magnetic isolators is not compatible with CMOS manufacturing used to fabricate hybrid III-V/Si lasers [21]. Other applications requiring improved coherence and precisely controlled light sources will be also considered in the future.

## REFERENCES

- [1] D. Lenstra, T. T. M. van Schaijk, and K. A. Williams, "Toward a feedback-insensitive semiconductor laser," *IEEE Journal of Selected Topics in Quantum Electronics*, vol. 25, no. 6, pp. 1–13, 2019.
- [2] T. S. Rasmussen, Y. Yu, and J. Mork, "Suppression of coherence collapse in semiconductor fano lasers," *Physical Review Letters*, vol. 123, no. 23, 2019.
- [3] G. Eisenstein and D. Bimberg, Eds., *Green photonics and electronics*. Springer International Publishing, 2017.
- [4] D. O'Brien, S. Hegarty, G. Huyet, J. McInerney, T. Kettler, M. Laemmlin, D. Bimberg, V. Ustinov, A. Zhukov, S. Mikhlin, and A. Kovsh, "Feedback sensitivity of 1.3 [micro sign]m InAsGaAs quantum dot lasers," *Electronics Letters*, vol. 39, no. 25, p. 1819, 2003.
- [5] H. Huang, L.-C. Lin, C.-Y. Chen, D. Arsenijević, D. Bimberg, F.-Y. Lin, and F. Grillot, "Multimode optical feedback dynamics in InAs/GaAs quantum dot lasers emitting exclusively on ground or excited states: Transition from short- to long-delay regimes," *Optics Express*, vol. 26, no. 2, p. 1743, 2018.
- [6] J. Duan, H. Huang, B. Dong, D. Jung, J. C. Norman, J. E. Bowers, and F. Grillot, "1.3- $\mu$ m reflection insensitive InAs/GaAs quantum dot lasers directly grown on silicon," *IEEE Photonics Technology Letters*, vol. 31, no. 5, pp. 345–348, 2019.
- [7] H. Huang, J. Duan, D. Jung, A. Y. Liu, Z. Zhang, J. Norman, J. E. Bowers, and F. Grillot, "Analysis of the optical feedback dynamics in InAs/GaAs quantum dot lasers directly grown on silicon," *Journal of the Optical Society of America B*, vol. 35, no. 11, p. 2780, 2018.
- [8] K. Mizutani, K. Yashiki, M. Kurihara, Y. Suzuki, Y. Hagihara, N. Hatori, T. Shimizu, Y. Urino, T. Nakamura, K. Kurata, and Y. Arakawa, "Isolator free optical I/O core transmitter by using quantum dot laser," in *2015 IEEE 12th International Conference on Group IV Photonics (GFP)*, IEEE, 2015.
- [9] C. T. Santis, S. T. Steger, Y. Vilenchik, A. Vasilyev, and A. Yariv, "High-coherence semiconductor lasers based on integral high-q resonators in hybrid Si/III-V platforms," *Proceedings of the National Academy of Sciences*, vol. 111, no. 8, pp. 2879–2884, 2014.

- [10] Z. Zhang, H. Wang, N. Satyan, G. Rakuljic, C. T. Santis, and A. Yariv, “Coherent and incoherent optical feedback sensitivity of high-coherence si/III-v hybrid lasers,” in *Optical Fiber Communication Conference (OFC) 2019*, OSA, 2019.
- [11] A. Gallet, K. Hassan, C. Jany, T. Card, J. DaFonseca, V. Rebeyrol, A. Shen, J.-G. Provost, F. V. Dijk, N. Girard, V. Muffato, A. Coquiard, S. Malhouitre, S. Olivier, G. Baili, H. Debregeas, G.-H. Duan, F. Grillot, and A. de Rossi, “Dynamic and noise properties of high-q hybrid laser,” in *2018 IEEE International Semiconductor Laser Conference (ISLC)*, IEEE, 2018.
- [12] A. Gallet, K. Schires, H. Huang, M. Song, A. Accard, D. Make, S. Olivier, G.-H. Duan, and F. Grillot, “Long delay optical feedback sensitivity of hybrid III-V/SOI directly modulated DFB lasers,” in *2017 IEEE 14th International Conference on Group IV Photonics (GFP)*, IEEE, 2017.
- [13] S. T. Steger, “A fundamental approach to phase noise reduction in hybrid Si/III-V lasers,” PhD thesis, California Institute of Technology, 2014.
- [14] G. Bjork and O. Nilsson, “A new exact and efficient numerical matrix theory of complicated laser structures: Properties of asymmetric phase-shifted DFB lasers,” *Journal of Lightwave Technology*, vol. 5, no. 1, pp. 140–146, 1987.
- [15] Fimmwave and Harold.
- [16] K. Petermann, *Laser diode modulation and noise*. Springer Netherlands, 1988.
- [17] J. Buus, M.-C. Amann, and D. J. Blumenthal, *Tunable laser diodes and related optical sources*. Wiley-IEEE Press, 2005, ISBN: 9780471208167.
- [18] J. Ohtsubo, *Semiconductor lasers*. Springer Berlin Heidelberg, 2013.
- [19] F. Grillot, B. Thedrez, J. Py, O. Gauthier-Lafaye, V. Voiriot, and J. Lafrayette, “2.5-gb/s transmission characteristics of 1.3- $\mu\text{m}$  DFB lasers with external optical feedback,” *IEEE Photonics Technology Letters*, vol. 14, no. 1, pp. 101–103, 2002.
- [20] J. Binder and G. Cormack, “Mode selection and stability of a semiconductor laser with weak optical feedback,” *IEEE Journal of Quantum Electronics*, vol. 25, no. 11, pp. 2255–2259, 1989.
- [21] M. Harfouche, “The coherence collapse regime of high-coherence Si/III-V lasers and the use of swept frequency semiconductor lasers for full field 3d imaging,” PhD thesis, California Institute of Technology, 2018.

## **CHAPTER 6**

### **SUMMARY AND FUTURE DIRECTIONS**

In this thesis, I have attempted to provide an insight into the development and vast potential of SiPh and devices derived therefrom in particular hybrid III-V/Si SCLs. The underlying capability, fundamental characteristics and limit to the performance of these optical components for PIC applications is described and proven experimentally. I have also carefully reviewed the motivations and associated challenges for potentially achieving light sources on-chip for isolator-free applications and the use of these devices for secure communications via chaos enhancement through the ROF when using a combination of short and long-cavity feedbacks at different strength levels.

The intimate integration of photonics with electronic functions offers a significant advantage to integrate optical components with electronic functions on-chip in order to deliver increased capacity and effectively move data at unimaginable speed rates. Soon, we will witness an increased migration of SiPh from a lab scale concept to the manufacturing facility to address latency, compute capacity and craved power. This technology has made tremendous progress throughout the years and continues to gain great attention due to the key benefits this technology can offer to a wide range of applications, in particular to the telecommunications industry. The development of compact reliable optical-interconnects-to-the-chip for the next generation of data centers can enable better use of available capacity for information transport on the existing fiber infrastructure while also enabling new powerful techniques for transmission impairment control [1]. Overall, The heterogeneous integration of optical components and electronic functions on-chip provides significant performance improvements and increased functionality in addition to enhanced power efficiency and substantial size reduction [2, 3].

These features are critical for the exponential growth of data centers and essential to

meet the new optical network requirements in order to handle the complexity of data traffic. In addition, it is important to emphasize that the extraordinary development of PIC technologies is one of the most attractive solutions considered to address the bottlenecks associated with the ongoing digital transformation and enable the rapidly increasing bandwidth demand required by data centers to meet the desired hyper-connectivity levels [4, 5].

Although it is well-established that PICs gather all the essential functionalities of photonics systems, it is also known that optical isolation is a serious drawback since it is not possible to position an optical isolator with sufficient isolation ratio and low insertion loss at the output of the laser as it is commonly done in fiber and free space optics [6, 7]. Therefore, designing ultra-stable semiconductor lasers with the intent to tackle unwanted short-cavity reflections remains a vital challenge for future integrated photonic technologies.

The work presented here aims at exploring the nonlinear dynamics of various configurations of hybrid III-V DFB lasers grown on Si substrate under different experimental conditions to fully understand their performance and identify strengths and technology limitations. In summary, three major accomplishments have been successfully demonstrated throughout the course of this study:

1. The existence of internal reflections within hybrid III-V/Si SCLs
2. Manipulation of the chaos bandwidth through the use of short and long delay feedbacks
3. High- $Q$  devices feedback insensitivity for isolator-free solutions

The power evolution coupled with an AR fiber of the hybrid designs in Chapter IV, exhibits a slight competition between two modes which translates into a kink in the curve. Above 4 times threshold, the laser also exhibited power drops which were also observed on the other lasers of the same bar, but differed from device to device. Such behavior

hints that parasitic reflections are present within these devices. This parasitic reflections are most likely associated with the VBG and tapers since they create reflections which only seem to affect the laser far above threshold through variations of the optical power or changes in the ROF. In this case, the VBG were only necessary for testing purposes in order to characterize several unprocessed devices on the same bar but in a PIC they would not be positioned after the laser. They however affected our study in two ways: first via their transmission losses of approximately 7 dB, and secondly by their parasitic reflectivity which affected laser operation when biased high above threshold.

As observed in the results obtained on the hybrid DFB in Section 4.1.3, a chaotic dynamics of 14 GHz was achieved, which lead us to believe this high value of ROF can somehow stem from the aforementioned internal feedback. We then deduce that internal feedback conditions thus allow a small enhancement of the ROF for some bias currents, showing an effect of parasitic feedback very different from the detrimental impact it can have further above threshold. Since sources of feedback are often inevitable in a PIC, they can thus be designed to potentially enhance the laser's operation instead of hindering it.

From an application point of view, the sensitivity to external feedback can be detrimental for the performance of a SCL and is often considered a limiting factor due to strong perturbations affecting the emission characteristics of the device. However, from a fundamental physics point of view, deterministic chaos in a SCL when subject to optical feedback paves the way to a new set of novel applications. Chaos enhancement via the excitation of the ROF and related phenomena in SCLs are also attractive attributes that can be used to investigate their practical application in secure communications as demonstrated herein. Therefore, a large ROF can be instrumental for chaos-based message encryption methods, such as chaos masking or chaos modulation among other applications [8]. Chaotic semiconductor lasers also offer pseudo-random bit generation with extremely high bit-rate, using strongly diverging trajectories, with a starting point almost impossible to recover once the optical signal has been converted to digital signal [9, 10, 11]. This area has already

gained a great amount of interest from different communities and remarkable progress has already been made. As a result, the study and design of novel III-V/Si DFB lasers will continue to remain a fertile arena for future research and development to exploit their tremendous potential in optical communications and address existing challenges associated with PICs.

The results provided in this thesis successfully demonstrate that the dynamics of a hybrid III-V/Si DFB laser under a combination of optical feedback have the potential to achieve passive chaos bandwidth enhancement in PICs. By varying the phase of the short feedback and strength of the long feedback, the dynamics of such devices can be extensively characterized to deeply understand their properties and the consequences of parasitic reflections on the optical and electrical spectrum on the desired applications. In addition, the tuneability of the chaotic dynamics and the bandwidth is of substantial interest for applications requiring random number generation, or broad chaos generation. With feedback cavities integrated into a Si waveguide along with a phase section, higher feedback strengths would be achievable for both short and long feedbacks. Chaotic spectra much wider than those reported in this work could thus be obtained using a single component and passive optical cavities with optional phase sections. This would be of prime importance for the development of low power consumption integrated chaotic transmitters and receivers for secure communications. As the wide bandwidth relies primarily on the larger ROF of the laser, the design of the device is extremely important, and for these applications QW sources may be more appealing than QD as QW lasers generally exhibit much higher ROFs than QDs. In the case of application in a Si PIC, the design of the Si waveguide would be very important also as all possible sources of reflections within the PIC will significantly affect the dynamics of the laser. In Sections 4.1.1 and 4.1.3, it was demonstrated that at least two cavities allow pushing the ROF to higher values: the cavity created by the cleaved fiber, but also the internal parasitic sources of feedback which seem to increase the ROF of the free-running device.

As new expanded services are introduced, such as high definition TV, social networking, on-line video streaming applications, 3D TV and computerized stock trading among others, emerging requirements are also identified to meet the hyper-connectivity demand. The demand of optical bandwidth will continue to maintain the extreme 100x bandwidth increase/decade slope [12]. As a result, novel approaches and innovate laser configurations continue to be proposed. For instance, the experimental results presented on high- $Q$  factor devices demonstrated their potential to serve as an alternative solution for isolator-free applications in future PICs.

Commercial isolators are key in fiber-optic communication systems because of their unique functionality to transmit light from input to output while blocking backward propagating light. These devices are considered bulk components, and as such they constitute the only type of optical component that is not readily available in an integrated form [13]. However, significant research efforts and advances in SCLs are underway to accomplish isolator-free operation that can potentially reduce the network architecture footprint while reducing capital expenditures of the overall data center infrastructure. The innovated and unique modal engineering approach of the high- $Q$  device characterized in Chapter V in which light is generated in the III-V material, and stored in the low loss Si region substantially enhances the  $Q$  factor of the cavity resonator. As a result, the device is able to tolerate significant disturbances caused by unintentional back-reflections generated within various sources, which in turn can be detrimental for light sources on chip as previously demonstrated.

The development of feedback insensitive lasers remain a major challenge for SiPh integration to alleviate the risk of undesired reflections. However, the work herein demonstrates significant progress towards light sources with absolute insensitivity, which has yet to be reported. The achieved performance constitutes a new milestone towards feedback insensitivity of a single mode laser with a DFB configuration and a large  $Q$  factor ideal for error-free transmission. The high level of CC regime permits a 10 Gbps error-free transmission over a 10 km fiber coil. Compared to the aftermentioned solutions discussed throughout

the course of my thesis, the high- $Q$  approach, does not require neither a complex design [14], nor a nano-cavity [15], nor an epitaxial growth of QDs [16], nor the utilization of any artificial solution (e.g., external cavity) [17]. Its enhanced performance is simply due to the large  $Q$  factor of the laser's cavity, which pushes the transition to the CC regime at much higher reflection levels as compared to their conventional III-V counterparts. This brings this technology a step further towards the development of future low cost PIC and isolator-free applications, which can eliminate the need of expensive nonreciprocal devices to protect active elements from back-reflected light that can substantially hinder their operation. A large  $Q$  factor stems from the reduction of the material losses because the hybrid III-V/Si structure allows the storage of the optical energy in the Si region, where losses are less predominant than in the III-V material, which in turn results in a much lower gain required to achieve lasing.

SiPh is actively evolving and will continue to remain a fertile arena of research able to achieve unimaginable application levels by disrupting a range of technologies. The convergence of photonics and electronics on the same platform as well as the considerable progress reported up to date in this field makes SiPh the best suited technology to address existing shortcomings for the next generation of data centers. Future experimental work will concentrate on the study of hybrid III-V/Si lasers in several other realistic feedback schemes, with cavities of a few centimeters (typ. around 5 cm) to investigate more quantitatively the bandwidth of these type of devices operating under a combination of short and long delays of optical feedback. These intermediate cavity lengths would closely match those of the parasitic feedback cavities usually found in PICs, which would allow evaluating the behavior of various designs of III-V/Si light sources under a realistic multiple-cavity configuration. With external cavities of similar lengths, the impact of such multiple cavities may indeed be very different from what is observed in this work, where the smallest one may dominate the overall dynamics of the device. Further studies on some of the proposed laser designs in Chapter IV are also necessary to determine whether or not the taper region

can indeed generate enough reflection to create the sub-cavity in question. The study of the dynamics of DFB lasers under long-cavity feedback will also allow comparison of the behavior of hybrid III-V/Si lasers with well-known QW and QD III-V laser sources with larger damping rate. In addition, a theoretical study of a DFB laser subject to several feedback sources with different external cavity lengths would be necessary to fully understand the effect of such combinations of feedback for Si lasers. Using the LK laser equation in the context of multiple feedback sources with parameters and cavity lengths specific to III-V/Si lasers should yield interesting results. Accounting for the complex interaction between modes in-between the two taper regions of the devices presented in this study may require travelling wave modeling.

Additional efforts will focus on the simulation of single mode III-V and III-V/Si lasers subject to two external cavities in order to replicate these experimental results to obtain a more reliable set of data with a higher confidence level. Conditions to maximize the increase of the ROF under short feedback will thus be studied in the presence of several short cavities, in order to reach larger bandwidth enhancements. It will also be possible to determine which absolute feedback phase leads to the wider chaos bandwidth. Finally, the theoretical results should allow identifying the minimum length of the long cavity required to achieve sufficient chaos bandwidth, which will help the design and realization of an integrated wideband chaos generator. Other efforts should also consider higher modulation rates to evaluate overall performance and the BER under optical feedback of different laser modalities.

The experimental results reported herein, can serve as a source of information to assist researchers in the field with making informed decisions on technology improvements to optimize the development for practical applications such as future high-speed integrated circuits.

## REFERENCES

- [1] L. A. Coldren, S. W. Corzine, and M. L. Mašanović, *Diode lasers and photonic integrated circuits*. John Wiley & Sons, Inc., 2012.
- [2] J. C. Norman, D. Jung, Y. Wan, and J. E. Bowers, “Perspective: The future of quantum dot photonic integrated circuits,” *APL Photonics*, vol. 3, no. 3, p. 030901, 2018.
- [3] L. Vivien, D. Marris-Morini, L. Virot, D. Perez-Galacho, G. Rasigade, J.-M. Hartmann, E. Cassan, P. Crozat, S. Olivier, C. Baudot, F. Boeuf, and J.-M. Fedeli, “High speed silicon-based optoelectronic devices on 300mm platform,” in *2014 16th International Conference on Transparent Optical Networks (ICTON)*, IEEE, 2014.
- [4] G. Roelkens, L. Liu, D. Liang, R. Jones, A. Fang, B. Koch, and J. Bowers, “III-V/silicon photonics for on-chip and intra-chip optical interconnects,” *Laser & Photonics Reviews*, vol. 4, no. 6, pp. 751–779, 2010.
- [5] G.-H. Duan, C. Jany, A. L. Liepvre, A. Accard, M. Lamponi, D. Make, P. Kaspar, G. Levaufre, N. Girard, F. Lelarge, J.-M. Fedeli, A. Descos, B. B. Bakir, S. Mes-saoudene, D. Bordel, S. Menezo, G. de Valicourt, S. Keyvaninia, G. Roelkens, D. V. Thourhout, D. J. Thomson, F. Y. Gardes, and G. T. Reed, “Hybrid III–V on silicon lasers for photonic integrated circuits on silicon,” *IEEE Journal of Selected Topics in Quantum Electronics*, vol. 20, no. 4, pp. 158–170, 2014.
- [6] L. Bi, J. Hu, P. Jiang, D. H. Kim, G. F. Dionne, L. C. Kimerling, and C. A. Ross, “On-chip optical isolation in monolithically integrated non-reciprocal optical resonators,” *Nature Photonics*, vol. 5, no. 12, pp. 758–762, 2011.
- [7] Y. Zhang, Q. Du, C. Wang, T. Fakhrol, S. Liu, L. Deng, D. Huang, P. Pintus, J. Bowers, C. A. Ross, J. Hu, and L. Bi, “Monolithic integration of broadband optical isolators for polarization-diverse silicon photonics,” *Optica*, vol. 6, no. 4, p. 473, 2019.
- [8] G. D. VanWiggeren, “Communication with chaotic lasers,” *Science*, vol. 279, no. 5354, pp. 1198–1200, 1998.
- [9] R. Takahashi, Y. Akizawa, A. Uchida, T. Harayama, K. Tsuzuki, S. Sunada, K. Arai, K. Yoshimura, and P. Davis, “Fast physical random bit generation with photonic integrated circuits with different external cavity lengths for chaos generation,” *Optics Express*, vol. 22, no. 10, p. 11727, 2014.

- [10] A. Uchida, *Optical communication with chaotic lasers: Applications of nonlinear dynamics and synchronization*. Wiley-VCH, 2012, ISBN: 9783527408696.
- [11] M. C. Soriano, J. García-Ojalvo, C. R. Mirasso, and I. Fischer, “Complex photonics: Dynamics and applications of delay-coupled semiconductor lasers,” *Reviews of Modern Physics*, vol. 85, no. 1, pp. 421–470, 2013.
- [12] L. A. Coldren, S. C. Nicholes, L. Johansson, S. Ristic, R. S. Guzzon, E. J. Norberg, and U. Krishnamachari, “High performance InP-based photonic ICs—a tutorial,” *Journal of Lightwave Technology*, vol. 29, no. 4, pp. 554–570, 2011.
- [13] J. Fujita, R. Gerhardt, and L. A. Eldada, “Hybrid-integrated optical isolators and circulators,” in *Optoelectronic Interconnects, Integrated Circuits, and Packaging*, L. A. Eldada, R. A. Heyler, and S. John R. Rowlette, Eds., SPIE, 2002.
- [14] D. Lenstra, T. T. M. van Schaijk, and K. A. Williams, “Toward a feedback-insensitive semiconductor laser,” *IEEE Journal of Selected Topics in Quantum Electronics*, vol. 25, no. 6, pp. 1–13, 2019.
- [15] T. S. Rasmussen, Y. Yu, and J. Mork, “Suppression of coherence collapse in semiconductor fano lasers,” *Physical Review Letters*, vol. 123, no. 23, 2019.
- [16] G. Eisenstein and D. Bimberg, Eds., *Green photonics and electronics*. Springer International Publishing, 2017.
- [17] L. A. Coldren, “Diode lasers and photonic integrated circuits,” *Optical Engineering*, vol. 36, no. 2, p. 616, 1997.

## VITA

Sandra C. Gomez

### EDUCATION

- Doctorate student in Communications and Electronics at Telecom ParisTech, September 15 - March 2020. Thesis title: “Effects of Dynamics and Optical Feedback on Hybrid III-V/Silicon Semiconductor Lasers.”
- Master of Engineering in Electrical Engineering at Stevens Institute of Technology, September 2002 - May 2005. Thesis title: “Trade-offs, Advantages, and Disadvantages of Different Beamforming Algorithms.” Concentration in Digital Signal Processing.
- Bachelor of Engineering in Electrical Engineering at Stevens Institute of Technology, September 1997 - May 2002.

### EMPLOYMENT

- **International Program Manager**, U.S. Army Combat Capabilities Development Command Armaments Center (CCDC-AC), January 2019 - present.
- **Technical Director**, U.S. Army Research Development and Engineering Command, January 2014 - December 2018.
- **Project Manager**, U.S. Special Operations Command, July 2002 - January 2014.
- **Project Engineer**, U.S. Army Research, Development and Engineering Center, July 2002 - January 2014.

## PUBLISHED CONTRIBUTIONS

- **Gomez, S.**, Huang, H., Duan J., Shen, A., Combrie, S., Baili, G., de Rossi, A. and Grillot, F., “High Coherence Collapse of a Hybrid Si/III-V Semiconductor Laser with a Large Quality Factor,” *Journal of Physics: Photonics* (2020).
- **Gomez, S.**, Huang, H., Sawadogo, B., Gallet, A., Shen, A., Combrié, S., Baili, S., de Rossi, A and Grillot, F., “10 Gbps Error-free Transmission of a High Coherent Si/III-V Hybrid Distributed Feedback Laser under Strong Optical Feedback,” *IEEE Photonics Conference* (2019).
- **Gomez, S.**, Huang, H., A. B, Sawadogo and Grillot, F., “10 Gbs Floor Free Transmission of a Hybrid III-V on Silicon Distributed Feedback Laser with Optical Feedback”, *OSA Frontiers in Optics Technical Digest* (2018).
- **Gomez, S.**, Schires, K., Gallet, A., Duan, G.-H and Grillot, F., “Chaotic Bandwidth of III-V/Silicon Distributed Feedback Lasers Subject to Various optical Feedback Conditions,” *IS-PALD, Paris, France* (2017).
- **Gomez, S.**, Schires, K., Gallet, A., Baili, G., Duan, G.-H and Grillot, F., “Wideband Chaos in Hybrid III-V/Silicon Distributed Feedback Semiconductor Lasers under Optical Feedback,” *SPIE Photonics West – Physics and Simulation of Optoelectronic Devices XXV*. 10098, 100980I (2017).
- Schires, K., **Gomez, S.**, Gallet, A., Duan, G.-H and Grillot, F., “Passive Chaos Bandwidth Enhancement under Dual-Optical Feedback with Hybrid III-V/Si DFB Laser,” *IEEE J. of Selected Topics in Quant. Electron.* 23, 1801309 (2017).
- Schires, K., Girard, N., Baili, G., Duan, G.-H., **Gomez, S** and Grillot, F., “Dynamics of Hybrid III-V Silicon Semiconductor Lasers for Integrated Photonics,” *IEEE J. of Selected Topics in Quant. Electron.* 22, 1800107 (2016)

- Schires, K., Girard, N., Baili, G., Duan, G.-H., **Gomez, S.**, and Grillot, F., “Nonlinear Dynamics of Hybrid III-V/Si Laser Poster,” NanoDesign project (2016).

## **GLOSSARY**

AR - Anti-Reflection

ASE - Amplified Spontaneous Emission

BKR - Back Reflector

B2B - Back-to-Back

BER - Bit Error Rate

BOX - Buried Oxide

CWDM - Coarse Wavelength Division Multiplexing

DCI - Data Center Interconnects

DC - Data Center

DBR - Distributed Bragg Reflector

DUT - Device Under Test

DSL - Digital Subscriber Line

DFB - Distributed Feedback

DML - Directly modulated lasers

DM - Direct Modulation

DH - Double Heterostructure

DWDM - Dense Wavelength Division Multiplexing

CH - Carrier Heating

CC - Coherence Collapse

CR - Clock Recovery

CW - Continuous Wave

CMOS - Complementary Metal Oxide Semiconductor

CMP - Chemical Mechanical Polishing

CPU - Central Processing Unit

CAGR - Compound Annual Growth Rate

DOS - Density of States

DBR - Distributed Bragg Reflector

DSL - Digital Subscriber Line

ESQ - Electrical Spectrum Analyzer

EDFA - Erbium-Doped Fiber Amplifier

EB - Exabytes

EHP - Electron-Hole Pairs

ECM - External Cavity Modes

EAM - Electro-Absorption Modulator

FP - Fabry-Perot

FGC - Focusing Grating Coupler

FSO - Free Space Optics

FSR - Free Spectral Range

GaAs - Gallium Arsenide

GaAs - Gallium Arsenide Phosphide

HH - Heavy Hole

HPC - High Performance Computing

HDTV - High-Definition Television

HBr - Hydrogen Bromide

IoE - Internet of Everything

IP - Internet Protocol

InP - Indium Phosphide

LD - Laser Diode

LCC - Light Current Characteristics

LEF - Linewidth Enhancement Factor

LFF - Low Frequency Fluctuations

LSHB - Longitudinal Spatial Hole Burning

MBE - Molecular Beam Epitaxy

MM - Multi Mode

MZM - Mach-Zehnder Modulator

MOVPE - Metal Organic Vapor Phase Epitaxy

OSA - Optical Spectrum Analyzer

OSC - Oscilloscope

PM - Power Meter

PIC - Photonics Integrated Circuits

PRBS - Pseudo-Random Bit Sequence

QW - Quantum Well

QD - Quantum Dot

ROF - Relaxation Oscillation Frequency

RF - Radio Frequency

RR - Ring Resonator

SCL - Semiconductor Conductor Laser

SEM - Scanned Electron Image

Si - Silicon

SiPh - Silicon Photonics

SOA - Semiconductor Optical Amplifier

SOI - Silicon-on-Insulator

SS - Single Mode

SMSR - Single Mode Suppression Ratio

SHB - Spatial Hole Burning

SWT - Switch

SGDBR - Sampled Grating Distributed Bragg Reflector

SSGDBR - Super Structure Grating Distributed Bragg Reflector

TE - Transverse Electric

TM - Transverse Magnetic

TD - Threading Dislocations

TBPF - Thin Band-Pass Filter

TUL - Tunable Laser TUL

UCSB - University of California Santa Barbara

VCSEL - Vertical Cavity Surface Emitting Laser

VBG - Vertical Bragg Gratings

VOD - Video-On-Demand

VNI - Visual Networking Index

WDM - Wavelength division multiplexing

ZB - Zettabyte